Università Politecnica delle Marche
Corso di Dottorato in Ingegneria Civile, Ambientale, Edile ed Architettura

Experimental Evaluation of Infill Masonry Walls Stiffness for the Modelling of Non-Structural Components in R.C. Frame Buildings

Ph.D. Dissertation of:
Vanni Nicoletti

Advisor:
Prof. Ing. Luigino Dezi
Co-Advisor:
Prof. Ing. Fabrizio Gara
Curriculum Supervisor:
Prof. Ing. Stefano Lenci

XXX ciclo

Università Politecnica delle Marche
Facoltà di Ingegneria
Dipartimento di Ingegneria Civile, Edile ed Architettura

Via Brecce Bianche – 60131 – Ancona, Italia

Contents

List of Figures

List of Tables

Abstract

Infill walls are commonly disregarded in the modelling of reinforced concrete (r.c.) frame structures and only their contribution in terms of mass is taken into account assuming that resistance and stiffness do not affect the structural response. This practice is supported by the fact that (*i*) at ultimate limit state infill walls are usually considered to be completely damaged, so that their contribution is negligible in terms of stiffness, while (*ii*) at the damage limitation limit state the value of the interstorey drift, obtained by neglecting the infill walls stiffness contribution, is commonly considered to be conservative. However, for strategic buildings, such as schools, hospitals, police and fire stations, it is crucial to preserve the infill walls from any damage, even for severe earthquake, in order to guarantee the building occupancy during the emergency management. Furthermore, these buildings are sometimes seismically protected with system and devices (dampers, isolators, etc…) whose design requires the real dynamic behaviour of the structure (in terms of frequencies and/or displacements and/or velocities) to be considered. To this purpose, it becomes crucial to accurately model the entire structure, including infill walls, and to validate this model on the basis of experimental evidences. The wall typology and the construction procedures are source of uncertainties in modelling interactions between structural and non-structural components. Thus, an experimental evaluation of the stiffness properties of the wall infill panel could be very useful to assess the stiffening contribution added by the infill masonry walls to the concrete frame in the structural model adopted for the design.

In this thesis is presented a procedure for developing accurate global finite element (f.e.) models of infilled r.c. frame buildings based on results of experimental an operational modal analysis of non-structural components and of the whole buildings. In particular, impact load tests with an instrumented hammer are performed on homogeneous wall panels to identify the modal parameters (frequency and mode shapes) and to estimate the mechanical properties of the masonry walls. Afterwards, the infill walls are included in the f.e. structural model, whose modal parameters are compared with those derived with operational modal analysis based on ambient vibration measurements. Furthermore, an experimental campaign on three specimens of infill masonry walls built in the Laboratory of Materials and Structures of the Faculty of Engineering at the Università Politecnica delle Marche is conducted. These specimens are built with the target to reproduce the features of some of the in situ investigated infill walls and are tested both dynamically and statically. First of all, impact load tests with an instrumented hammer are performed to investigate the out of plane dynamic behaviour of these walls; then, lateral load tests are carried out to investigate the in plane static behaviour of the panel under low level of lateral forces. The experimental results obtained are used to calibrate f.e. models of the specimens with the aim to evaluate the reliability of the masonry mechanical properties estimated through different approaches.

Keywords: infilled r.c. frame buildings, infill wall modelling, building dynamic identification, impact load test, Operational and Experimental Modal Analysis.

Sommario

Solitamente le tamponature vengono trascurate nella modellazione delle strutture a telaio in cemento armato e solamente il loro contributo in termini di massa viene preso in considerazione, assumendo che la resistenza e la rigidezza delle stesse non influiscano sulla risposta strutturale. Questa pratica è supportata dal fatto che (*i*) generalmente allo stato limite ultimo le tamponature si considerano completamente danneggiate e, quindi, il loro contributo in termini di rigidezza è trascurabile, mentre (*ii*) allo stato limite di danno il valore dello spostamento di interpiano, ottenuto trascurando il contributo di rigidezza delle tamponature, può essere considerato a favore di sicurezza. Tuttavia, per edifici di importanza strategica, quali scuole, ospedali, caserme delle forze dell'ordine e dei Vigili del Fuoco, è cruciale preservare le tamponature da qualsiasi danno, anche per terremoti di entità severa, in modo da garantire il normale utilizzo dell'edificio durante la gestione dell'emergenza. Inoltre, questi edifici a volte sono sismicamente protetti con sistemi e dispositivi (smorzatori, isolatori, ecc…) il cui progetto richiede che sia tenuto in considerazione il reale comportamento dinamico della struttura (in termini di frequenze e/o spostamenti e/o velocità). Per questo diventa cruciale modellare accuratamente l'intera struttura, includendo le tamponature, e validare questo modello così ottenuto sulla base dell'evidenza sperimentale. La tipologia delle pareti e le loro procedure costruttive sono fonte di incertezze nella modellazione delle interazioni tra la struttura e gli elementi non strutturali. Quindi, una valutazione sperimentale delle proprietà di rigidezza dei pannelli di tamponatura potrebbe essere molto utile per valutare, all'interno del modello strutturale adottato per il progetto, il contributo in termini di rigidezza fornito alla struttura in c.a. da questi elementi non strutturali.

In questa tesi viene presentata una procedura per realizzare modelli globali agli elementi finiti accurati di edifici a telaio in c.a. tamponati, basandosi su risultati ottenuti da analisi modali sperimentali e operative sviluppate rispettivamente su elementi non strutturali e sull'intero edificio. In particolare, sono stati eseguiti test di impatto con martello strumentato su pareti omogenee per identificarne i parametri modali (frequenze e forme modali) e per stimarne le proprietà meccaniche. Dopo di che, le tamponature sono state inserite nel modello strutturale globale agli elementi finiti, i cui parametri modali vengono confrontati con quelli derivanti da analisi modali operative basate su misurazioni di vibrazioni ambientali per valutarne l'accuratezza. In seguito, è stata condotta una campagna sperimentale su tre provini di tamponatura costruiti all'interno del Laboratorio di Prove di Materiali e Strutture della Facoltà di Ingegneria dell'Università Politecnica delle Marche. Questi provini sono stati realizzati con l'intento di riprodurre le caratteristiche di alcune delle tamponature testate in sito e su di essi vengono svolte prove sia dinamiche che statiche. Innanzi tutto, sono stati effettuati test ad impatto con martello strumentato per investigarne il comportamento dinamico fuori dal piano; successivamente sono state svolte prove di spinta laterale per investigare il comportamento statico nel piano dei pannelli soggetti a bassi livelli di forze orizzontali. I risultati sperimentali ottenuti sono stati utilizzati per calibrare modelli agli elementi finiti dei provini al fine di valutare l'esattezza delle proprietà meccaniche delle tamponature stimate in precedenza e secondo diversi approcci.

Parole chiave: edifici a telaio in c.a. tamponati, modellazione delle tamponature, identificazione dinamica degli edifici, prove ad impatto, analisi modale sperimentale e operativa.

Introduction

I.1. Infill masonry walls in the modelling of the edifices

Over the time the infill masonry walls were considered as non-structural elements and their influence in the structural response was not taken into account, being only considered for the gravity loads. This practice is supported by the fact that (*i*) at ultimate limit state infill walls are usually considered to be completely damaged, so that their contribution is negligible in terms of stiffness, while (*ii*) at the damage limitation limit state the value of the interstorey drift, obtained by neglecting the infill walls stiffness contribution, is commonly considered to be conservative. Nowadays it is accepted by the overall community that the stiffness and strength provided by these elements must be considered in the numerical models and in the analytical calculations in the assessment of a reinforced concrete (r.c.) structure, especially for those founded in earthquake-prone areas around the world. Furthermore, for strategic buildings, such as schools, hospitals, police and fire stations, it is crucial to preserve the infill walls from any damage, even for severe earthquake, in order to guarantee the building occupancy during the emergency management. Besides, these buildings are sometimes seismically protected with system and devices (dampers, isolators, etc…) whose design requires the real dynamic behaviour of the structure (in terms of frequencies and/or displacements and/or velocities) to be considered. To this purpose, it becomes crucial to accurately model the entire structure, including infill walls.

However, parameter and modelling uncertainties (e.g., material and geometric parameters, energy dissipation mechanisms, etc.) exist and affect the accuracy of such finite element (f.e.) models in predicting structural response to dynamic loads. Estimation of the dynamic properties of structures using vibration data recorded in the field or from laboratory specimens allows the calibration of these numerical models. Experimental and operational modal analysis are the main procedures to identify the modal parameters (natural frequencies, equivalent damping ratios and mode shapes) from recorded vibration data, information that can be used to improve and update numerical models of the structures of interest. Most of the studies conducted in this area were based on data collected from completed structures, while only a few have analysed the variation of the dynamic properties of the buildings during construction and the effects of non-structural components and systems on the dynamic properties. Most of them studied the variation of the modal properties during construction and due to non-structural elements using ambient vibrations recorded in three-storeys to fifty-six-storeys buildings to identify the modal parameters of the buildings and compare them with those obtained from f.e. models typically used in engineering practice.

By following the construction process of a building it is possible to progressively validate numerical models of the structure and also to control the quality and safety of the construction. Comparison between dynamic properties identified from experimental data with those predicted from numerical models help engineers to take predictive decisions in case of unexpected or anomalous behaviour. Furthermore, it has been shown that the effects of the non-structural elements should not be neglected because their dynamic interaction with the structure can influence significantly the dynamic properties of the compete (coupled structural and non-structural) building system. The presence of the infill walls increase the lateral stiffness of the structures (and consequently their natural frequencies) and this can influence significantly the building performance when subjected to earthquakes. The contribution of the infills to the building behaviour depends on several aspects, such as the infills mechanical properties, the plan and height distribution of the infill panels, the relative stiffness and strength between the frame and masonry walls, type of connection between the infill masonry walls and the frame. It is evident that further and in-depth knowledge concerning the infill panels behaviour is needed in order to support the development and calibration of precise numerical models.

Typically an infill wall can be modelled as a diagonal strut connected to the two diagonal corners of the r.c. frame. Many authors investigated the geometrical and mechanical properties of these diagonal elements and proposed several modelling strategies to be used in global finite models of the buildings. In particular, as concern the material properties, the most important parameter that characterize the behaviour of an infill panel is the elastic modulus E. Given the variations in type and quality of materials and constructions, no unique modulus of elasticity can be defined for all infill walls; indeed, this parameter actually depends on the materials from which the infill is made and is rather difficult to determine. In each region of the world, the dimension and material type of the brick unit and mortar characteristics are different as well as construction practice. Moreover, the mentioned items have local quality and technical specification. Therefore it is not surprising to find various values for the mechanical properties of infills in different references. Eurocode 6, Calvi et al. and Crisafulli suggest that the elastic modulus can be set equal to $1000f_{cw}$, that is 1000 times its compressive strength of masonry. Morandi et al. performed static tests on three real dimension infill masonry walls built with different types of hollow clay bricks and thicknesses. They obtained that for the wall with thickness of 8 cm the elastic modulus E_h relevant to the horizontal direction is equal to 991 MPa while the elastic modulus E_v for the vertical direction is equal 1873 MPa; for the wall 30 cm thick E_h is equal to 1050 MPa while E_v 3240 MPa. Finally the wall composed by two side by side layers of 12 cm thick bricks gives E_h equal to 991 MPa and E_v equal to 1873 MPa. Koken determined experimentally that for a wall with hollow clay bricks of 13.5 x 19 x 19 cm dimensions, cement mortar and 3 cm thick cement plaster layer on the both sides, the modulus of elasticity is equal to 1393 MPa. Starvidis et al. determined modulus of elasticity for masonry prisms around 6000 MPa from a previous experimental work. FEMA450 implies that the modulus of elasticity of a masonry wall can be assumed 550 times greater compared to its compressive strength. Moreover, Ozkaynak et al., by implementing compression tests of the masonry wallets with dimensions of 35 x 35 x 5.6 cm obtained the elastic moduli of the masonry to be about 2500 MPa. In their numerical analysis, Hatzigeorgiu and Kanapitsas assumed the modulus of elasticity of masonry was equal to 1500 MPa.

I.2. Thesis objectives

The focus of this thesis is the investigation of the effects of infill masonry walls on the global dynamic behaviour of buildings and the calibration of global f.e. models of the edifices whose take into account both the mass and stiffness contributions of these non-structural elements. The study is developed by reference to two buildings case studies with r.c. frame structures and infill masonry walls: the first is a four-storeys building with considerable plan dimensions located in Fermo in the centre of Italy (called Building 1) and the second one is a two-storeys semi-detached house located in Ancona in the centre of Italy (called Building 2). To determine the effects of the infills on the dynamic behaviour of the buildings, experimental dynamic tests are performed on the in situ real structures and the variation of the modal parameters is studied. As concerns the calibration of global f.e. models of buildings is extremely important to have as much knowledge as possible about the geometry of the structural elements, the material mechanical properties, the masses actually present on the building, the constraint conditions, etc. Besides, for the calibration of existing buildings f.e. models, it is crucial to consider the presence of the infill masonry walls, both in terms of mass and stiffness. The determination of the masses of these non-structural elements does not involve particular difficulties if the geometry and construction materials are known, while the same cannot be said with regard to the stiffness. Another purpose of this thesis is to validate an innovative methodology to estimate the mechanical properties of the infills. These material properties are used in the modelling of these non-structural elements within global f.e. models of buildings. The new proposed procedure consists in determining the infill mechanical properties through the results of dynamic impact load tests performed on real walls. These tests are fast and non-invasive and can be carried out in all types of non-structural elements, both during the construction and all along the life of a building. The proposal method can be summarized in the following steps:

1- subdivision of the masonry panel with a regular grid of twenty-five points, in whose the impulsive forces are applied and the accelerometers are placed. Each point of the grid is identified with an alphanumeric code, in detail a letter, starting from left to right, is associated to the vertical lines, while a number, starting from top to bottom, characterizes the horizontal lines;
2- placement of two accelerometers on two grid points to identify as many vibrational modes as possible. The accelerometers are fixed on the infill panel by means of hot glue and with the measurement direction horizontal;
3- application of the impulsive forces at each grid point using an instrumented hammer, while the accelerometers remain always in the same positions. Three or more impulsive forces are applied in each impact point to get a reliable data set;
4- analysis of the collected data. Before the use, recorded data need to be checked and processed and, in particular, the strokes that indicate an anomalous signal both in terms of impulse and acceleration measurements are discarded. Besides, for all the impact points, the number of strokes of the hammer has to be the same (usually three or four strokes), so that the excessive ones are removed from the data set. Finally, the reduction of the data number is achieved through resampling with lower frequency values;

5- identification of the experimental modal parameters of the infill (i.e. natural frequencies and mode shapes) through experimental modal analysis based on data recorded during the impact tests;
6- creation of the f.e. model of the infill and determination of its numerical modal parameters by means of modal analysis;
7- estimation of the mechanical material properties through the comparison between experimental and numerical modal parameters.

I.3. Thesis organization

Chapter 1 deals with the evaluation of the infill masonry walls effects on the dynamic behaviour of the two real buildings case studies. The reported considerations are based on the results of experimental dynamic tests (ambient vibration measurements) performed on the buildings. In the first part of the chapter a description of both buildings investigated is presented, with particular regard to the characterization of the infill masonry walls built. The second part, after a brief introduction on the basic principles of the experimental tests and technique adopted, presents an accurate description of the dynamic in situ tests performed and a critique discussion of the experimental results obtained.

In Chapter 2 the dynamic tests performed on some infill masonry walls of the two buildings case studies are described and analysed in order to identify the dynamic behaviour of these non-structural elements, in terms of modal parameters. After a brief description of the tested walls, i.e. the geometry, the position within the buildings and the construction materials adopted, the impact tests performed are depict and the experimental results obtained are discussed.

Chapter 3 presents the upgrading procedure used to obtain calibrated global f.e. models of the buildings case studies. First, the preliminary f.e. models are developed without considering the infill masonry walls. Then the concrete mechanical properties are adjourned on the basis of the results of ultrasonic in situ tests. Whereupon, the infills are modelled within the global f.e. models of the edifices and the numerical analyses adopted to estimate the mechanical properties of these non-structural elements are illustrated. At the end, the reliability of the global f.e. models developed is evaluated by means of the comparison between the numerical results obtained from the numerical f.e. models and the experimental ones achieved by the in situ tests on the edifices.

The aim of the Chapter 4 is the validation of the infill masonry wall mechanical properties determined on the basis of the results of in situ dynamic tests. This can be possible through the comparison with those obtained from laboratory tests. The first part of the chapter describes the experimental static and dynamic tests performed on clay unit specimens; the second one consists of the estimation of the specimen masonry mechanical properties through numerical analyses. Three specimens are built with different types of clay masonry units with the target to reproduce the same features of some of the in situ tested infills. Each specimen is tested dynamically by means of impact tests with instrumented hammer and statically through in plane lateral load tests with step-wise increased amplitude force up to the collapse of the specimens. Then, the mechanical properties of the specimens are valued by means of numerical analyses. In particular, the dynamic mechanical materials properties are estimated by the comparison between experimental modal parameters obtained from the results of the dynamic tests and the numerical one resulting from f.e. models of the specimens; the static material properties are estimated on the basis of the interpretation of the lateral tests.

Chapter 1.

Experimental evaluation of non-structural components effects on the buildings dynamic behaviour

1.1. Description of the buildings case studies

1.1.1. Building 1: fire station in Fermo

The Building 1 is a fire station newly built in the suburbs of the city of Fermo (centre of Italy). The structure has a rectangular shape with dimensions of 58.50 x 14.80 m and a total height of 15.65 m (three storeys plus the underground floor). The underground floor is 3.50 m high, the ground floor is the highest (5.225 m) because of the presence of the garage for the trucks of firefighters, the first floor is 3.48 m high and here there are the offices, while the second floor is 3.44 m high; part of this last floor is covered with sandwich-roofing panels supported by a steel frame structure forming two flaps with an inclination of 18 degree to the horizontal. In the centre of the last elevation there is a flat roof-walkway in longitudinal direction that connects the two transverse side pavilions. The vertical connection is made by means of two r.c. stairs and two elevators placed at the centre of each stair. The elevators have load-bearing steel structures that are disconnected from the r.c. frame of the building. The structure is composed by thirteen transverse r.c. frames and four longitudinal r.c. frames. The external transverse frames columns have 0.30 x 0.80 m dimensions for the first, second and third elevation, while 0.30 x 0.60 m for the last elevation. All beams are flat beams wide between 0.65 m and 0.80 m, except for the external transverse frames beam at all levels, that are formed beams high between 0.50 m and 0.70 m, and the perimeter beams of the first floor, that have 0.40 x 0.60 m of dimensions. At the last floor all the aisle beams are flat beams with 0.40 x 0.24 m of dimensions. The ground floor and the first floor are made by predalles precast slabs 0.32 m thick, while the attic and the roof floor are r.c. slabs with hollow clay blocks 0.28 m and 0.24 m thick, respectively. The foundation system consists of drilled piles

20 m deep with diameter of 0.60 m and, with pile caps connected by 0.70 x 0.60 m tie beams in transverse and longitudinal directions. The underground floor is bordered all around the building by retaining walls 0.30 m thick that are separated to the structure of the main building by a 0.90 m wide perimeter corridor. The gap between the retaining structures and the building at the ground level is covered by means of cantilever r.c. slabs and metal grids. The cars access at the underground level is allowed by means of a r.c. garage ramp with lateral r.c. retaining walls. Figure 1.1 shows the architectural plans of all the building floors, while Figure 1.2 depicts the East façade and two building sections in East-West direction.

The internal and external infill masonry walls are made with hollow clay bricks with different dimensions and, sometimes, composed with overlapping bricks layers. Only four types of blocks are used to build all the infills (Figure 1.3).

The external infill masonry walls are mainly constituted by hollow clay bricks with different dimensions and they can be divided into three different typologies (EWF-0, EWF-1, EWF-2). The EWF-0 typology (Figure 1.4a) is a double-leaf panel wall with total thickness of 36 cm. The external wall is 12 cm thick and it is made with hollow clay bricks with dimensions of 12 x 50 x 25 cm; the internal ones is 8 cm thick and it is made with hollow clay bricks with dimensions of 8 x 50 x 25 cm. Between the two brick layers there are a thermal insulation layer with thickness of 6 cm and an empty space of about 6 cm. The outdoor and indoor sides of the wall are covered with a plaster layer with thickness of about 2 cm. This typology is used to build all the external infill masonry walls at the underground level. The EWF-1 typology (Figure 1.4b) is a double-leaf panel wall with total thickness of 44 cm. The external wall is 12 cm thick and it is made with facing bricks with dimensions of 12 x 25 x 5.5 cm; the internal ones is 12 cm thick and it is made with hollow clay bricks with dimensions of 12 x 50 x 25 cm. Between the two brick layers there are a reinforced plaster layer 1 cm thick, a thermal insulation layer with thickness of 6 cm and an empty space of about 5 cm. Adjacent to the interior bricks layer there is an aluminium frame that supports the 2 cm thick plasterboard slabs. This typology is used to build the external infill masonry walls of the two pavilions located at the ends of the building from the ground level up to the last elevation. The EWF-2 typology (Figure 1.4c) is one-leaf panel wall with total thickness of 32 cm. The hollow clay bricks, with dimensions of 20 x 25 x 19 cm, are placed with the 25 cm side parallel to the wall plane and the 20 cm side oriented in the thickness direction. On the outdoor side of the wall there is an insulation layer 8 cm thick. The two sides of the wall are covered with a plaster layer with thickness of about 2 cm. This last typology is used for the external infill masonry walls of the East and West sides of the building for the ground and first floor. Considering the last elevation, this typology is used to fill the gap between the sandwich-roofing panels and the flat roof slab in the longitudinal sides of the central aisle, for a height of 1.50 m. It is worth noting that the external infill masonry walls placed on the East and West side of the building have a longer length and a large number of openings respect to those placed on the North and South side that have a lower length and few openings. In Table 1.1 are reported the specific weights for all the external infill masonry wall typologies.

The internal infill masonry walls are made with hollow clay bricks with different dimensions and they can be divided into three different typologies (IWF-0, IWF-1, IWF-2). The IWF-0 typology (Figure 1.5a) is one-leaf panel wall with total thickness of 12 cm. The hollow clay bricks, with dimensions of 8 x 50 x 25 cm, are placed with the 50 cm side parallel to the wall plane and the 8 cm side oriented in the thickness direction.

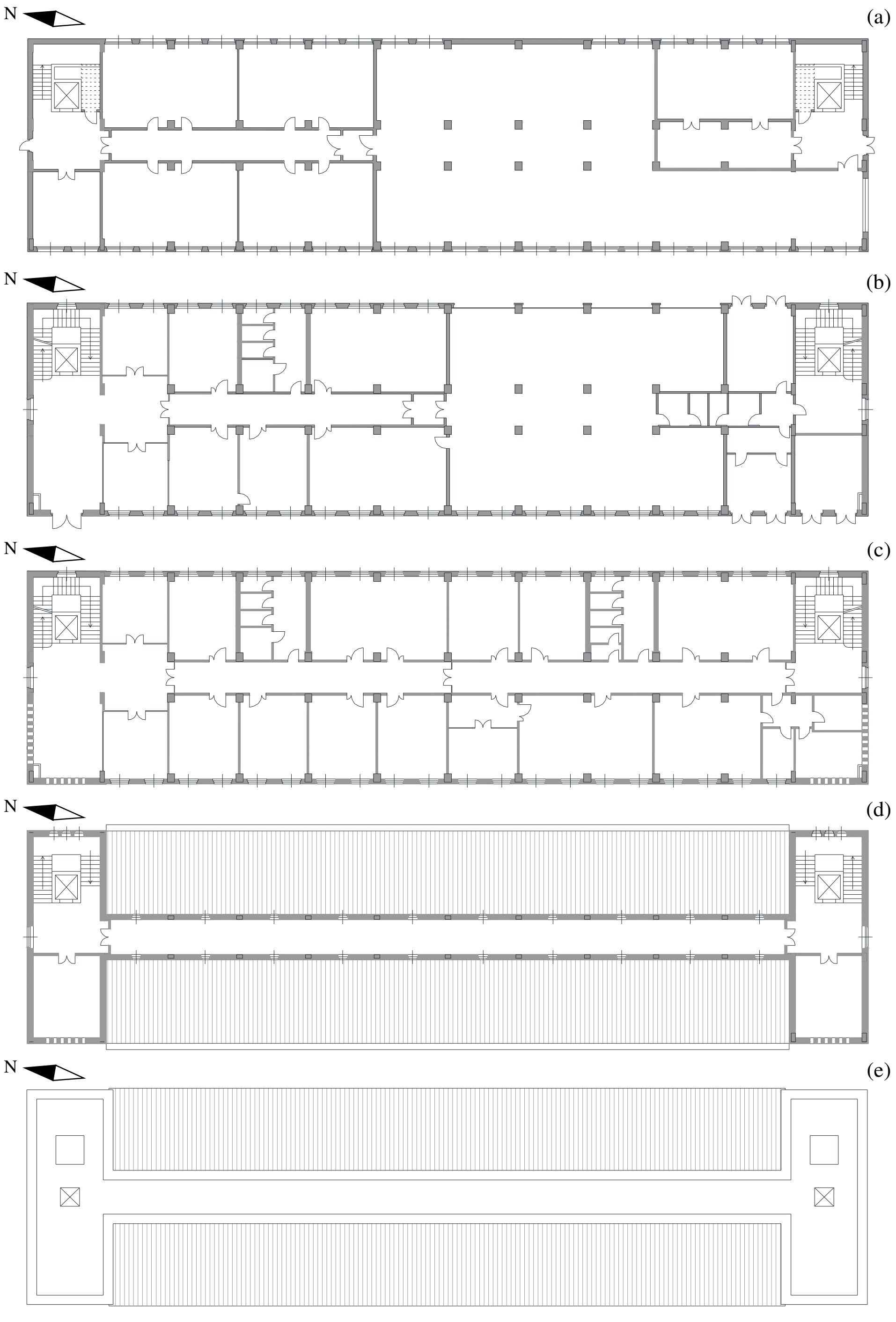

Figure 1.1 Architectural plans: (a) underground floor, (b) ground floor, (c) first floor, (d) attic floor, (e) roof.

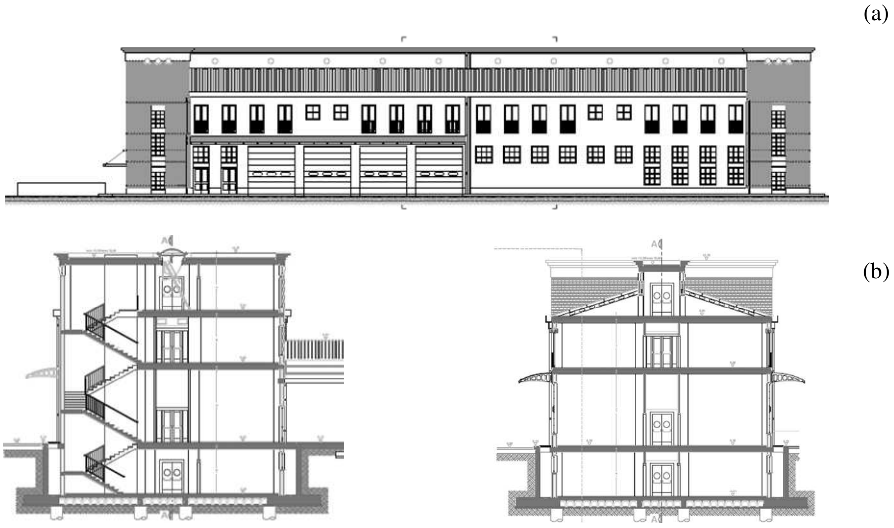

Figure 1.2 Building 1: (a) East façade, (b) sections in East-West direction.

The two sides of the wall are covered with a plaster layer with thickness of about 2 cm. This typology is used for most of the internal infill masonry walls at the first floor. The IWF-1 typology (Figure 1.5b) is one-leaf panel wall with total thickness of 16 cm. The hollow clay bricks, with dimensions of 12 x 50 x 25 cm, are placed with the 50 cm side parallel to the wall plane and the 12 cm side oriented in the thickness direction. The two sides of the wall are covered with a plaster layer with thickness of about 2 cm. This typology is used for most of the internal infill masonry walls at the underground and ground floor and for the internal panels of the staircases for all the elevations. The IWF-2 typology (Figure 1.5c) is one-leaf panel wall with total thickness of 24 cm. The hollow clay bricks, with dimensions of 20 x 25 x 19 cm, are placed with the 25 cm side parallel to the wall plane and the 20 cm side oriented in the thickness direction. The two sides of the wall are covered with a plaster layer with thickness of about 2 cm. This last typology is used for the infill masonry walls that separate the garages from the offices both at the underground and ground floor and also for some of the external infill masonry walls of the pavilions at the last floor. The underground and the ground floor have similar interior partition wall distributions and they have a wide-open space located approximately in the middle of the building used as garages for the trucks and cars; the first floor has an high number of internal infill masonry walls due to the presence of lot of offices; the last floor have only two internal infill masonry walls because the layout of the building changes, assuming an "H" shape where almost all the partition walls are external. Accordingly, the vertical distribution of the internal infill masonry walls can be considerate irregular, though the differences are not so high among the first three elevations. In Table 1.2 are listed the specific weights for all the internal infill masonry wall typologies during the construction processes, namely before and after the plaster realization.

Table 1.1 Specific weight of the external infill masonry walls.

Wall typology	Specific weight [kN/m^3]
EWF-0	6.32
EWF-1	6.80
EWF-2	9.63

Table 1.2 Specific weight of the internal infill masonry walls.

Wall typology	Specific weight [kN/m^3]	
	Without plaster	With plaster
IWF-0	6.52	10.11
IWF-1	8.70	10.85
IWF-2	7.98	9.53

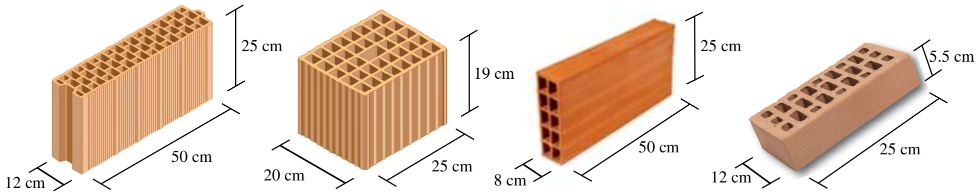

Figure 1.3 Bricks used for the infill masonry walls in Building 1.

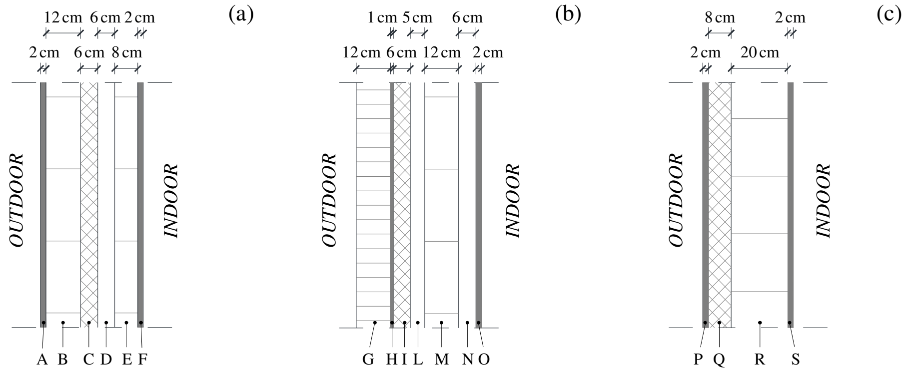

OUTDOOR	
A	Plaster
B	Hollow clay bricks
C	Insulation layer
D	Air layer
E	Hollow clay bricks
F	Plaster
INDOOR	

OUTDOOR	
G	Facing bricks
H	Reinforced plaster
I	Insulation layer
L	Air layer
M	Hollow clay bricks
N	Plasterboard frame
O	Plasterboard
INDOOR	

OUTDOOR	
P	Plaster
Q	Insulation layer
R	Hollow clay bricks
S	Plaster
INDOOR	

Figure 1.4 External infill masonry walls typologies: (a) EWF-0, (b) EWF-1, (c) EWF-2.

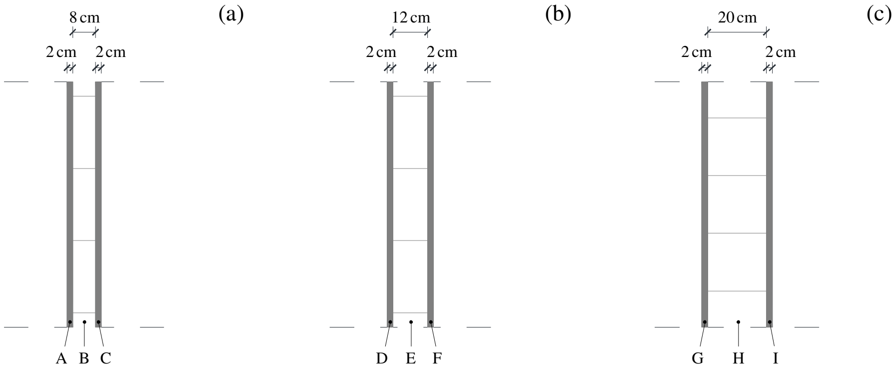

A	Plaster
B	Hollow clay bricks
C	Plaster

G	Plaster
H	Hollow clay bricks
I	Plaster

G	Plaster
H	Hollow clay bricks
I	Plaster

Figure 1.5 Internal infill masonry wall typologies: (a) IWF-0, (b) IWF-1, (c) IWF-2.

1.1.2. Building 2: semi-detached house in Ancona

The Building 2 is a semi-detached house newly built in the suburbs of the city of Ancona (centre of Italy). The structure has a rectangular shape with dimensions of 16.50 x 11.70 m and a total height of 8.00 m (one storey plus the underground floor and the attic floor). The underground floor with garages and cellars is 2.87 m high, the ground floor is 3.20 m high and the attic floor has a height ranging from 0.00 m to 1.93 m inasmuch the roof is sloping. The ground floor has residential use and it consists of two detached housing units with almost square shapes whose are adjacent but misaligned in North-South direction. The access to the underground level is achieved by two external r.c stairs attached to the East and West side of the building and, in future, by two r.c. garage ramps with lateral r.c. retaining walls separated to the main building. The structure is composed by r.c. frames arranged in both the main orthogonal directions of the building; the columns have 0.30 x 0.50 m dimensions for all elevations, while the beams are flat beams wide between 0.42 m and 0.60 m, except for the perimeter beams of the attic storey, that are formed beams high between 0.50 m and 0.66 m. At the attic level there is a shear wall with variable height placed in North-South direction of the building, dividing the two housing units. The underground floor is surrounded by means of r.c. retaining walls with thickness of 0.30 m with openings in correspondence of doors and skylight. The external perimetrical sidewalks and the canopies are realized using r.c. slabs. The ground floor, the first floor and the roof floor are r.c. slabs with hollow clay blocks 0.24 m thick. The foundation system consists of 10 m deep drilled piles with diameter of 0.50 m with pile caps connected by 0.30 x 0.60 m tie beams placed in transverse and longitudinal directions. Figure 1.6 shows the architectural plans of all the floors of the building, while Figure 1.7 shows the South façade and two building sections, one in East-West direction and the other one in North-South direction.

The internal and external infill walls are made with hollow clay bricks with different dimensions. Only three types of blocks are used to build all the infills (Figure 1.8). It is worth noting that all the infill masonry walls at the ground floor are built over a thermal-acoustic insulation layer 12 cm thick that covers entirely the floor slab. There is only one typology of external infill masonry walls named EWA-0 (Figure 1.9a), that is one-leaf panel wall with total thickness of 44 cm. The hollow clay bricks, with dimensions of 30 x 25 x 19 cm, are placed with the 25 cm side parallel to the wall plane and the 30 cm side oriented in the thickness direction. On the outdoor side of the wall there is an insulation layer 10 cm thick. The outdoor and indoor sides of the wall are covered with a plaster layer with thickness of about 2 cm.

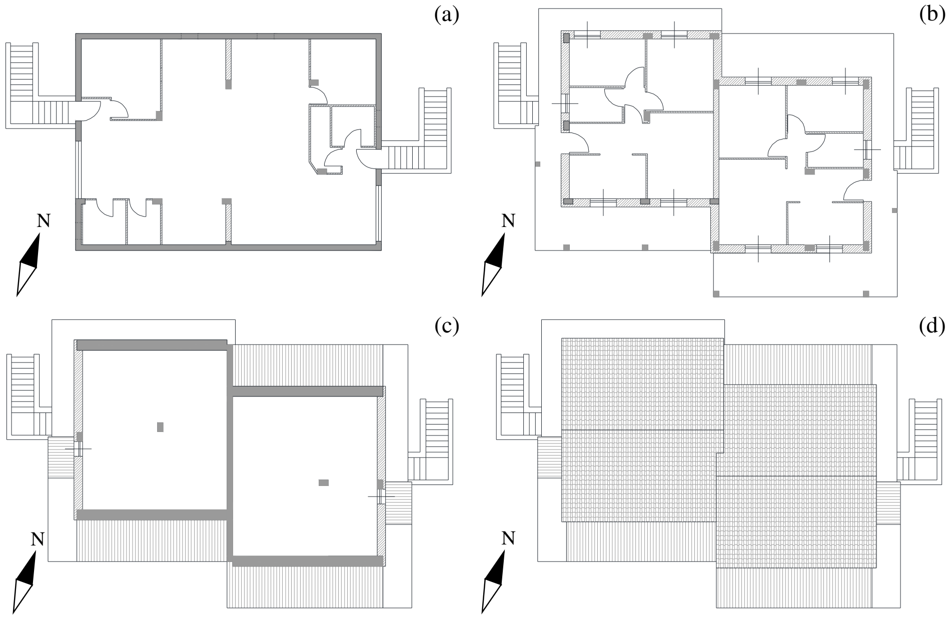

Figure 1.6 Architectural plans: (a) underground floor, (b) ground floor, (c) attic floor, (d) roof.

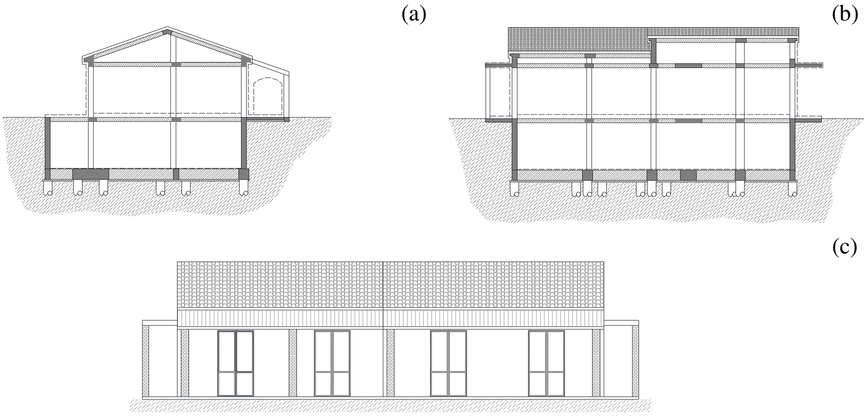

Figure 1.7 Building 2: (a) section in North-South direction, (b) section in East-West direction, (c) façade.

This wall typology is used for all the external infill masonry walls, which are built only at the ground and at the attic level. Referring to the internal infill masonry walls, two typologies are realized. The IWA-0 typology (Figure 1.9b) is a double-leaf panel wall with total thickness of 30 cm. Two identical hollow clay bricks layer are made using bricks with dimensions of 12 x 50 x 19 cm placed with the 50 cm side parallel to the wall plane and the 12 cm side oriented in the thickness direction. Between these two brick layers there is a glass wool insulation layer with 6 cm of thickness. The two sides of the wall are covered with a plaster layer with thickness of about 2 cm. This typology is used for the internal infill masonry walls that divide the two housing units at the underground and ground floor. The IWA-1 typology (Figure 1.9c) is a one-leaf panel wall with total thickness of 12 cm. The hollow clay bricks, with dimensions of 8 x 25 x 25 cm, are placed with the 25 cm side parallel to the wall plane and the 8 cm side oriented in the thickness direction. The two sides of the wall are covered with a plaster layer with thickness of about 2 cm. This typology is used for most of the internal infill masonry walls at the underground and ground floor. It is worth noting that only the ground floor is completely surrounded by the external infill masonry walls, while in the attic floor only the East and West sides are filled with this wall typology, since the roof is sloping and not so much high.

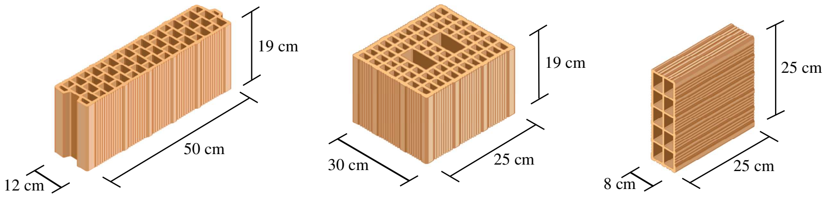

Figure 1.8 Bricks used for the infill masonry walls in Building 2.

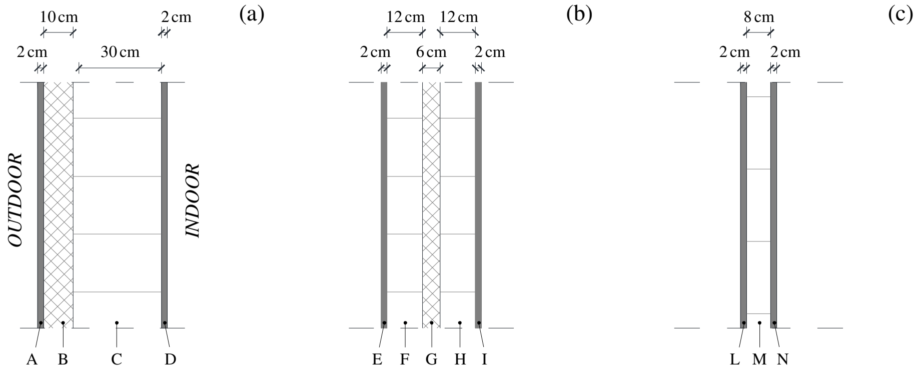

OUTDOOR	
A	Plaster
B	Insulation layer
C	Hollow clay bricks
D	Plaster
INDOOR	

E	Plaster
F	Hollow clay bricks
G	Insulation layer
H	Hollow clay bricks
I	Plaster

L	Plaster
M	Hollow clay bricks
N	Plaster

Figure 1.9 External and internal infill masonry wall typologies: (a) EWA-0, (b) IWA-0, (c) IWA-1.

At the underground level the external infill masonry walls are absent because this floor is surrounded by retaining r.c. walls. The internal infill masonry walls are built with a fairly uniform plan distribution at the underground and ground floor, while they are completely absent at the attic floor. Table 1.3 presents the specific weights for all the infill masonry wall typologies during the construction processes, namely before and after the plaster realization.

Table 1.3 Specific weight of the infill masonry walls.

Wall typology	Specific weight [kN/m^3]	
	Without plaster	With plaster
EWA-0	8.70	9.80
IWA-0	7.08	8.28
IWA-1	6.52	10.11

1.2. Experimental in situ dynamic tests

1.2.1. Introduction to the ambient vibration measurement and Operational Modal Analysis

To evaluate the experimental modal parameters of the two buildings investigated, which are natural frequencies, mode shapes and damping ratios, Operational Modal Analysis (OMA) based on the acceleration measurements of the buildings were performed.

While in traditional experimental modal analysis (EMA) the forces exciting the test specimen are controlled and normally the testing is carried out in the laboratory, in OMA the forces are just the ones that are naturally present during the operation of the structure and the test should be carried under the actual operating in situ conditions. For a structure in the civil engineering field, typical ambient forces are wind and waves, while for a structure in the mechanical engineering field, they are operating forces on an engine or a gearbox, in both cases nothing is done to control temperature and other conditions that might influence the result. In OMA all modal parameters are to be determined without knowing the excitation forces. Therefore, it is normally assumed that the excitation forces are Gaussian white noise, or at least that spectral densities of these forces are all flat. The random vibration is often characterized by the power spectral density (PSD) function that for a time series $x(t)$ is defined as the Fourier transform of the correlation function $R_x(\tau)$

$$G_{xy}(\omega) = \frac{1}{2\pi}\int_{-\infty}^{\infty} R_{xy}(\tau)e^{-i\omega\tau}\,d\tau \tag{1}$$

The PSD is popular mainly because vibrational modes are clearly indicated by spectral peaks; the area below a PSD for any frequency band is equal to the variance of the corresponding time signal (band-pass filtered to the same frequency band) and therefore the

PSD has a simple physical interpretation of energy distribution (from which the name "power" spectral density). One of the most important equations in random vibrations is the fundamental theorem that relates the product of the PSD matrix of the input and the FRF matrix of the system to the PSD matrix of the response

$$G_y(\omega) = \overline{H}^*(i\omega) G_x(\omega) \overline{H}^T(i\omega) = \overline{H}(-i\omega) G_x(\omega) \overline{H}(i\omega) \tag{2}$$

The last equation follows from the identity $\overline{H}^*(i\omega) = \overline{H}(-i\omega)$ and from the fact that the transfer function is symmetric. Other central relations in random vibrations are the modal decompositions of the correlation function and PSD function matrices. The modal decomposition of the correlation function matrix is due to James et al., 1995. Expressing a general response by its modal decomposition and assuming white noise input where the correlations functions all degenerate to the Dirac delta functions it can be shown that the correlation function matrix for negative times $R_{y-}(\tau)$ and for positive times $R_{y+}(\tau)$ is given by

$$\begin{aligned} R_{y-}(\tau) &= 2\pi \sum_{n=1}^{N} \left(b_n \gamma_n^T e^{-\lambda_n \tau} + b_n^* \gamma_n^H e^{-\lambda_n^* \tau} \right) \\ R_{y+}(\tau) &= 2\pi \sum_{n=1}^{N} \left(\gamma_n b_n^T e^{\lambda_n \tau} + \gamma_n^* b_n^H e^{\lambda_n^* \tau} \right) \end{aligned} \tag{3}$$

where b_n is the mode shape for the mode n and γ_n is a vector describing the modal participation of the considered mode. It is important to note that the negative time part of the correlation function matrix $R_{y-}(\tau)$ is in fact a free decay because it is written as a linear combination of modal contributions (terms proportional to the mode shape times a complex exponential), whereas the positive time part $R_{y+}(\tau)$ is in fact only a free decay if it is used in its transposed form so the terms $\gamma_n\ b^T_n$ turn into the form $b_n\ \gamma^T_n$ and the response becomes proportional to the mode shapes. This means that whenever correlation functions are used as free decays, using the positive part of the correlation function matrix, the matrix must be used in its transposed form. The decomposition in the frequency domain can be found by taking the Fourier transform of (3) or by assuming a with noise input and using the fundamental theorem (2), (Brincker, 2000)

$$G_y(\omega) = \sum_{n=1}^{N} \left(\frac{b_n \gamma_n^T}{-i\omega - \lambda_n} \frac{b_n^* \gamma_n^H}{-i\omega - \lambda_n^*} + \frac{\gamma_n b_n^T}{i\omega - \lambda_n} + \frac{\gamma_n^* b_n^H}{i\omega - \lambda_n^*} \right) \tag{4}$$

As it appears, in the frequency domain we do not have a modal decomposition that can be considered as a linear combination of free decays from system, because some terms are proportional to the mode shapes and some terms are proportional to the modal participation vectors. This is due to the fact that when taking the Fourier transform of (3) the terms from the negative and the positive time axes get mixed so that the first two terms in (4) are from the negative time axis and the last two ones are from the positive time axis. Including only the positive part of the correlation function matrix in the Fourier transform defines the so-called half spectrum matrix that consists only of the two last terms of (4) and, as we can see, the half spectrum matrix is a spectral representation of free decays, but again only in its transpose form. It is important to note that by using the transposed correlation function matrix as free decays in any identification technique (or using its counterpart in the frequency domain as the corresponding half spectrum) we see that we have as many free decays as we have sensors. Therefore OMA is so to speak born as a multiple input technique. From (2) we can see that a reduced rank of the input spectral density matrix $G_x(\omega)$ will reduce the rank of the output spectral density accordingly, so normally it is a common assumption in OMA that the excitation of the structure is also multiple input, that is, using many independent excitation sources.

Concerning the testing part it is extremely important to make a well-defined plan for the test, in order to guarantee that all measurements are carried out well, all data have the required quality and the testing is well documented. It is also important to ensure a reasonable signal-to-noise ratio by making sure that the noise floor of the sensors (and that of the total measurement system) is well below the excepted response level.

As regard the signal processing, the information from the random signals are extracted by calculating correlation functions. However, before doing that it is important to go through some initial pre-processing steps: validate data quality (check for clipping, dropouts, etc.), calibrate signals to refer to physical units and detrending (remove mean or slowly varying trend). Some optional pre-processing steps often used in OMA are the adjustment of the sampling frequency (up sampling and down sampling, also denoted decimation), filtering to reduce the frequency band (low-pass, band-pass or high-pass filters) and integration/differentiation of signals. When the pre-processing has been performed the correlation function matrix can be estimated by direct calculation following the simple and unbiased estimator

$$\hat{R}(k) = \frac{1}{(N-k)\Delta t}\sum_{n=1}^{N-k} y(n)y^T(n+k)\Delta t = \frac{1}{N-k}\sum_{n=1}^{N-k} y(n)y^T(n+k) \tag{5}$$

The tradition is to calculate the spectral density first by segmenting the data and using (Brandt, 2011)

$$\hat{G}(\omega) = \frac{1}{S}\sum_{s=1}^{S} \tilde{y}_s(\omega)^* \tilde{y}_s^T(\omega) \tag{6}$$

where $\tilde{y}_s(\omega)$ is the Fourier transformed response of segment *s*. Then, the correlation function can be found by inverse Fourier transform. In OMA one should be careful with possible bias on spectral function and correlation function estimates that eventually might result in large errors in the damping values. In the last years it has become popular to skip the negative part of the correlation functions so that according to (3) when taking the Fourier transform to get the spectral density the two first terms in (4) disappear and we obtain a so-called half spectrum that is a spectral representation of time domain free decays.

To estimate the modal properties, both identification techniques in time and frequency domain can be used. In time domain identification (TD-ID) it is normal to use parametric models obtained by least square (LS) fitting. In practice this is done by formulating an overdetermined set of equations that is solved using the pseudo inverse of the equation matrix. Frequency domain (FD) methods are mainly popular due to their ability to appeal to our intuition by the nice plots where we can inspect spectral peaks and have an idea about modal participation by evaluating the height of each peak and the damping by evaluating its width. The disadvantage is that they tend to suffer from bias problems due to leakage because even though the spectral density can be estimated so that it is asymptotically unbiased (bias is zero when information approaches infinity), in practice we need to deal with a limited amount of information and thus the leakage bias will tend to lead to overestimation of the damping in the frequency domain.

1.2.2. Instrumentation and sensors arrangement

For both buildings case studies the instrumentation used to perform the dynamic tests consists of low-noise uniaxial piezoelectric accelerometers with sensitivity of 10 V/g, frequency range of 0.07 – 300 Hz and 1 μg of resolution. The sensors were connected to a 24-bit data acquisition system by means of coaxial cables. A laptop equipped with a basic software developed in LabView ambient was used in order to store data automatically during the tests and to plot the frequency spectra of the accelerations recorded. For each test, 2000 seconds long records sampled at a rate of 2048 Hz were acquired. This time length provides enough data to obtain modal parameters with a good accuracy (as reported in Canteni, 2005) where a length of the acquired time window of about 1000 – 2000 times the period of the fundamental mode is recommended. All the recorded data were processed with standard signal processing techniques before performing the modal analysis. Initially, data were carefully inspected in order to cut those parts characterized by anomalous behaviours (signal clipping, intermittent noise, spikes and so on) due to sensor or measurement chain malfunctioning or due to signal saturation. Then, the contribution of spurious trends is eliminated by subtracting the contribution obtained by fitting the signals with a polynomial function and the high frequency contribution is eliminated by filtering with a Butterworth low pass filter characterized by order 4 and cut-off frequency of 20 Hz. Finally, signals are down-sampled at 51.2 Hz to decrease the number of data and make faster the successive analysis. The obtained frequency range contains all the vibration modes that significantly contributes to the dynamic response of the buildings.

The accelerometers were positioned over the floor slabs of the buildings and the arrays are displayed in Figure 1.10 for Building 1 in Fermo and in Figure 1.11 for Building 2 in Ancona. For Building 1, the sensors were placed at each floor (ground, first, attic and roof floors) except at the underground floor. Six accelerometers were positioned at each level distributed throughout the building, two measuring in longitudinal direction (North-South direction) and four measuring in transverse direction (East-West direction). This high number of sensors at each level is necessary to catch those vibration modes that also involve a deformation of the floor. For Building 2, four accelerometers were positioned at all levels (underground, ground and attic floors), two measuring in longitudinal direction (East-West direction) and two in transverse direction (North-South direction). In this case, a few number of accelerometers is enough to catch the vibration modes of the building since the small size of the structure allows to consider the floors rigid in the horizontal plane. Figure 1.12 and Figure 1.13 show some pictures related to the arrangement of the accelerometers on Building 1 and on Building 2, respectively.

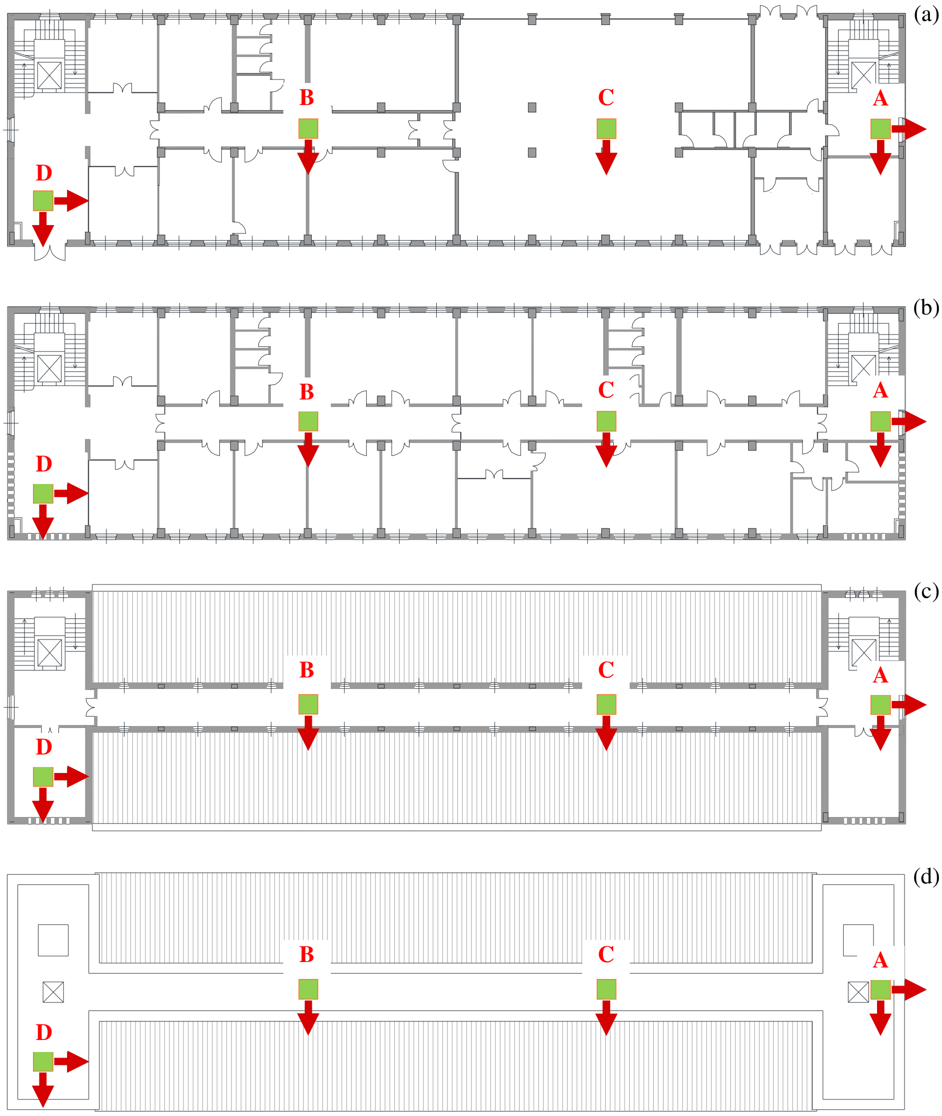

Figure 1.10 Sensors arrays in Building 1: (a) ground floor, (b) first floor, (c) attic floor, (d) roof.

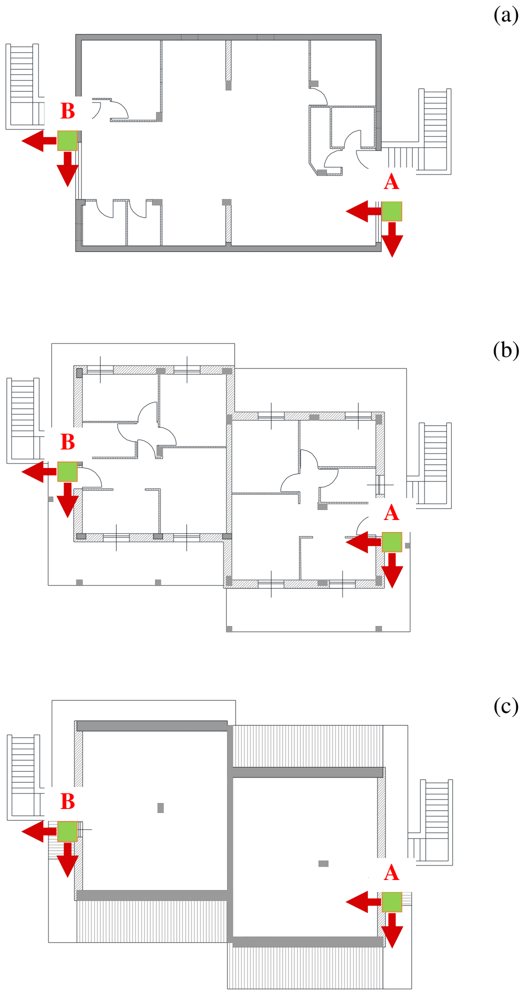

Figure 1.11 Sensors arrays in Building 2: (a) underground floor, (b) ground floor, (c) attic floor.

Figure 1.12 Arrangement of the accelerometers on Building 1.

Figure 1.13 Arrangement of the accelerometers on Building 2.

1.2.3. Systems identification during the construction processes

Ambient vibration (low-amplitude with noise) data were recorded on the buildings at key stages of the construction processes. For all the dynamic tests performed the input was not controlled but was assumed to have a flat spectrum such as a white noise; therefore, to identify the modal parameters of the buildings the output-only technique working in the time domain called Covariance-driven Stochastic Subspace Identification (SSI-COV) was used.

As regard Building 1, the tests were conducted on August 25, 2016 once the construction of the structural skeleton was finished and only the infills at the underground floor were realized and, in some cases, plastered (almost bare building structure) (Figure 1.14). Another test was conducted on November 7, 2016 when the construction of all the infills was completed (Figure 1.15) and, in particular, all the infills of the underground and ground floor were realized with plaster, while the infills of the first and attic floor were partially plastered. The infill masonry walls built on the two pavilions located at the ends of the building were completed only at the ground floor in the South pavilion, while for all the others, only the external facing brick layer was completed. For Building 2 the tests were performed on June 1, 2016 at the end of the construction of the bare building structure (Figure 1.16) and on July 21, 2016 after the construction of the infills (without plaster) only at the ground level (Figure 1.17).

For what concern Building 1, the first three natural frequencies obtained for the two construction stages mentioned above are listed in Table 1.4 and the relevant mode shapes are displayed in Figure 1.18. Considering only the bare building structure, the first vibrational mode is a translational mode in the longitudinal direction (North-South direction), the second one is mainly a translational mode in transverse direction (East-West direction) but it is affected by the fact that the floors are not rigid in their plane and, in particular, they have a "C" shape deformation with higher modal displacements at the centre of the building and lower at the ends. The third vibrational mode is rotational. After the construction of the infill masonry walls the vibrational modes order and the mode shapes are the same as before, but the natural frequency values are significantly higher, as expected. In detail, the first natural frequency value has doubled, the second and the third ones are increased almost by 50%. In conclusion, it can be observed that the addition of the infill masonry walls within the global f.e. model of Building 1 leads to notably higher values of natural frequency but keeps constant the modes order and the mode shapes.

As regards Building 2, Table 1.5 and Figure 1.19 reported the first three natural frequencies and the relevant mode shapes resulting from ambient vibration tests at the two key stages. Considering the test performed on June 1, 2016 (before the infills) the first and second vibrational modes are translational modes in the East-West direction and in the North-South direction, respectively. The third mode is rotational. After the construction of the infill masonry walls, the modes order is the same as before but the first two mode shapes (the translational ones) have, in this case, a significantly rotational component. Here as well the natural frequency values obtained in the case without infills are lower with respect to those obtained with the infills and, in particular, the values roughly double for all three modes considered. It can be concluded that the addition of the infills within Building 2 leads to a variation of the first two mode shapes whose however remain mainly translational and leads to a notably gain on frequency values. The modes order, instead, remains unchanged.

Figure 1.14 Building 1: construction process on August 25, 2016.

Figure 1.15 Building 1: construction process on November 7, 2016.

Figure 1.16 Building 2: construction process on June 1, 2016.

Figure 1.17 Building 2: construction process on July 21, 2016.

Table 1.4 Experimental natural frequencies for Building 1.

Mode	Mode name	Frequency [Hz]	
		August 25, 2016	November 7, 2016
1	1st N-S	2.57	5.24
2	1st E-W	3.32	5.75
3	1st Rot	4.12	6.41

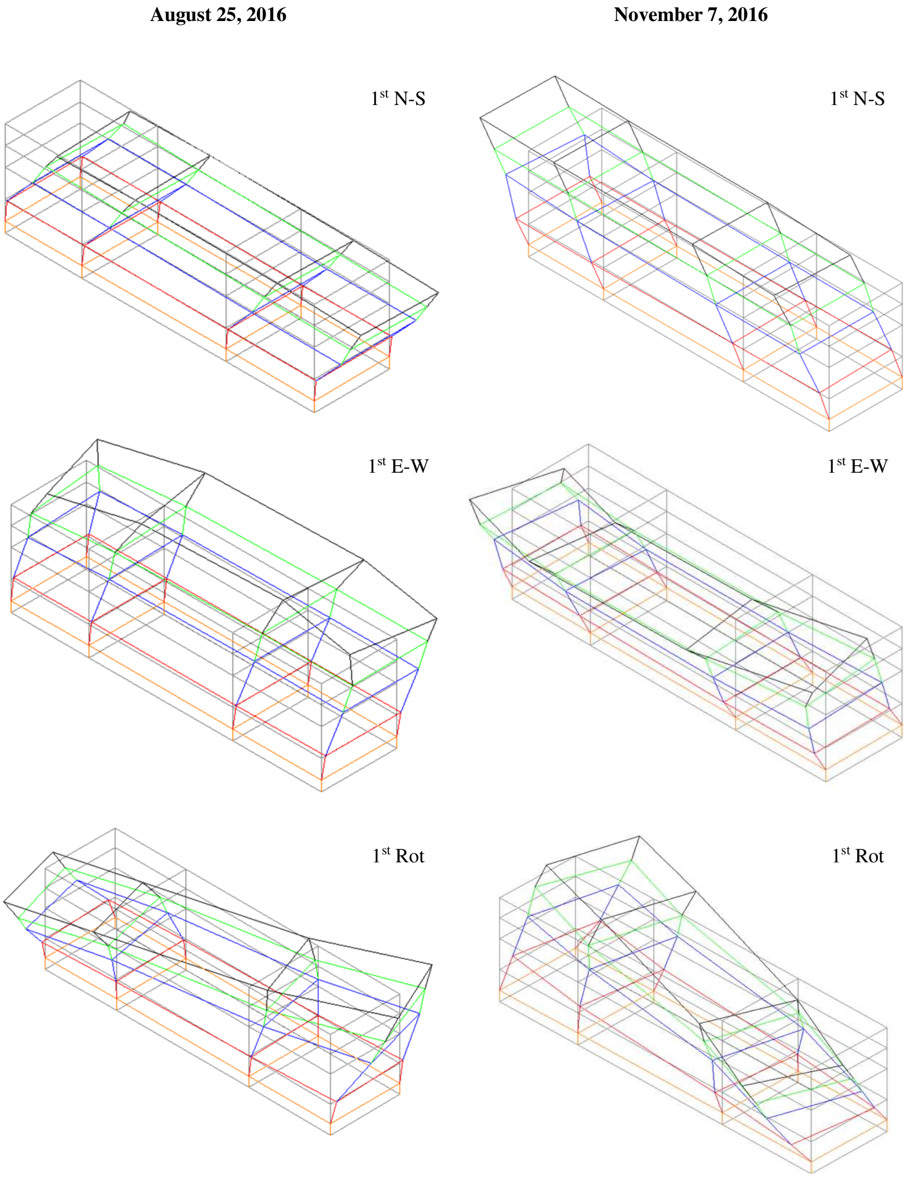
August 25, 2016

November 7, 2016

Figure 1.18 Experimental mode shapes for Building 1.

Table 1.5 Experimental natural frequencies for Building 2.

Mode	Mode name	Frequency [Hz]	
		June 1, 2016	July 21, 2016
1	1st N-S	5.77	10.71
2	1st E-W	6.12	13.04
3	1st Rot	7.85	15.75

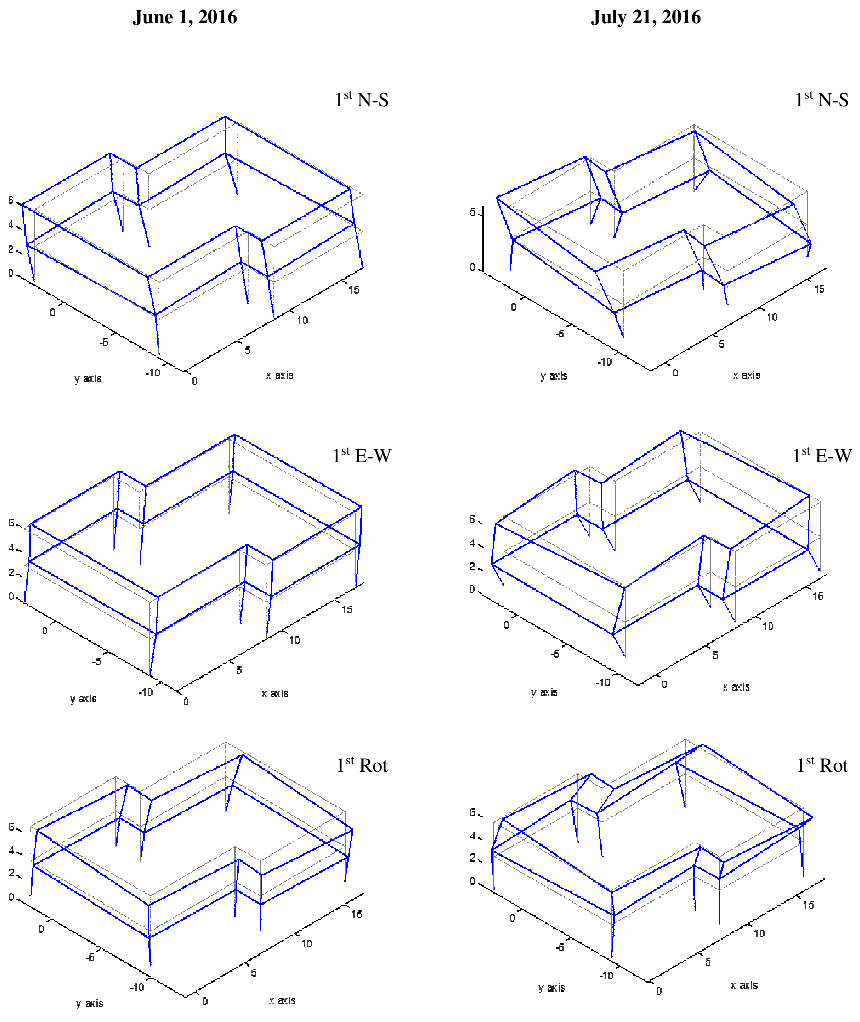

Figure 1.19 Experimental mode shapes for Building 2.

Chapter 2.

Dynamic tests on in situ infill masonry walls

2.1. Tested infill masonry walls description

2.1.1. Tested infills of Building 1

Considering the Building 1 case study located in Fermo, three infill masonry walls were evaluated and tested. The choice of these walls was made with the aim to investigate the most representative typologies of masonry infills used to realize the external and internal partitions of the building. They are located on the underground floor and made with hollow clay bricks with different thickness and all of them are surrounded by the r.c. frame of the structure. Figure 2.1 shows the arrangement of the walls inside the building. All the tested walls do not have openings.

The W1-F wall is an internal partition that divides the garage from the offices and provides a safety barrier against fires. The constructive typology is IWF-2, which is representative of several internal partitions and external walls. The bed joints of this wall have thickness of about 1 cm, while the head joints are almost completely absent. The W2-F wall is the interior part of a composite external infill masonry wall built with the IWF-0 typology, so it is representative for the 8 cm thick infill masonry walls. The joints are similar to those of the IWF-2 typology, that is thickness of about 1 cm for the bed joints and head ones nearly absent. Only the exposed side of this wall is covered with plaster, as it is part of a composite wall. The W3-F wall is an internal partition between two offices with IWF-1 constructive typology, one of the most used for the interior partitions. The bed joints have thickness of about 1 cm, while, the head joints are also in this case almost completely absent. The four border sides of all the tested infills are constrained by beams and columns of the r.c. frame of the building. Figure 2.2 displays some pictures referring to the construction process of the infills, while in Figure 2.3 the geometry of the tested infill walls is illustrated.

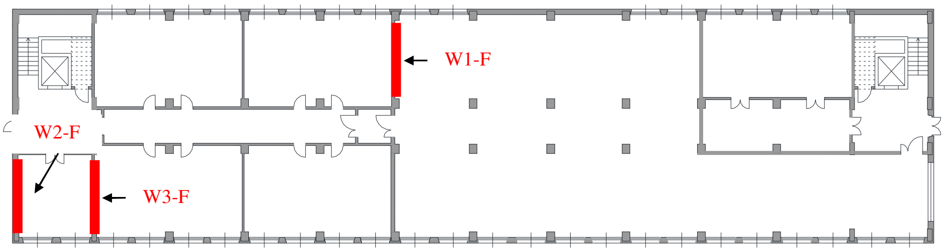

Figure 2.1 Layout of the tested infill masonry walls at the underground level of Building 1.

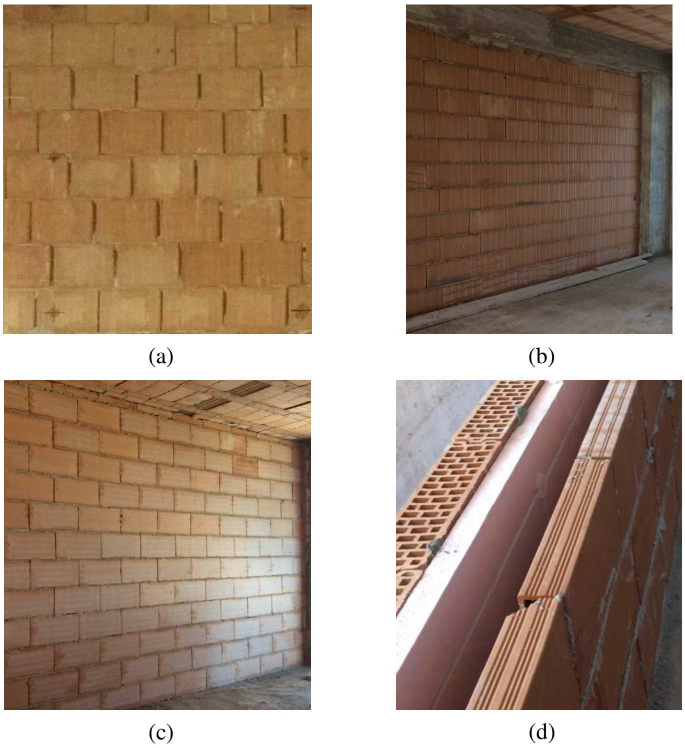

Figure 2.2 Infill masonry walls typology: (a) wall W1-F, (b) wall W3-F, (c) wall W2-F, (d) section of the wall W2-F.

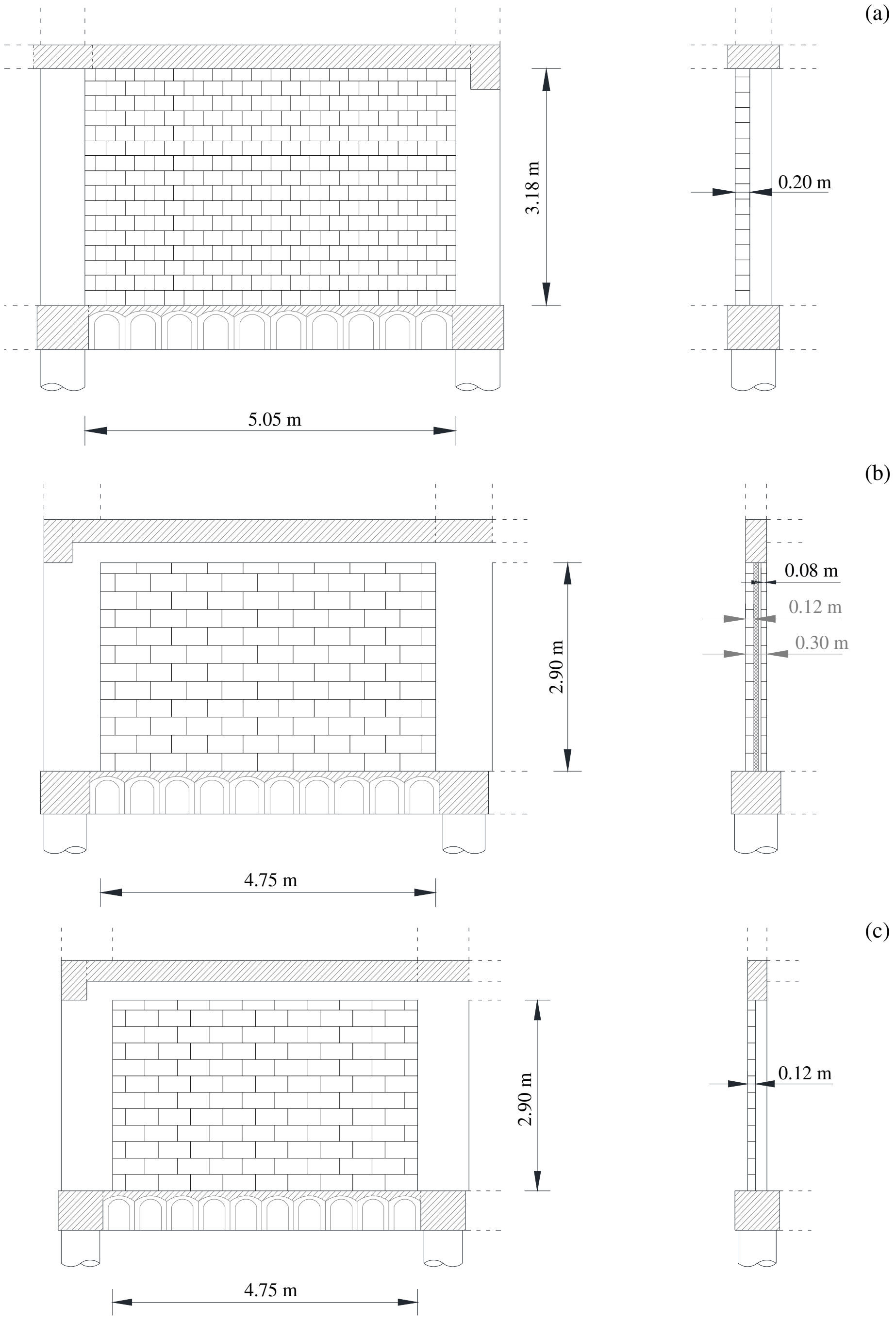

Figure 2.3 Geometry of the tested infill walls: (a) wall W1-F, (b) wall W2-F, (c) wall W3-F.

2.1.2. Tested infills of Building 2

For what concerns the Building 2 case study, which is located in Ancona, three infill masonry walls were tested and investigated. Also in this case, the choice of the walls was made with the aim to investigate the most representative typologies of masonry infill walls used for the internal and external partitions of the building. They are located on the ground floor and made of hollow clay bricks with different thickness. Differently from the previous case study (Building 1), the r.c. frames of the structure confine only some perimeter sides of the walls. Figure 2.4 shows the arrangement of the walls inside the building. There are no openings on the tested walls.

The W1-A wall is an external infill wall built with the EWA-0 constructive typology and it is representative for all the external walls. The bed joints have thickness of about 1 cm, while the head joints are not completely filled with mortar. All the border sides of this wall are constrained by the r.c. members of the structure. The wall W2-A is an internal partition that divides two housing units at each floor and it is built with the IWA-0 constructive typology. The bed joints have thickness of about 1 cm, while the head joints are almost completely absent. Three sides of the wall are constrained by the r.c. frame of the structure, in detail the upper and lower sides and one of the two vertical sides; in the other one there is an internal infill built orthogonally with respect to the considered wall. The W3-A wall is an internal partition between two rooms realized with the IWA-1 constructive typology and it is representative for almost all the internal partitions. The bed joints have thickness of about 1 cm, while, also in this case, the head joints are almost completely absent. Only one side of the wall is constrained by a column of the r.c. frame, while the upper and lower sides are constrained by the ground floor slab and the first floor slab, respectively. The other vertical side is built adjacent to an orthogonal internal wall 12 cm thick. Figure 2.5 illustrates the geometry of the tested infill walls, while Figure 2.6 displays some pictures of the infill walls construction process.

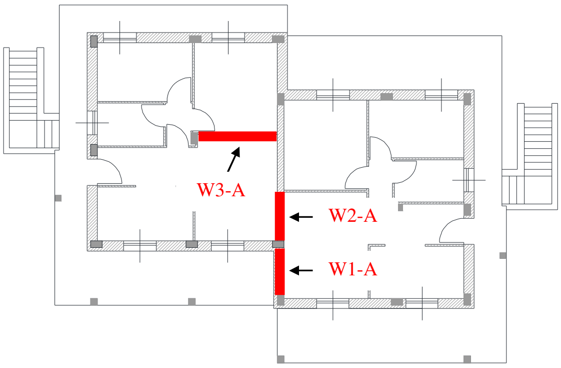

Figure 2.4 Layout of the infill walls tested at the ground floor of Building 2.

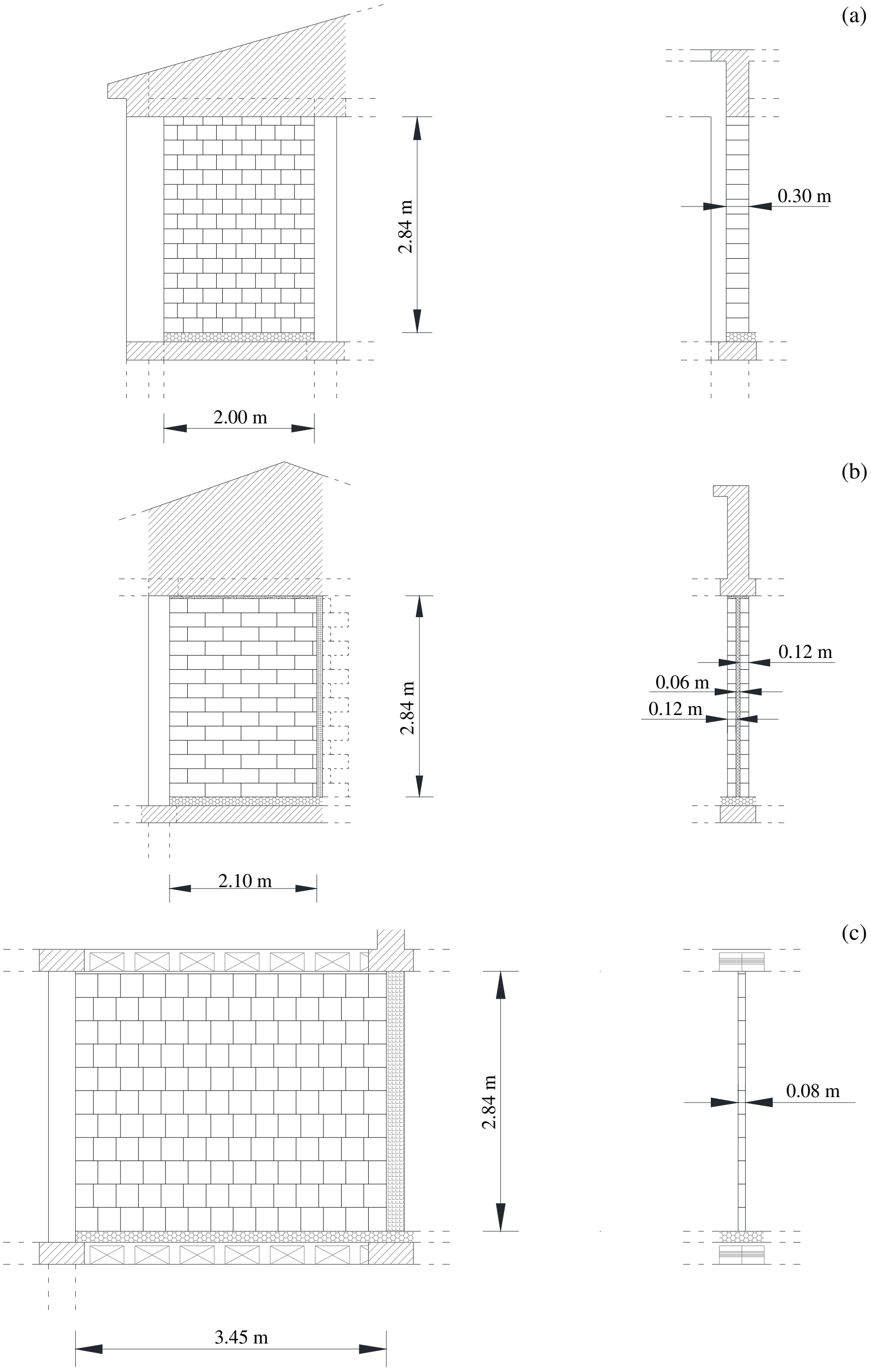

Figure 2.5 Geometry of the tested infill walls: (a) wall W1-A, (b) wall W2-A, (c) wall W3-A.

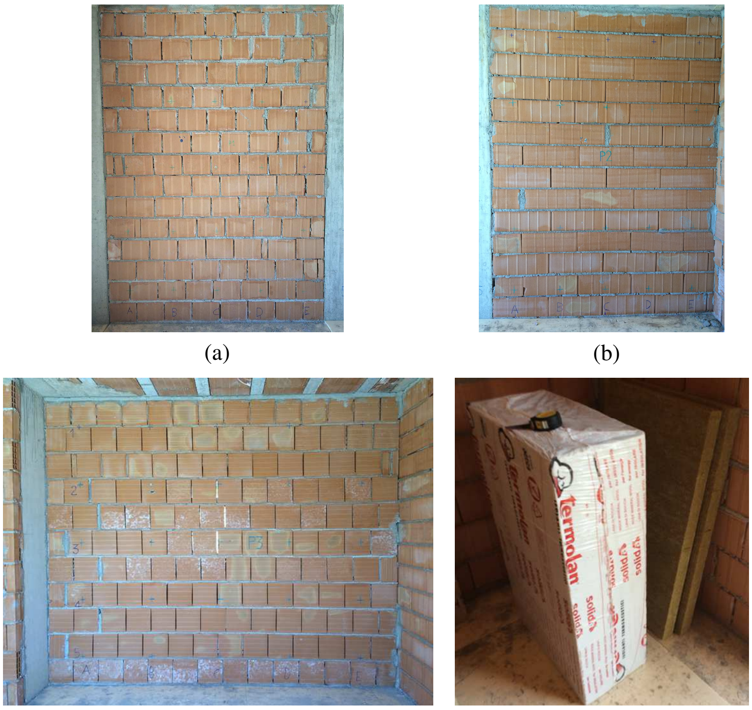

(a) (b)

(c) (d)

Figure 2.6 Infill masonry walls typology: (a) wall W1-A, (b) wall W2-A, (c) wall W3-A, (d) glass wool used inside the wall W2-A.

2.2. Introduction to impact tests and Experimental Modal Analysis

To perform an Experimental Modal Analysis (EMA) it is necessary to acquire data with the aim of identify the frequency response function of a test structure, while for time–domain analysis the target is to achieve either the free-decaying due to an impulse or the response due to ambient excitation. The method used in this work is to excite a structure with a known input force and measure both the forces and responses on the structure. As a result, we obtain the data for a group of Frequency Response Functions (FRFs) that can be suitable for modal analysis to derive the modal model of the structure. EMA is a technique that attempt to do a system identification, which means that the structure is a “black box” that needs to be decoded. The traditional approach is to provide the “black box” with a known input, measure the output and proceed with the identification. The input force is known, so that the FRF can be derived directly from both the input force and the response measured. The excitation force can be random, sinusoidal, periodic or due to an impact. From a theoretical point of view, the type of force does not affect the FRF, which is defined as the ratio between the response and force. Practically the input force needs to be characterised by an amount of energy and frequency components that are able to excite all the vibration modes of interest and allow to minimize errors in signal processing, leading to the formation of accurate FRF data. The assumption that the test structure behaves linearly is essential to attaining accurate FRF measurement. It is known that the modal analysis resulting from the measured FRF data of a structure which does not exactly follow linearity assumption, may only represent a linearized mathematical model for the structure. The other essential assumption is the reciprocity property of the structure. In addition, FRF measurement cannot succeed if the dynamic properties of a structure vary during the measurement. For this reason, it is required that the structure is time-invariant. FRF data are not the only type of data acquired for modal analysis. As known, for a special category of modal analysis that utilizes the responses in time history, either free vibration response or impulsive response function data are needed. There are also practical cases where laboratory set-up for force excitation is not feasible. Instead, vibrational response due to ambient excitations can be readily measured.

A typical measurement set-up should have three constituent parts. A simple single input and single output case are taken into account as an example. The first part is responsible for the excitation force generation and for its application to the test structure; the second part deals with the response data measurement and acquisition. Finally the third part provides signal processing capacity to derive FRF data from the measured force and response data (Figure 2.7). The first part of the measurement set-up is an excitation mechanism that applies a force of sufficient amplitude and frequency contents to the structure. There are different types of excitation equipment that are able to excite a structure; in this work, a hammer is used. The hammer is a device that produce an excitation force pulse to the test structure. It consists of a hammer tip, a force transducer, a balancing mass and a handle. To alter the hardness the hammer tip can be changed. Typical materials for the tip are rubber, plastic and steel. The hardness of the tip, together with that of the structure surface to be tested, are directly related to the frequency range of the input impulse force. For a hard tip striking on a hard surface, it is expect that the force pulse to distribute energy to a wide range of spectrum. This is the only mechanism to control the frequency components of excitation in a hammer test. An accelerometer is the most common sensor for modal testing. It measures acceleration of a test structure and outputs the signal in form of voltage. This signal needs to be transformed by a signal conditioner before its processing by an analyser, or other hardware or software. The accelerometer does not assume the properties of the measured structure such as linearity. An accurate accelerometer only records faithfully the acceleration at the measurement location. A most common type of accelerometer is the piezoelectric one as illustrated in Figure 2.8. Piezoelectricity means the phenomenon of strain inducting a change in the shape of a crystal thus leading to the change of electric charge. The main parameters affecting the performance of piezoelectric accelerometers are: the frequency response property, the sensitivity and its stability under temperature change, cross-axial sensitivity and base strain.

For what concerns the excitation forces, the impact excitation is adopted. The time-domain force signal for impact excitation is a pulse with uncontrollable frequency contents. In terms of hardware involved, impact excitation is a relatively simple excitation technique compared with shaker excitation. It is convenient and easy to use for field and laboratory tests. Because of no physical connection between the excitation and the structure, impact test avoids the problem of interaction between them. This means that it is possible to measure accurate damping quantities if the signal processing does not add windows or if the additional damping from windowing can be removed. The main disadvantages of impact excitation are as notable as its advantages. It is difficult to control either the force level or the frequency range of the impact. This could affect the signal-to-noise ratio in the measurement, thus resulting in poor quality data. The impact cannot usually be repeated unless a special device, such as a swing for the impact hammer, is used. In addition, some structures are too delicate to be hit by a hammer.

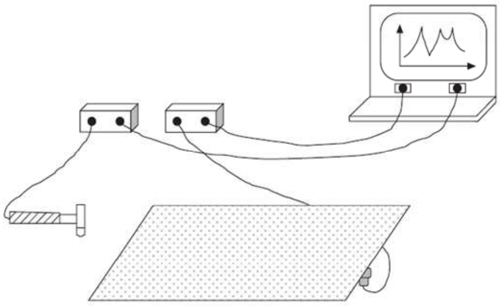

Figure 2.7 A measurement set-up with hammer excitation.

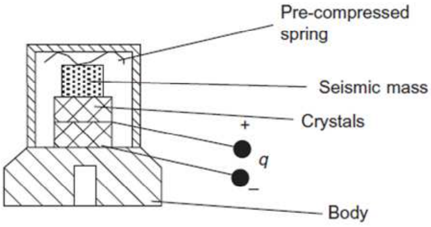

Figure 2.8 Diagram of a piezoelectric accelerometer.

For any measurement, noise exists at both the input and the output. For the idealized measurement situation shown in Figure 2.9 where no noise and measurement errors are present, the FRF can be simply defined as the ratio of two Fourier transforms. The first is the one of the response $x(t)$, denoted as $X(\omega)$, the second is that of the input force $f(t)$, denoted as $F(\omega)$

$$H(\omega) = \frac{X(\omega)}{F(\omega)} \tag{7}$$

From dual channel spectral analysis, an FRF is defined as the cross-spectrum of excitation and response, divided by the auto-spectrum of the excitation. This leads to the following noise-free FRF estimator

$$H_1(\omega) = \frac{S_{FX}(\omega)}{S_{FF}(\omega)} \tag{8}$$

Here, $S_{FX}(\omega)$ is the cross spectrum of excitation and response and $S_{FF}(\omega)$ is the auto-spectrum of the excitation. It has been found in spectral analysis that the same FRF can be estimated both from the ratio of the auto-spectrum of the excitation $S_{XX}(\omega)$ and from the cross-spectrum of excitation and response $S_{FX}(\omega)$

$$H_2(\omega) = \frac{S_{XX}(\omega)}{S_{XF}(\omega)} \tag{9}$$

When the test structure satisfies all assumptions and when noise and measurement errors do not exist, these two different FRF estimators should be equal to the correct FRF:

$$H_1(\omega) = H_2(\omega) = H(\omega) \tag{10}$$

Actually, FRF measurement cannot be noise free. Figure 2.10 shows that the measured force $F^*(\omega)$ is a combined signal of the genuine force $F(\omega)$ and the noise from the input $M(\omega)$. These two are normally inseparable in the time domain but they are not correlated each other. The same happens at the output end. The measured response $X^*(\omega)$ encompasses both the true response $X(\omega)$ and the noise from the output $N(\omega)$. The FRF using $X^*(\omega)$ and $F^*(\omega)$ can be estimated as

$$H_1^*(\omega) = \frac{S_{XF}^*(\omega)}{S_{FF}^*(\omega)} = H(\omega)\left(1 + \frac{S_{MM}(\omega)}{S_{FF}(\omega)}\right)^{-1} \tag{11}$$

or

$$H_2^*(\omega) = \frac{S_{XX}^*(\omega)}{S_{XF}^*(\omega)} = H(\omega)\left(1 + \frac{S_{NN}(\omega)}{S_{XX}(\omega)}\right)^{-1} \tag{12}$$

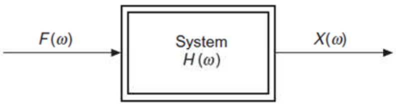

Figure 2.9 System with single input and output.

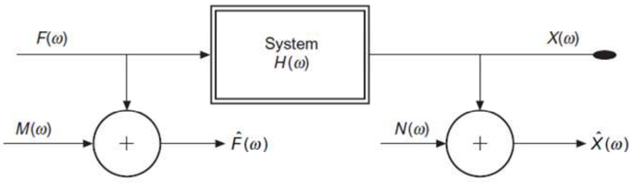

Figure 2.10 FRF estimation with input and output noise.

Neither estimator accounts for the accurate FRF. In terms of amplitude, $H_1^*(\omega)$ is an under-estimator and $H_2^*(\omega)$ is an over-estimator. More insights can be made if we examine $H_1^*(\omega)$ and $H_2^*(\omega)$ close to resonance and anti-resonance, where most dramatic changes of signal-to-noise ratio occur, either at the input or the output end. In case of resonance, the interaction between the excitation and the structure usually results in a peak in the force signal. This allows measurement noise to dominate the input end, while high level of response ensures a large signal-to-noise ratio at the output end, resulting in a significant $S_{MM}(\omega)$ compared with $S_{FF}(\omega)$. Consequently, the FRF estimator $H_1^*(\omega)$ underestimates the true FRF $H(\omega)$ (as shown in Figure 2.11) and the estimator $H_2^*(\omega)$ is accurate. As many modal analysis methods utilize the measured FRF data close to resonance, estimator $H_2^*(\omega)$ should be the choice with respect to $H_1^*(\omega)$.

$$H_1^*(\omega)\Big|_{resonance} = H(\omega)\left(1 + \frac{S_{MM}(\omega)}{S_{FF}(\omega)}\right)^{-1} < H(\omega) \tag{13}$$

$$H_2^*(\omega)\Big|_{resonance} = H(\omega)\left(1 + \frac{S_{NN}(\omega)}{S_{XX}(\omega)}\right)^{-1} \approx H(\omega) \tag{14}$$

In case of anti-resonance, the structure response is usually insignificant when compared with the force input. This allows measurement noise to dominate the output while a high level of force produces a large signal-to-noise ratio at the input end. This results in a significant $S_{NN}(\omega)$ compared with $S_{XX}(\omega)$ and a small $S_{MM}(\omega)$. Consequently, we have the following estimates for the true FRF $H(\omega)$

$$H_1^*(\omega)\Big|_{anti-resonance} = H(\omega)\left(1 + \frac{S_{MM}(\omega)}{S_{FF}(\omega)}\right)^{-1} \approx H(\omega) \tag{15}$$

$$H_2^*(\omega)\Big|_{anti-resonance} = H(\omega)\left(1 + \frac{S_{NN}(\omega)}{S_{XX}(\omega)}\right)^{-1} > H(\omega) \tag{16}$$

The two FRF estimators $H_1^*(\omega)$ and $H_2^*(\omega)$ are related through the coherence function $\gamma^2(\omega)$. For the input $f(t)$ and output $x(t)$, coherence is defined as

$$\gamma_{FX}^2(\omega) = \frac{\left|S_{FX}(\omega)\right|^2}{S_{FF}(\omega)S_{XX}(\omega)} \tag{17}$$

Physically, coherence reflects the causal and linear relationship between the output $x(t)$ and the input $f(t)$. Therefore, $\gamma^2(\omega)$ is equal to zero when the output is not due to the input, equal to one when the output is caused solely by the input. Poor coherence is indicative of poor signal-to-noise ratio, measurement errors, non-linear or time-variant behaviour of the structure or a combination of them. From the definitions of two FRF estimators and coherence, we can find that

$$\gamma_{FX}^2(\omega) = \frac{H_1^*(\omega)}{H_2^*(\omega)} \tag{18}$$

Therefore, if a measurement set up only provides $H_1^*(\omega)$ data, it is possible to convert it into $H_2^*(\omega)$ using coherence data from modal analysis.

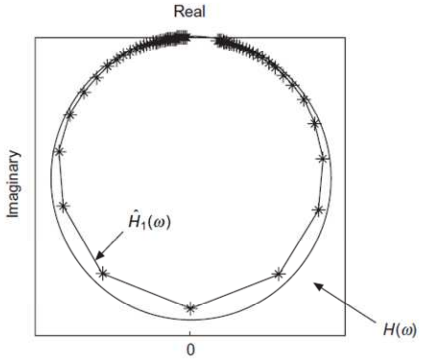

Figure 2.11 $H(\omega)$ and $H_1^*(\omega)$ plot of an SDOF receptance FRF.

2.3. Impact tests on in situ infills

2.3.1. Impact tests set up

To perform the impact tests on the in situ infill masonry walls one PCB Impulse Force Test Hammer (model 086D20) was used. This hammer consists of an integral, Integrate Circuit Piezoelectric (ICP) quartz force sensor mounted on the striking end of the hammerhead. The sensing element is able to transfer impact force into electrical signal for display and analysis. It is structured with rigid quartz crystals and a built-in, micro-electronics, unity gain amplifier. The cable is connected to the end of the handle for convenience, and to avoid connector damage in the event of a “miss hit”. The striking end of the hammer has a threaded hole for the installation of a variety of impact tips. The tip acts to transfer the impact force to the sensor, and protects the sensor face from damage. Tips of different stiffness allow varying the pulse width and frequency content of the force. The hammer size, length, tip and velocity at impact determine the amplitude and frequency content (wave shape) of the force impulse (Figure 2.12). The model selection involves determining the size and mass of the hammer structure, which will provide the force amplitude and frequency content required for proper excitation of the structure under test. The soft tip (red tip) was used to perform the in situ tests and the hammer features with this configuration are listed in Table 2.1. To register the accelerations due to the hammer impacts, two PCB uniaxial shear piezoelectric accelerometers were adopted. The accelerometers have a sensitivity of 0.3 V/g and a frequency range of 1-2000 Hz. Both the hammer and the accelerometers were connected to a 24-bit data acquisition system with chassis, by means of coaxial cables. The acquisition system was connected with a laptop equipped with a LabView software, which was capable to store the data recorded. The acquisition parameters, adopted for all the tests performed, are listed in Table 2.2. The masonry panel was divided with a regular grid of twenty-five points. The two accelerometers, called Acc.1 and Acc.2, were placed on two grid points (C3 and B2 respectively). The tests started applying the impulsive forces at each grid point using the instrumented hammer, while the accelerometers remained always in the same positions.

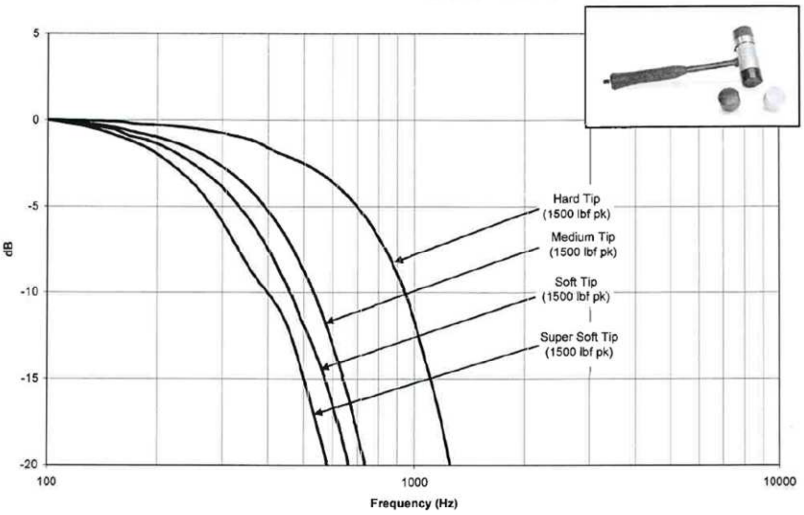

Figure 2.12 Force spectrums of an impact on a stiff steel mass for hammers with their available tips.

Table 2.1 PCB Impulse Force Test Hammer with soft tip features.

Sensitivity	0.23	mV/N
Measurement range	± 22240	N pk
Frequency range	0 - 650	Hz
Resonant frequency	> 12	kHz
Hammer mass	1.1	kg
Tip diameter	5.1	cm
Hammer length	37	cm

Table 2.2 Acquisition parameters.

Sampling frequency	51200	Hz
Number of samples	51200	(each hammer impact)
Time length	1	s (each hammer impact)

Three or more impulsive forces were applied in each impact point to get a reliable data set. Figure 2.13 depicts a schematic layout of the grids used for the infill masonry walls. Examples of recorded impulse and acceleration signals are display in Figure 2.14a. It is worth repeating that the tests were performed before and after the realization of the plaster for all the tested walls (Figure 2.14b).

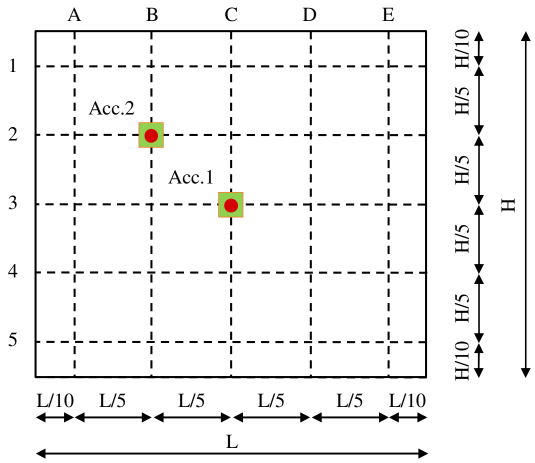

Figure 2.13 Schematic layout of the standard measuring grid on the infill panels.

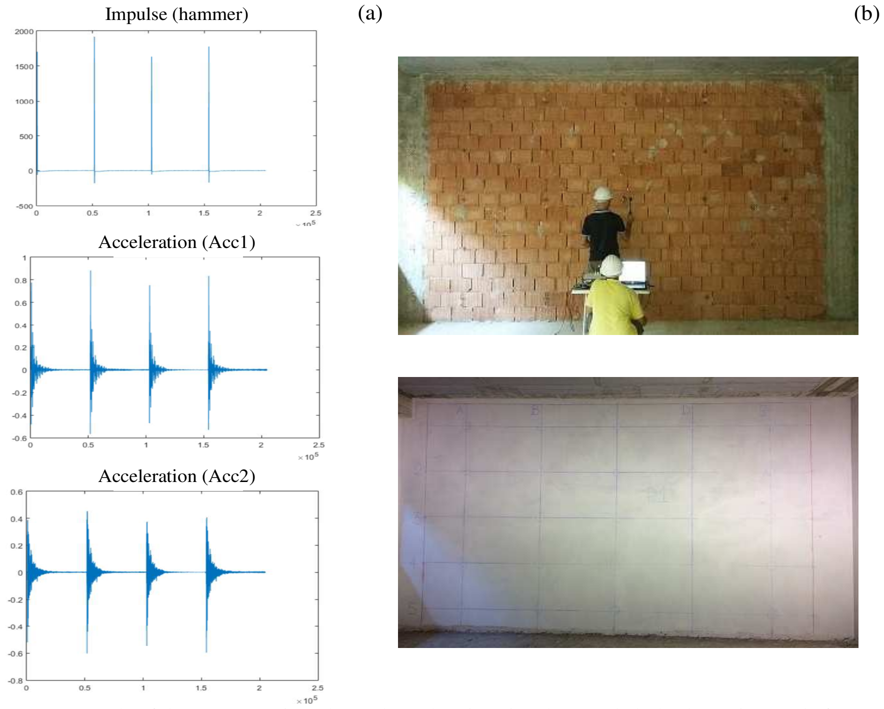

Figure 2.14 Example of the W1-F: (a) impulse and acceleration signals recorded, (b) dynamic tests before and after the realization of the plaster.

2.3.2. *Impact test results*

The results (in terms of modal parameters) obtained from the data recorded during the in situ tests previously described, are representative of the out of plane behaviour of the infill masonry walls. The ModalView software was used to perform the experimental modal analysis through whose the natural frequencies and the corresponding mode shapes were identified.

As regards the infill masonry panels of the Building 1 without plaster, Table 2.3 reports the results in terms of natural frequencies for the wall W1-F, Table 2.4 those related to the wall W2-F and Table 2.5 the ones for wall W3-F. The corresponding mode shapes are displayed from Figure 2.15 to Figure 2.17. The natural frequencies of the same walls after the plaster realization are listed in Table 2.6 for the wall W1-F, in Table 2.7 for the wall W2-F and in Table 2.8 for the wall W3-F. The corresponding mode shapes, instead, are shown from Figure 2.18 to Figure 2.20.

For what concerns the Building 2 case study, it is worth noting that for the wall W1-A, in addition to the external plaster layer was realized an insulation layer of thickness of about 10 cm. As regard the infill masonry panels without plaster, the results in terms of natural frequencies are reported in Table 2.9 for the wall W1-A, in Table 2.10 for the wall W2-A and in Table 2.11 for the wall W3-A; the corresponding mode shapes are displayed from Figure 2.21 to Figure 2.23. After the plaster and insulation layers realization, the natural frequencies for the wall W1-A are listed in Table 2.12, for the wall W2-A in Table 2.13 and for the wall W3-A in Table 2.14; the corresponding mode shapes are shown from Figure 2.24 to Figure 2.26.

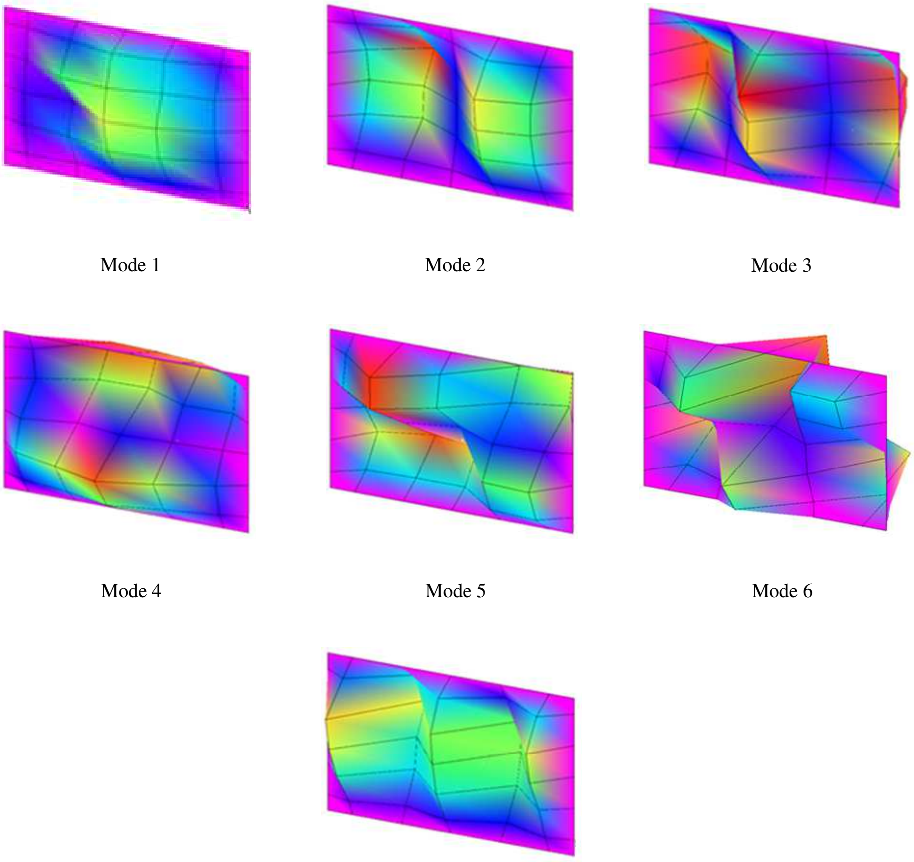

Mode 1

Mode 2

Mode 3

Mode 4

Mode 5

Mode 6

Mode 7

Figure 2.15 Experimental mode shapes for the wall W1-F without plaster.

Table 2.3 Experimental natural frequencies for the wall W1-F without plaster.

Mode	Mode name	Frequency [Hz]
1	I	39.90
2	II-vertical	51.91
3	III-vertical	72.35
4	II-horizontal	111.53
5	IV	121.65
6	VI	139.90
7	V-vertical	140.60

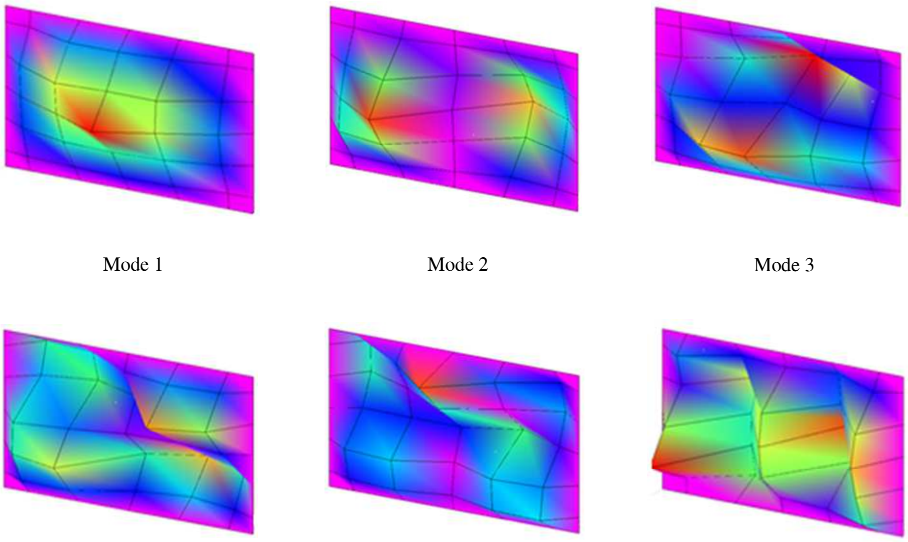

Mode 1 Mode 2 Mode 3

Mode 4 Mode 5 Mode 6

Figure 2.16 Experimental mode shapes for the wall W2-F without plaster.

Table 2.4 Experimental natural frequencies for the wall W2-F without plaster.

Mode	Mode name	Frequency [Hz]
1	I	16.05
2	II-vertical	29.08
3	II-horizontal	39.38
4	IV	51.91
5	VI	74.37
6	V-vertical	119.20

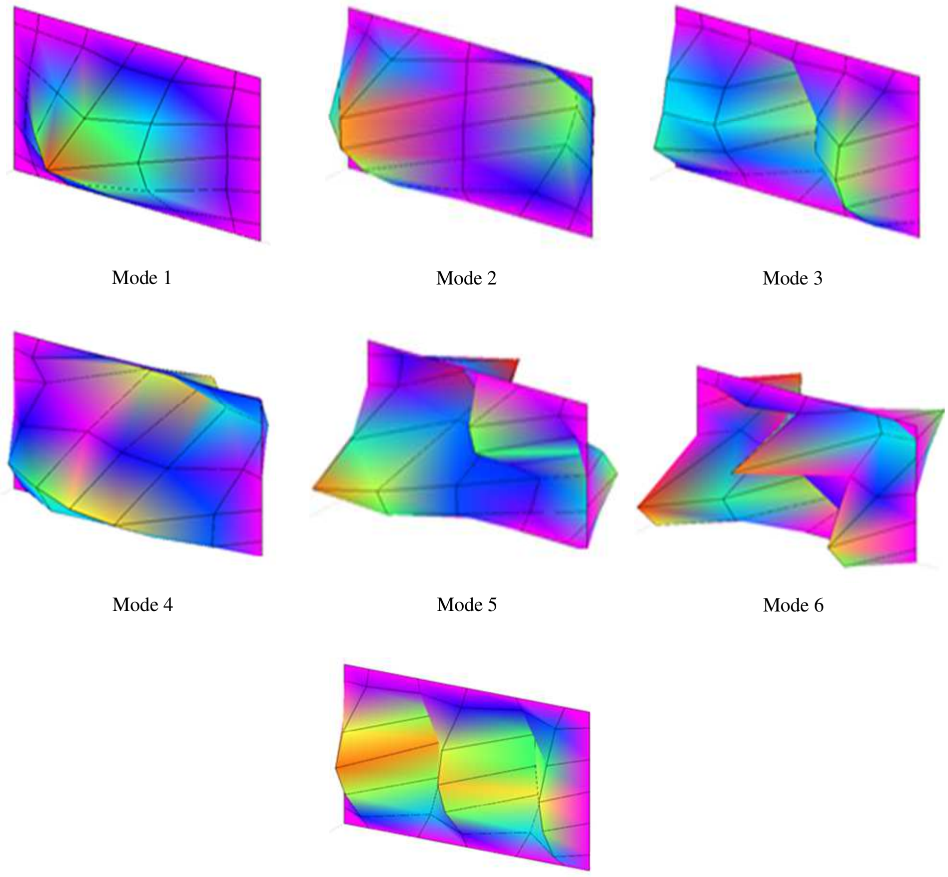
Mode 1

Mode 2

Mode 3

Mode 4

Mode 5

Mode 6

Mode 7

Figure 2.17 Experimental mode shapes for the wall W3-F without plaster.

Table 2.5 Experimental natural frequencies for the wall W3-F without plaster.

Mode	Mode name	Frequency [Hz]
1	I	27.70
2	II-vertical	41.78
3	III-vertical	64.33
4	II-horizontal	75.89
5	IV	93.35
6	VI	113.40
7	V-vertical	136.70

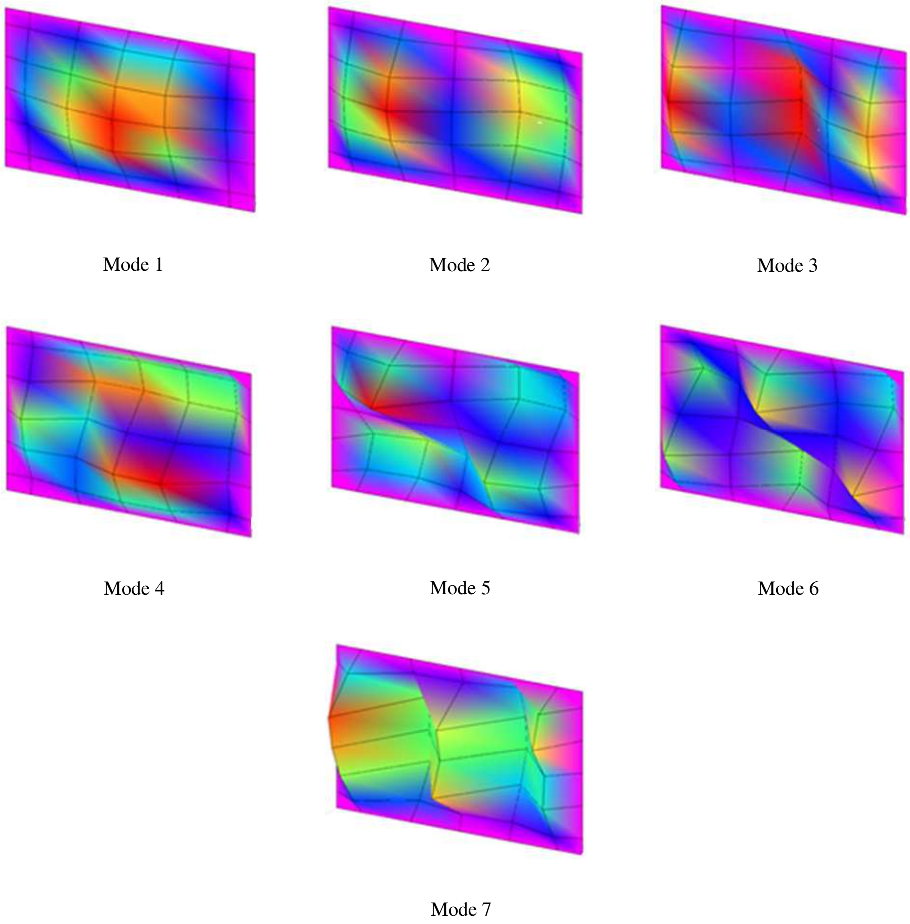

Mode 1

Mode 2

Mode 3

Mode 4

Mode 5

Mode 6

Mode 7

Figure 2.18 Experimental mode shapes for the wall W1-F with plaster.

Table 2.6 Experimental natural frequencies for the wall W1-F with plaster.

Mode	Mode name	Frequency [Hz]
1	I	55.31
2	II-vertical	74.65
3	III-vertical	108.93
4	II-horizontal	139.90
5	IV	159.81
6	VI	189.15
7	V-vertical	201.78

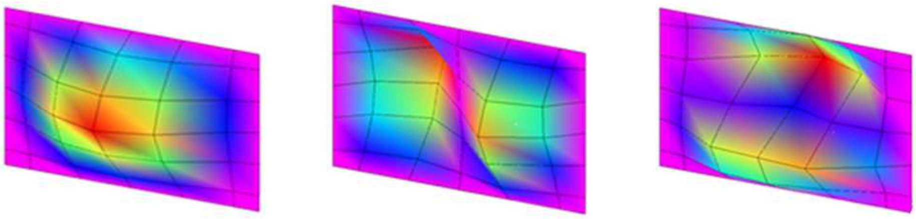

Mode 1 Mode 2 Mode 3

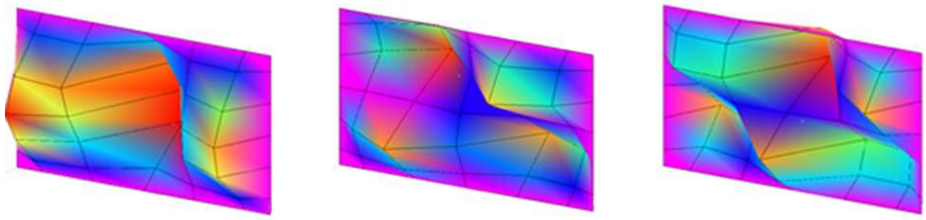

Mode 4 Mode 5 Mode 6

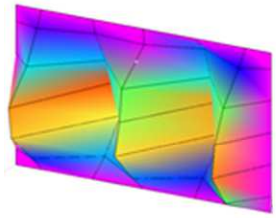

Mode 7

Figure 2.19 Experimental mode shapes for the wall W2-F with plaster.

Table 2.7 Experimental natural frequencies for the wall W2-F with plaster.

Mode	Mode name	Frequency [Hz]
1	I	25.01
2	II-vertical	41.98
3	II-horizontal	57.52
4	III-vertical	68.18
5	IV	72.28
6	VI	99.27
7	V-vertical	157.09

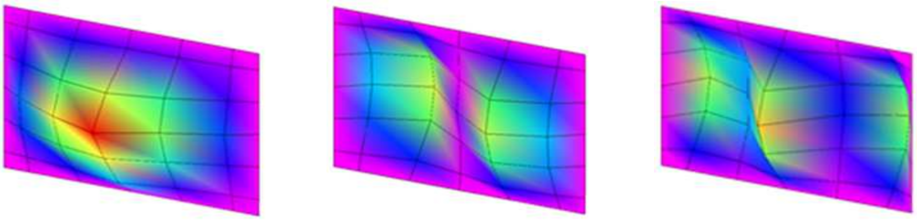

Mode 1 Mode 2 Mode 3

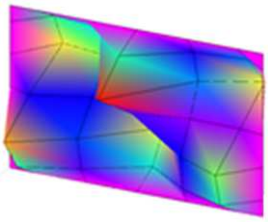

Mode 4 Mode 5 Mode 6

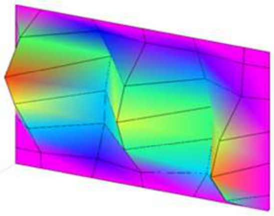

Mode 7

Figure 2.20 Experimental mode shapes for the wall W3-F with plaster.

Table 2.8 Experimental natural frequencies for the wall W3-F with plaster.

Mode	Mode name	Frequency [Hz]
1	I	45.21
2	II-vertical	65.69
3	III-vertical	96.42
4	II-horizontal	116.90
5	IV	135.80
6	VI	165.23
7	V-vertical	193.40

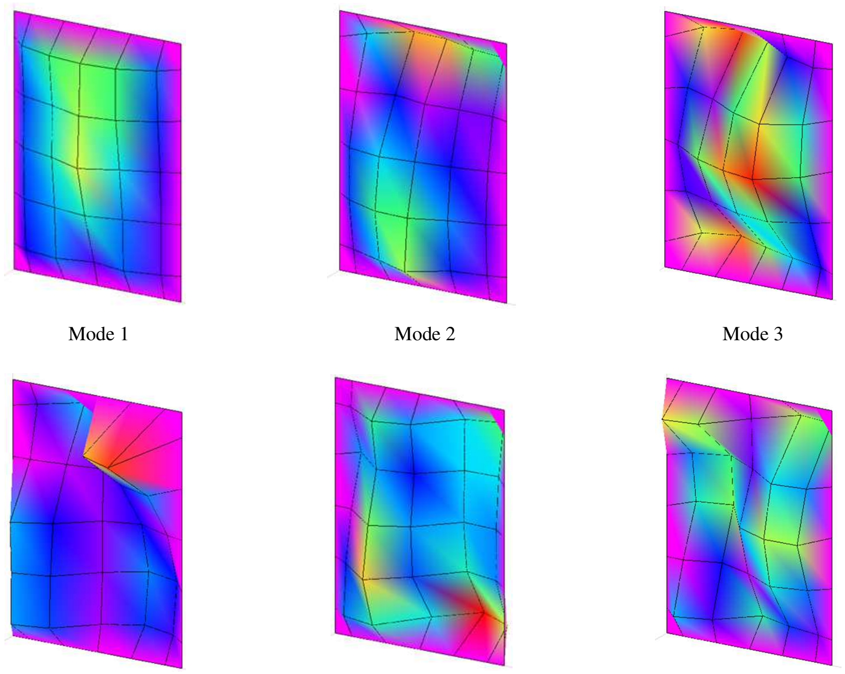

Mode 1 Mode 2 Mode 3

Mode 4 Mode 5 Mode 6

Figure 2.21 Experimental mode shapes for the wall W1-A without plaster.

Table 2.9 Experimental natural frequencies for the wall W1-A without plaster.

Mode	Mode name	Frequency [Hz]
1	I	65.55
2	II-horizontal	91.03
3	III-horizontal	174.27
4	IV	202.50
5	II-vertical	231.00
6	VI	276.33

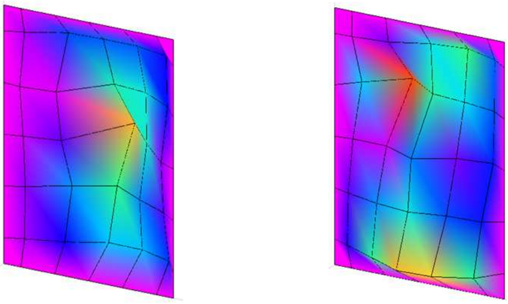

Mode 1 Mode 2

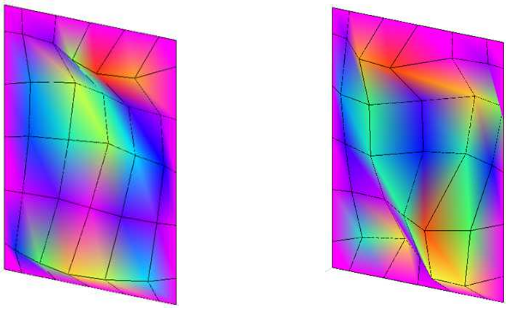

Mode 3 Mode 4

Figure 2.22 Experimental mode shapes for the wall W2-A without plaster.

Table 2.10 Experimental natural frequencies for the wall W2-A without plaster.

Mode	Mode name	Frequency [Hz]
1	I	49.70
2	II-horizontal	71.40
3	III-horizontal	120.48
4	IV	150.10

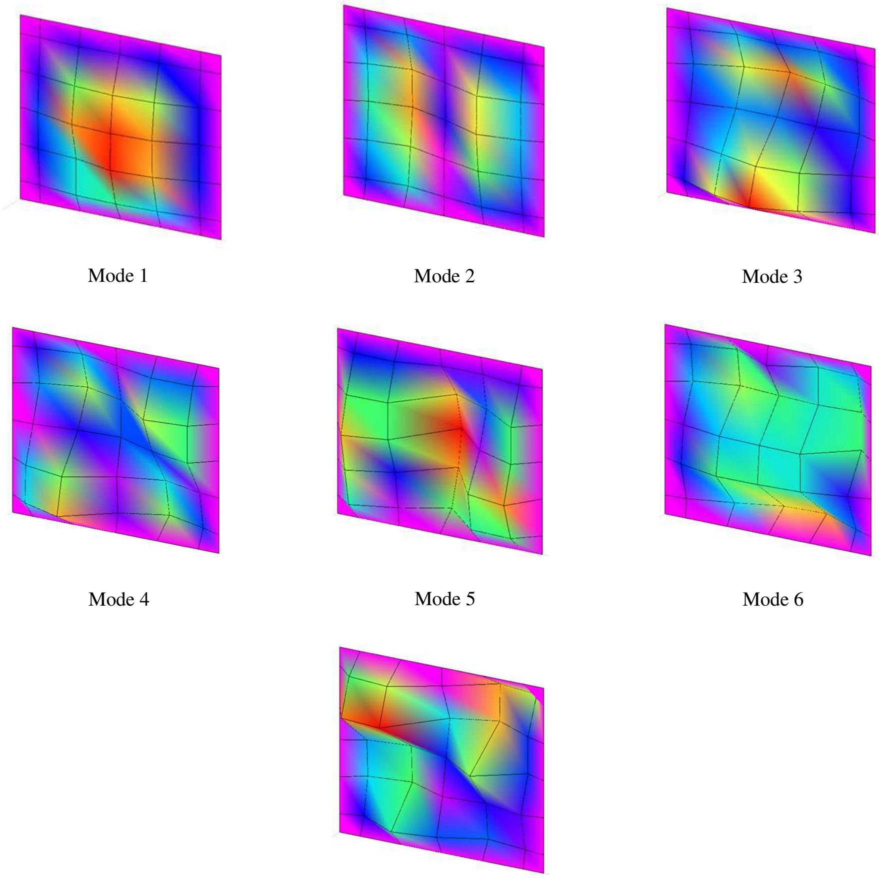

Mode 1

Mode 2

Mode 3

Mode 4

Mode 5

Mode 6

Mode 7

Figure 2.23 Experimental mode shapes for the wall W3-A without plaster.

Table 2.11 Experimental natural frequencies for the wall W3-A without plaster.

Mode	Mode name	Frequency [Hz]
1	I	21.87
2	II-vertical	40.12
3	II-horizontal	49.59
4	IV	63.72
5	III-vertical	70.40
6	III-horizontal	82.54
7	VI	96.93

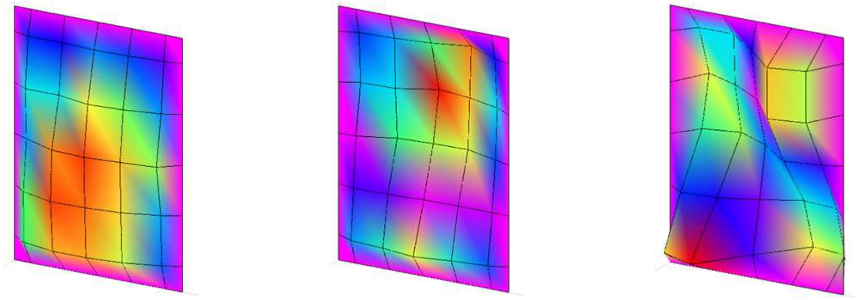

Mode 1 Mode 2 Mode 3

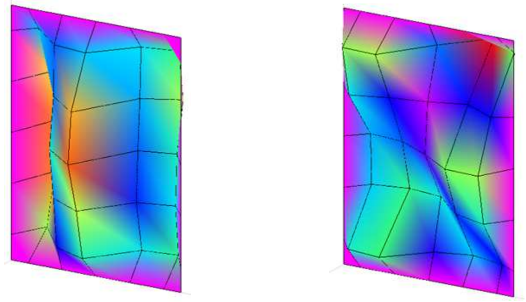

Mode 4 Mode 5

Figure 2.24 Experimental mode shapes for the wall W1-A with plaster.

Table 2.12 Experimental natural frequencies for the wall W1-A with plaster.

Mode	Mode name	Frequency [Hz]
1	I	90.43
2	II-horizontal	158.10
3	IV	262.10
4	III-vertical	326.77
5	VI	366.30

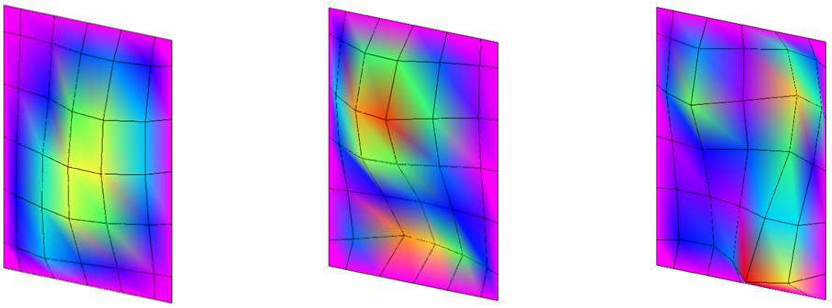

Mode 1 Mode 2 Mode 3

Figure 2.25 Experimental mode shapes for the wall W2-A with plaster.

Table 2.13 Experimental natural frequencies for the wall W2-A with plaster.

Mode	Mode name	Frequency [Hz]
1	I	64.31
2	II-horizontal	102.40
3	IV	161.50

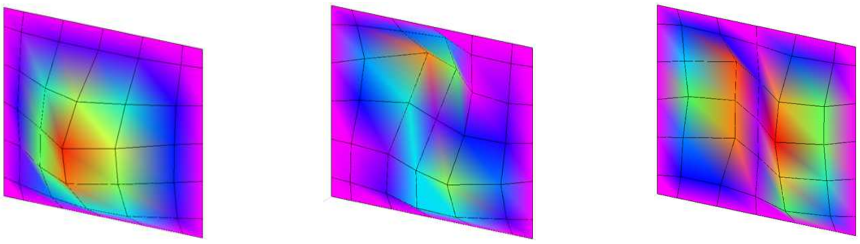

Mode 1

Mode 2

Mode 3

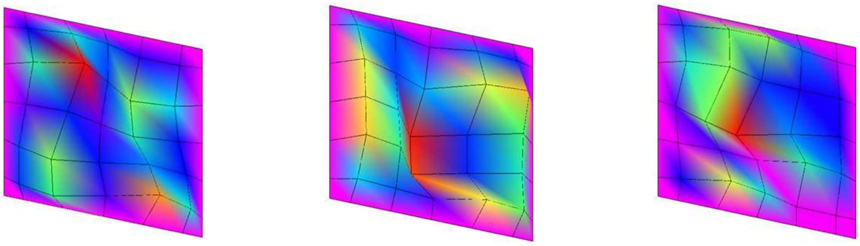

Mode 4

Mode 5

Mode 6

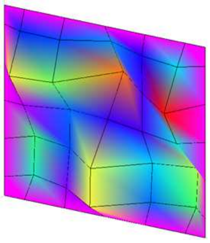

Mode 7

Figure 2.26 Experimental mode shapes for the wall W3-A with plaster.

Table 2.14 Experimental natural frequencies for the wall W3-A with plaster.

Mode	Mode name	Frequency [Hz]
1	I	34.24
2	II-horizontal	67.50
3	II-vertical	70.63
4	IV	99.28
5	III-vertical	116.50
6	III-horizontal	136.30
7	VI	152.40

In Table 2.15 and Table 2.16 the experimental natural frequencies obtained from the three tested walls of the Building 1 before and after the plaster realization are summarized. From the results of the impact tests it can be observed that the wall with thickness of 20 cm (W1-F) reaches the highest values of out of plane frequencies, then the panel with thickness of 12 cm (W3-F) and finally the wall with thickness of 8 cm (W1-F). Taking into account the walls after the realization of the plaster, leads to the same consideration, but in the latter case (wall with thickness of 8 cm) the frequency values are higher than before. In particular, the percentage of the frequency values obtained after the plaster realization increases in ranges between 25% and 63% considering all the tested walls (Table 2.17). The walls W1-F and W3-F, with similar length and height, evince the same modes order. Considering the wall W2-F, that has the same length and height of the wall W3-F, it can be observed that the mode called III-vertical has not been found in the case without plaster. After the plaster realization instead, there is the III-vertical mode, but it has a frequency value higher than the mode called II-horizontal. Therefore, only in the case with plaster, these two modes are reversed respect to the other two walls (W1-F and W3-F) that have the same modes order.

For what concerns Building 2, in Table 2.18 and Table 2.19 are summarized the experimental natural frequencies obtained from the three tested walls before and after the plaster realization. First, it can be observed that there is a difference in the modal behaviour of the wall W1-A and W2-A from the wall W3-A. In fact, the first two walls have similar modes order that is different from the third one, both with and without plaster, except for the first mode that is always the same for all of them. This may be due to the fact that the first two walls have very similar geometric dimensions, while the third one has the same height but a greater width (about 50% more). Considering the first out of plane frequency, the wall with thickness of 30 cm (W1-A) reaches its highest value; then the panel with the two layers of hollow clay bricks 12 cm thick with an insulating layer in the middle (W2-A) and finally the wall with thickness of 8 cm (W3-A). The same consideration can be done analysing the walls after the realization of the plaster. In this latter case the frequencies value are higher than before. In particular, after the plaster and insulation layers realization, the percentage of the frequency values obtained increases in a range between 8% and 74% for the two walls that have similar geometric dimensions (W1-A and W2-A). For the wall W3-A (Table 2.20), instead, the percentage varies from a minimum of 36% to a maximum of 76%. It is worth noting that for the wall W2-A the impact tests are performed only in one of the two faces and it should be probable that the insulation layer in the middle of the wall, is not able to transfer the excitation to the bricks layer in the opposite face. Therefore, it is presumable that the experimental results obtained should be inherent only to one of the two bricklayers (12 cm thick). The walls W1-A and W2-A have a similar dynamic behaviour; for the second panel the modes identified are in a less number than for the first wall, both with and without plaster. This difference can be due to the fact that the wall W2-A has three border constrained by the r.c. frame of the structure, while one vertical side is delimited by another internal infill built orthogonally. The wall W1-A has all four borders constrained by the r.c. members. Considering the wall W3-A, it can be noted that after the construction of both the plaster and the external insulation layer, there is an inversion of the second and third mode.

All the results obtained from the in situ impact tests carried out in the two buildings are analysed together in order to perform global comparison and evaluate the effects of the panel dimensions (height and length), hollow clay bricks thickness and border constraints, in the out of plane infill panels frequencies. Evaluating the hollow clay bricks thickness, it can be observed that greater thickness results in greater out of plane frequency values. The walls

W2-F and W3-A are both built with hollow clay bricks 8 cm thick and the modes order and frequency values are similar but not equal. Moreover, the two walls have a very similar height but different length; in particular the wall with the higher length (wall W2-F) presents the lower values of frequency, indicating a smaller bending stiffness compared to the other one. Anyway, the values of the first natural frequency, for both walls without plaster, are very close to each other. Dealing with the panel dimensions, the walls that have length greater than the height have a similar mode shapes order and the first vibrational modes have mainly vertical development. A similar consideration can be done for panels that have height larger than length, but in this case the first vibrational modes have mainly horizontal development.

Table 2.15 Experimental natural frequencies for the tested infill walls of Building 1 without plaster.

Mode name	Frequency [Hz]		
	W1-F	W2-F	W3-F
I	39.90	16.05	27.70
II-vertical	51.91	29.08	41.78
III-vertical	72.35	/	64.33
II-horizontal	111.53	39.38	75.89
IV	121.65	51.91	93.35
VI	139.90	74.37	113.40
V-vertical	140.60	119.20	136.70

Table 2.16 Experimental natural frequencies for the tested infill walls of Building 1 with plaster.

Mode name	Frequency [Hz]		
	W1-F	W2-F	W3-F
I	55.31	25.01	45.21
II-vertical	74.65	41.98	65.69
III-vertical	108.93	68.18	96.42
II-horizontal	139.90	57.52	116.90
IV	159.81	72.28	135.80
VI	189.15	99.27	165.23
V-vertical	201.78	157.09	193.40

Table 2.17 Changes in percentage of the natural frequency values for the tested infill walls of Building 1 after the plaster realization.

Mode name	Frequency percentage change [%]		
	W1-F	W2-F	W3-F
I	+39	+56	+63
II-vertical	+44	+44	+57
III-vertical	+51	/	+50
II-horizontal	+25	+46	+54
IV	+31	+39	+45
VI	+35	+33	+46
V-vertical	+44	+32	+41

Table 2.18 Experimental natural frequencies for the tested infill walls of Building 2 without plaster.

Mode name	Frequency [Hz]		Mode name	Frequency [Hz]
	W1-A	W2-A		W3-A
I	65.55	49.70	I	21.87
II-horizontal	91.03	71.40	II-vertical	40.12
III-horizontal	174.27	120.48	II-horizontal	49.59
IV	202.50	150.10	IV	63.72
II-vertical	231.00	/	III-vertical	70.40
VI	276.33	/	III-horizontal	82.54
			VI	96.93

Table 2.19 Experimental natural frequencies for the tested infill walls of Building 2 with plaster.

Mode name	Frequency [Hz]		Mode name	Frequency [Hz]
	W1-A	W2-A		W3-A
I	90.43	64.31	I	34.24
II-horizontal	158.10	102.40	II-vertical	70.63
IV	262.10	161.50	II-horizontal	67.50
III-vertical	326.77	/	IV	99.28
VI	366.30	/	III-vertical	116.50
			III-horizontal	136.30
			VI	152.40

Table 2.20 Changes in percentage of the natural frequency values for the tested infill walls of Building 2 after the plaster realization.

Mode name	Frequency percentage change [%]		Mode name	Frequency percentage change [%]
	W1-A	W2-A		W3-A
I	+38	+29	I	+57
II-horizontal	+74	+43	II-vertical	+76
IV	+29	+8	II-horizontal	+36
			IV	+56
			III-vertical	+65
			III-horizontal	+65
			VI	+57

Chapter 3.

Calibration of global f.e. models of the buildings

3.1. General

The calibration of global f.e. models of the buildings can be based on the comparison between experimental and numerical global modal parameters (natural frequencies and mode shapes). In fact, the smaller the differences between these parameters and the greater the reliability of the numerical models. The experimental modal parameters can be determined by means of operational modal analysis based on ambient vibration measurements at different construction stages, as described in the chapters before. As regard the numerical ones, they are obtained from global f.e. models developed and adjourned to account for the real conditions of the buildings during the dynamic tests and also to simulate their dynamic behaviour when subjected to very low energy ambient excitations. In particular, the updating procedures of manifold parameters allow to obtain calibrated global numerical f.e. models. First of all, the geometry and the details of the modelled structural elements have to be the same of those actually cast in place. Then, the mechanical construction material properties must to be determined in a way to simulate the real in situ materials. To estimate these material properties (especially for the concrete), ultrasonic in situ tests can be performed. These tests permit to estimate the elastic moduli of the concrete adopted to build the buildings and, through properly validated methods, it is possible to modify these properties over time. Other important updating parameters are the constraint and the boundary conditions, whose have to simulate the interaction between the considered structures with the surrounding others and with the ground (foundation systems). After that, the masses assigned in the numerical models have to be the same of those actually present on the buildings during the dynamic tests. It is very important to not considered all the design loads taken into account during the design process inasmuch they include variable loads that are rarely present on the structures, especially during the construction. Finally, the non-structural elements can be considered and modelled within the global finite element models, among them the most important are the infills. The presence of these non-structural components, both in terms of mass and stiffness, can be significantly vary the dynamic behaviour of the buildings therefore it becomes crucial to model correctly these elements. The mass of the infill masonry walls can be accurately calculated once the construction materials and the geometry of the panels are known, while the determination of their stiffness turn out to be more complicated. A procedure to estimate the stiffness of the masonry infills through the comparison between experimental and numerical modal parameters of the panels is proposed and depicted hereinafter.

3.2. Description of global f.e. models of the bare buildings

To identify the dynamic properties of the investigated buildings and to calibrate predictive models able to evaluate the infills contribution, global f.e. models are developed for both the buildings by means of the code SAP2000.

The first f.e. model developed for Building 1, called Mod1-A, represents the edifice in a key stage of the construction process, i.e. at the end of construction of the bare structure (August 25, 2016) (Figure 3.1a). At this point, only the infills at the underground level were already realized. Beams and columns are modelled with elastic frame elements while floor and stair slabs with shell elements. To consider the real size of the joints between the elements of the r.c. frames, rigid links are modelled at the end sections of frame elements. The ends of the columns at the underground floor are fixed. The infills at the underground level are modelled as shell elements. The masses of modelled elements are automatically considered by the software according to their geometry and their mechanical properties, except for the floor slabs that are modelled only in terms of stiffness. In fact, the masses of the floors are calculated and then assigned to the beams, with a higher portion to the beams arranged orthogonally to the floor frame (distribution 60% - 40% for the beams at the ground and first floors and 80% - 20% for the beams at the attic and roof floors). The other masses actually present on the structure during the dynamic tests are taken into account and assigned to the beams, considering as far as possible their real positions.

For Building 2 the first f.e. model generated, called Mod2-A, represents the building at the end of the construction of the bare structure (June 1, 2016) (Figure 3.1b). As reported before for the other building, the structural elements such as beams and columns are modelled with elastic frame elements while plates (for floor and perimetrical slabs) with shell elements. Also the external stairs and the retaining walls that surround the entire building at the underground floor are modelled with shell elements, as well as the shear wall with variable height at the attic floor that divide the two housing units. To consider the real size of the joints between the elements of the r.c. frames, rigid links are modelled at the end sections of frame elements; furthermore, because of the eccentricity in elevation between the beams of the attic floor, the beams of the roof and the shell used to model the attic floor slab, rigid elements are used to connect the frame and the shell elements. The ends of the columns and retaining walls at the underground floor are fixed. The ground that surround the building at the underground level is modelled using elastic springs linked with the retaining walls. The stiffness of these springs is calculated on the basis of the ground typology and on the results of the geological survey carried out before the beginning of the work. As before, the masses of the modelled elements are taken into account by the software according to their geometry and specific weight, while the masses of the floor slabs are calculated and assigned to the beams. The other masses actually present on the building during the dynamic tests are considered and assigned to the beams. Also the mass of the ground is considered and modelled within the f.e. model.

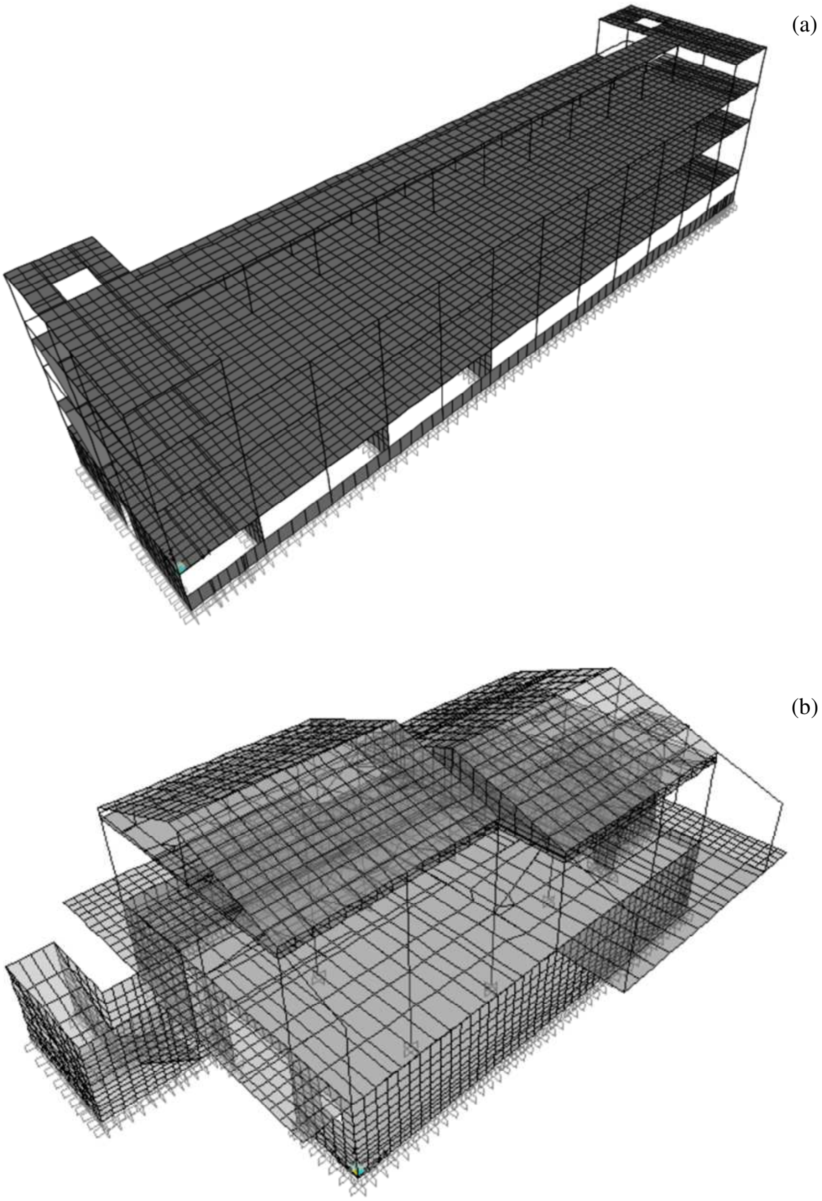

Figure 3.1 Developed f.e. models at the end of the construction of the bare structures: (a) Mod1-A, (b) Mod2-A.

3.3. Determination of the elastic modulus of concrete

The elastic modulus of concrete is a parameter that notably influences the results of numerical models developed with f.e. software. It is a common practice to consider only one elastic modulus for all the r.c. elements, but this assumption may not be representative of reality. In fact, the construction of an edifice is performed step by step, building the structure from bottom to top in different stages, called casting phases. Usually, in each of them a floor or a group of columns belonging to the same elevations, are poured. For this reasons, the concrete used is not always the same and, besides, it has different aging levels.

To reduce the number of uncertainties in the modelling procedure, the mechanical properties of the concrete adopted to build the frame structures of the two buildings case studies are estimated by means of ultrasonic in situ tests. These tests were performed after the construction of the entire bare structures and in several elements of both edifices. As concerns Building 1, seven of the nine casting phases required to build the entire structure were investigated and, in detail, twenty-two columns and seven beams were tested. For Building 2, four of the seven casting phases were examined, for a total of eleven columns, two beams and three retaining walls tested.

The ultrasonic test consists of a pulse of longitudinal vibration produced by an electro-acoustical transducer held in contact with a surface of the concrete under test. After crossing a known path length in the concrete, the pulse of vibrations is converted into an electrical signal by a second transducer and electronic timing circuits enable the transit time of the pulse to be measured. The apparatus used in the test consists of an electrical pulse generator, a pair of transducers, an amplifier and an electronic timing device for measuring the time interval elapsing between the onset of a pulse generated at the transmitting transducer and the onset of its arrival at the receiving transducer. A calibration bar is also supplied to provide a datum for the velocity measurement. In order to obtain a measurement of pulse velocity which is reproducible, it is necessary to take into account various factors which can influence the measurements (moisture content, temperature, path length, shape and size of specimen, reinforcing bars, cracks and voids, etc.). Although the direction in which the maximum energy is propagated is at right angles to the face of the transmitting transducer, it is possible to detect pulses which have travelled through the concrete in some other direction. It is therefore possible to make measurements of pulse velocity by placing the two transducers on opposite faces (direct transmission), or on adjacent faces (semi-direct transmission), or the same face (indirect transmission) of a concrete structure or specimen. For direct transmission, the path length is the shortest distance between the transducers. For semi-direct transmission, it is generally found to be sufficiently accurate to take the path length as the distance measured from centre to centre of the transducer faces. With indirect transmission, the path length is not measured, but a series of measurements is made with transducers at different distances apart. There shall be adequate acoustical coupling between the concrete and the face of each transducer. For many concrete surfaces, the finish is sufficiently smooth to ensure good acoustical contact by the use of a coupling medium such as petroleum jelly, grease, soft soap and kaolin/glycerol paste and by pressing the transducer against the concrete surface. Repeated readings of the transit time should be made until a minimum value is obtained, indicating that the thickness of the coupling material has been reduced to a minimum. When the concrete surface is very rough and uneven, the area of the surface should be smoothed and levelled by grinding or by the use of a quick-setting epoxy resin. For direct and semi-direct transmissions, the pulse velocity shall be calculated from the formula

$$V = \frac{L}{T} \tag{19}$$

where L is the path length and T is the time taken by the pulse to transverse the length. Once the transmission velocity V is known, the dynamic elastic modulus of concrete can be calculated on the basis of the theory of the wave propagation in homogeneous, isotropic and elastic materials as

$$E_d = \rho V^2 \frac{(1+\upsilon_d)(1-2\upsilon_d)}{1-\upsilon_d} \tag{20}$$

where v_d is the dynamic Poisson coefficient (0.15 for high concrete resistance and 0.30 for low concrete resistance) and ρ is the density of the concrete. We refer to the dynamic elastic modulus of concrete inasmuch it is estimated by means of the results of non-destructive dynamic tests. It is also known that the values of dynamic elastic moduli are different (higher) from that obtained by direct static testing of cylinders drawn from the structure (Popovics et al., 2008). The elastic modulus of concrete is a material property that changes with time. At an age different from 28 days the modulus of elasticity of concrete may be estimated by

$$E_{ci}(t) = \beta_E(t) E_{ci} \tag{21}$$

with

$$\beta_E(t) = [\beta_{cc}(t)]^{0.5} \tag{22}$$

where $E_{ci}(t)$ is the modulus of elasticity at an age t and E_{ci} is the modulus of elasticity at an age of 28 days. The coefficient $\beta_E(t)$ depends on the age of concrete by means of the coefficient $\beta_{cc}(t)$

$$\beta_{cc}(t) = \exp\left\{ s\left[1-\left(\frac{28}{t}\right)^{0.5}\right]\right\} \tag{23}$$

The coefficient s, to be inserted in $\beta_{cc}(t)$ depends on the type of cement (strength class) and on the compressive strength of the concrete and may be taken from Table 3.1.

In Table 3.2 and Table 3.3 the elastic moduli of concrete for the different casting phases of the two buildings are listed. These moduli are calculated with Eq. (20) on the basis of the results (in terms of transmission velocities) of the ultrasonic in situ tests. These tests are performed in specific days, so the properties of concrete refer to that dates. To estimate the effective dynamic properties of concrete corresponding to the specific dates when the ambient vibration measurements were performed, Eq. (21) is used. In particular, for Building

1 the elastic moduli are calculated for the day August 25, 2016 and November 7, 2016, while for Building 2 June 1, 2016 and July 21,2016.

Table 3.1 Coefficient *s* to be used for different types of cement.

f_{cm} [MPa]	Strength class of cement	*s*
≤ 60	32.5 N	0.38
	32.5 R, 42.5 N	0.25
	42.5 R, 52.5 N, 52.5 R	0.20
> 60	All classes	0.20

Table 3.2 Elastic moduli of concrete for Building 1.

Casting phase	Elements	E [MPa]	
		August 25, 2016	November 7, 2016
1	1st elevation	33915.14	34859.68
2	2nd elevation	31601.20	32939.35
3	First floor	33214.96	35234.11
4	3rd elevation	32149.65	34475.84
5	Attic floor	31659.46	35254.49
6	4th elevation	30342.09	34847.61
7	Roof floor	18828.19	34156.21

Table 3.3 Elastic moduli of concrete for Building 2.

Casting phase	Elements	E [MPa]	
		June 1, 2016	July 21, 2016
1	1st elevation (walls)	27369.96	27641.16
2	1st elevation (columns)	33529.02	33958.71
3	2nd elevation	27424.63	28460.96
4	Attic floor	30311.32	31399.49

3.4. Modelling of the infills within the global f.e. models

3.4.1. Numerical models of the in situ tested walls

F.e. models of the investigated infill masonry walls are developed by means of the SAP2000 code. Each infill wall is modelled with shell elements having the same geometric dimensions of the real walls (length, height and thickness) (Figure 3.2). A shell element is defined as a two-dimensional element with a combination of membrane and plate behaviour, hence supports forces and moments. The edges of the shells are fixed. Some tests are performed to investigate the constraint between the masonry infills and the r.c. frame of the structure. In particular, two different models are developed: the first one considering only the infill wall, the second modelling also the r.c. frame around the infill, by means of shell elements in continuity with those of the masonry infill. The differences between these two models, in terms of modal parameters, are negligible. Accordingly, for the successive analyses only the first model is considered. The shell elements (or each sub-shell element of a meshed area) has its own element local coordinate system used to define material properties, loads and output. The axis of this local system are denoted as 1, 2 and 3. The first two axes lie in the plane of the element while the third axis is normal. The masses of the walls are automatically accounted by the software, according to their geometry and considering the specific weight. In order to obtain both the natural frequencies and the relevant mode shapes, modal analyses with eigen-vectors are performed.

Assuming that both the geometric features (length, height and thickness) and the masses are known, the masonry mechanical properties, i.e., the elastic modulus *E*, the shear modulus *G* and the Poisson's coefficient ν, are investigated and updated. For this purpose, several model strategies are taken into account, with the aim at fitting numerically the experimental out of plane dynamic behaviour obtained by the in situ tests described in the previous chapters.

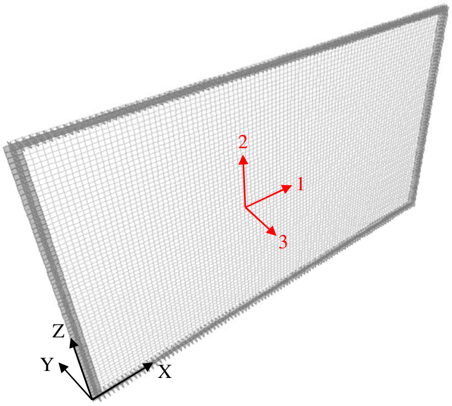

Figure 3.2 Example of the numerical shell model developed.

In particular, for each tested infill wall, the updating procedure is performed both in the case without and with the plaster. It is worth noting that one approximation of this methodology is to consider the masonry as a homogenous material. In fact, it is known that masonry is a heterogeneous material composed by bricks held together with mortar joints and, often, coated with plaster; so its mechanical properties depend on the mechanical properties of the several construction materials adopted. Therefore, the abovementioned mechanical properties have to be considered as mean values that characterize the infill panels in their entirely.

3.4.2. Determination of the elastic modulus E of the masonry

The estimation of the elastic modulus *E* of the masonry is performed through a three steps procedure, involving different theoretical formulations regarding the theory of the plate. In detail the Kirchooff theory, the Mindlin/Reissner formulations and the Huber one.

In the beginning, the shell elements representing the infill masonry walls are considered thin shell elements, i.e., their plate bending behaviour is governed by the Kirchhoff's theory, neglecting therefore transverse shear deformation; the masonry material is considered isotropic. The Kirchhoff's formulation is governed by a differential equation for the deflection that depends on the thickness of the plate *h* and on two mechanical properties of the material by means of the constant *D*, as shown in the following equation, the elastic modulus *E* and the Poisson's coefficient ν

$$D = \frac{Eh^3}{12\left(1-\nu^2\right)} \tag{24}$$

The Poisson's coefficient ν is assumed to be constant and equal to 0.2 as its variation does not affect significantly the out of plane dynamic behaviour of the shell, while the only unknown parameter of the material mechanical properties is the elastic modulus *E.* The calibration of the Young modulus is achieved with the updating procedure, which ends when the first numerical out of plane mode matches well the experimental one, in terms of both frequency and mode shape. In Table 3.4 and Table 3.5 the elastic moduli *E* obtained at the end of the updating procedure, are listed, for both Building 1 and Building 2.

Successively, the shell elements are considered thick elements, i.e., their plate bending behaviour is governed by the Mindlin/Reissner formulations, whom includes the effects of transverse shear deformation. Also in this case the masonry material is considered isotropic. These formulations are governed by a sixth-order system of differential equations for the plate bending theory that depends on the thickness of the plate *h* and on all the mechanical properties of the material (elastic modulus *E*, shear modulus *G* and Poisson's coefficient ν) by means of the constants *D*, previously defined, and the constant k^2, defined in the following

$$k^2 = \frac{2C}{D\left(1-\nu\right)} \qquad \text{where} \qquad C = Gh \tag{25}$$

The Poisson's coefficient ν is assumed constant and equal to 0.2 and the shear modulus *G* is calculated with the formulation of the elasticity theory

$$G = \frac{E}{2(1+\upsilon)} \tag{26}$$

Hence, the parameter calibrated during the updating procedure is only the elastic modulus *E*. Also in this case, this procedure ends when the first numerical out of plane mode well matches the experimental one, in terms of both frequency and mode shape. In Table 3.6 and Table 3.7 the elastic moduli *E* obtained at the end of the updating procedure, are listed, for both Building 1 and Building 2.

Finally, the shell elements are considered again thin element, but composed of orthotropic material. In this case the theoretical approach is governed by the Huber differential equation that depends on the thickness of the plate *h*, the elastic moduli in the two main orthogonal local directions of the plane E_1 and E_2, respectively, the shear modulus *G* and the Poisson's coefficients ν_1 and ν_2 in the same local directions. In detail, it is necessary to know only one of the two Poisson's coefficients, inasmuch the second one can be obtained from the following relation

$$\frac{\nu_x}{E_x} = \frac{\nu_y}{E_y} \tag{27}$$

In this case, a first approximation consists in not considering both the Poisson's coefficients as updating parameters, thanks to the fact that their variation does not affect significantly the out of plane dynamic behaviour of the shell. Another assumption is to estimate the shear modulus *G* with the following equation

$$G \approx \frac{\sqrt{E_x E_y}}{2\left(1+\sqrt{\nu_x \nu_y}\right)} \tag{28}$$

This way the parameters taken into account in the updating procedure are only the elastic moduli E_1 and E_2; the process ends when the numerical out of plane modes match well the experimental ones, in terms of both frequency and mode shape. In Table 3.8 and Table 3.9 the elastic moduli *E* obtained at the end of the updating procedure, are listed, for both the buildings.

Table 3.4 Values of elastic moduli *E* for the tested infill masonry walls of Building 1: isotropic thin shell.

Wall typology	E [MPa]	
	Without plaster	With plaster
W1-F	2200	3600
W2-F	1300	3100
W3-F	2200	4200

Table 3.5 Values of elastic moduli *E* for the tested infill masonry walls of Building 2: isotropic thin shell.

Wall typology	E [MPa]	
	Without plaster	With plaster
W1-A	400	700
W2-A	2200	3100
W3-A	1700	2800

Table 3.6 Values of elastic moduli *E* for the tested infill masonry walls of Building 1: isotropic thick shell.

Wall typology	E [MPa]	
	Without plaster	With plaster
W1-F	2300	3800
W2-F	1300	3100
W3-F	2300	4300

Table 3.7 Values of elastic moduli *E* for the tested infill masonry walls of Building 2: isotropic thick shell.

Wall typology	E [MPa]	
	Without plaster	With plaster
W1-A	550	950
W2-A	2300	3200
W3-A	1700	2900

Table 3.8 Values of the elastic moduli E_1 and E_2 for the tested infill masonry walls of Building 1: orthotropic thin shell.

Wall typology	E_1 [MPa]		E_2 [MPa]	
	Without plaster	With plaster	Without plaster	With plaster
W1-F	1000	2000	2900	4100
W2-F	3100	5100	900	2400
W3-F	2400	3700	2700	4500

Table 3.9 Values of the elastic moduli E_1 and E_2 for the tested infill masonry walls of Building 2: orthotropic thin shell.

Wall typology	E_1 [MPa]		E_2 [MPa]	
	Without plaster	With plaster	Without plaster	With plaster
W1-A	450	500	400	1300
W2-A	2400	3400	900	1900
W3-A	1600	3100	1700	2600

Taking into account the infills of the Building 1, modelled as isotropic thin shell elements in the case before the plaster, it is observable that the elastic modulus *E* estimated is the same for the panels of thickness 20 cm and 12 cm (W1-F and W3-F, respectively). The estimation, instead, is characterized by a lower value for the wall of thickness 8 cm (W2-F). After the plaster, the panel 12 cm thick (W3-F) shows the highest value of the estimated *E*, then the wall with thickness of 20 cm (W1-F) and finally the one with thickness of 8 cm (W2-F). For Building 2, before and after the plaster, the highest value of the elastic modulus *E* is obtained for the wall composed by two layers 12 cm thick (W2-A), then the second one is achieved for the wall 8 cm thick (W3-A) and the lower value is obtained for the wall 30 cm thick (W1-A). It is worth noting that for the wall W2-A, the numerical model is developed considering only one of the two leaf panels and neglecting the insulation layer. Furthermore, the low values of *E* obtained for the wall 30 cm thick are in disagree with the fact that the elastic modulus is directly proportional to the thickness of the wall, as can be seen for all other cases without plaster. This could be due to the fact that the out of plane bending stiffness of the wall should be influenced, and in particular reduced, by the notable width of the bed joints and the particular dimensions of the bricks (wider than high). It follows that in this case the mechanical properties estimated for the out of plane dynamic behaviour of the panel, can be different from those that characterize the in plane dynamic behaviour. Making a comparison between the results for both the buildings, it can be observed that the walls with the same hollow clay brick thickness (W2-F with W3-A and W3-F with W2-A) have very similar elastic modulus values, in the case without plaster, and quite similar in the case with plaster. Obviously, in the latter case, the mechanical properties of the panel depend also by the typology of the plaster and its thickness.

The introduction of the shear deformability on the numerical models leads to slightly higher values of elastic moduli *E* for all the tested walls, therefore the shear deformability can be neglected without significantly effect on the reliability of the results.

In the case of modelling the walls as orthotropic elements, it can be observed that, for Building 1, the infill 20 cm thick (W1-F) has a higher value of elastic modulus in the vertical direction with respect to the horizontal one. The infill 8 cm thick (W2-F) has a higher value of *E* in the horizontal direction, with respect to the vertical one and the infill 12 cm thick (W3-F) has a higher value of the estimated modulus in the vertical direction and lower one in the horizontal way. The same result occurs after the plaster, but in this case the values of elastic moduli in both the orthogonal directions are greater than the case without plaster, for all the infills. For Building 2, the infill 30 cm thick (W1-A) has a higher value of *E* in the vertical direction with respect to the horizontal one. However, the values of the elastic moduli are quite low so it is reasonable to think that, like before for the isotropic solutions, the mechanical properties estimated for the out of plane dynamic behaviour of the panel can be different from those that characterize the in plane dynamic behaviour. The infill with double leaf panels 12 cm thick (W2-A) has a higher value of elastic modulus in the horizontal direction with respect to the vertical one and the infill 8 cm thick (W3-A) has a higher value of the estimated modulus in the vertical direction and lower one in the horizontal way for the case without plaster and vice versa after the plaster realization. Moreover, after the plaster, the values of elastic moduli in both the orthogonal directions are greater than the case without plaster, for all the infills.

3.4.3. Evaluation of the reliability of the results

The natural frequencies for all modes of each infill masonry wall investigated, for both the two buildings case studies, are listed from Table 3.10 to Table 3.21. In particular, for each wall both the natural frequencies obtained experimentally from the dynamic in situ tests and the corresponding numerical ones, are reported. The latter ones are achieved by means of the elastic moduli *E* previously determined for the three different modelling strategies.

Considering both the Building 1 and the Building 2, it can be noted that the numerical natural frequency values obtained modelling the walls as thin isotropic shell elements are quite close to the experimental ones. In particular, there is a very good agreement between the first experimental and numerical natural frequencies. The same considerations can be done when the infill walls are modelled as thick isotropic shells. However, the best results in terms of total differences between experimental and numerical natural frequencies are achieved modelling the infill panels as orthotropic thin elements.

Table 3.10 Natural frequencies of the wall W1-F without plaster of Building 1.

Mode	Mode name	Frequencies [Hz]			
		Experimental	Numerical		
			Shell thin isotropic	Shell thick isotropic	Shell thin orthotropic
1	I	39.90	39.79	39.73	41.51
2	II-vertical	51.91	59.35	58.99	52.71
3	III-vertical	72.35	92.74	91.14	73.08
4	II-horizontal	111.53	98.81	96.28	108.69
5	IV	121.65	117.09	113.85	119.48
6	VI	139.90	148.35	143.08	138.27
7	V-vertical	140.60	198.02	187.85	140.86

Table 3.11 Natural frequencies of the wall W2-F without plaster of Building 1.

Mode	Mode name	Frequencies [Hz]			
		Experimental	Numerical		
			Shell thin isotropic	Shell thick isotropic	Shell thin orthotropic
1	I	16.05	16.25	16.17	16.97
2	II-vertical	29.08	23.64	23.51	30.68
3	II-horizontal	39.38	40.73	40.31	38.12
4	IV	51.91	47.67	47.17	51.05
5	VI	74.37	59.57	58.86	72.26
6	V-vertical	119.20	76.73	75.60	119.45

Table 3.12 Natural frequencies of the wall W3-F without plaster of Building 1.

Mode	Mode name	Frequencies [Hz]			
			Numerical		
		Experimental	Shell thin isotropic	Shell thick isotropic	Shell thin orthotropic
1	I	27.70	27.44	27.77	30.00
2	II-vertical	41.78	39.94	40.33	42.82
3	III-vertical	64.33	61.45	61.76	65.05
4	II-horizontal	75.89	68.79	68.79	75.74
5	IV	93.35	80.53	80.47	87.80
6	VI	113.40	100.64	100.24	108.53
7	V-vertical	136.70	129.61	128.31	135.90

Table 3.13 Natural frequencies of the wall W1-F with plaster of Building 1.

Mode	Mode name	Frequencies [Hz]			
			Numerical		
		Experimental	Shell thin isotropic	Shell thick isotropic	Shell thin orthotropic
1	I	55.31	55.60	55.24	55.22
2	II-vertical	74.65	82.93	81.85	73.49
3	III-vertical	108.93	129.60	125.91	106.12
4	II-horizontal	139.90	138.08	132.63	142.65
5	IV	159.81	163.62	156.66	160.02
6	VI	189.15	207.30	196.23	190.15
7	V-vertical	201.78	276.71	256.12	212.57

Table 3.14 Natural frequencies of the wall W2-F with plaster of Building 1.

Mode	Mode name	Frequencies [Hz]			
			Numerical		
		Experimental	Shell thin isotropic	Shell thick isotropic	Shell thin orthotropic
1	I	25.01	25.18	25.00	24.88
2	II-vertical	41.98	36.65	36.33	41.31
3	II-horizontal	57.52	63.13	62.15	58.83
4	III-vertical	68.18	56.39	55.71	68.27
5	IV	72.28	73.90	72.71	74.22
6	VI	99.27	92.35	90.66	99.96
7	V-vertical	157.09	118.94	116.26	151.53

Table 3.15 Natural frequencies of the wall W3-F with plaster of Building 1.

Mode	Mode name	Frequencies [Hz]			
		Experimental	Numerical		
			Shell thin isotropic	Shell thick isotropic	Shell thin orthotropic
1	I	45.21	45.27	44.97	45.86
2	II-vertical	65.69	65.89	65.24	64.64
3	III-vertical	96.42	101.37	99.56	97.37
4	II-horizontal	116.90	113.49	110.52	116.29
5	IV	135.80	132.85	129.22	133.99
6	VI	165.23	166.01	160.57	164.46
7	V-vertical	193.40	213.82	204.59	202.05

Table 3.16 Natural frequencies of the wall W1-A without plaster of Building 2.

Mode	Mode name	Frequencies [Hz]			
		Experimental	Numerical		
			Shell thin isotropic	Shell thick isotropic	Shell thin orthotropic
1	I	65.55	64.23	66.53	67.49
2	II-horizontal	91.03	100.31	101.10	103.35
3	III-horizontal	174.27	161.02	153.10	163.95
4	IV	202.50	189.84	174.96	199.20
5	II-vertical	231.00	156.49	146.92	165.78
6	VI	276.33	246.68	218.43	256.07

Table 3.17 Natural frequencies of the wall W2-A without plaster of Building 2.

Mode	Mode name	Frequencies [Hz]			
		Experimental	Numerical		
			Shell thin isotropic	Shell thick isotropic	Shell thin orthotropic
1	I	49.70	50.03	50.42	47.01
2	II-horizontal	71.40	92.63	92.44	74.66
3	III-horizontal	120.48	158.80	156.19	118.18
4	IV	150.10	163.66	161.35	155.74

Table 3.18 Natural frequencies of the wall W3-A without plaster of Building 2.

Mode	Mode name	Frequencies [Hz]			
		Experimental	Numerical		
			Shell thin isotropic	Shell thick isotropic	Shell thin orthotropic
1	I	21.87	22.11	21.99	21.80
2	II-vertical	40.12	41.52	41.16	40.51
3	II-horizontal	49.59	48.42	47.93	48.12
4	IV	63.72	66.30	65.49	65.30
5	III-vertical	70.40	72.49	71.51	70.47
6	III-horizontal	82.54	88.96	87.46	88.62
7	VI	96.93	95.97	94.41	93.93

Table 3.19 Natural frequencies of the wall W1-A with plaster of Building 2.

Mode	Mode name	Frequencies [Hz]			
		Experimental	Numerical		
			Shell thin isotropic	Shell thick isotropic	Shell thin orthotropic
1	I	90.43	90.74	90.57	86.44
2	II-horizontal	158.10	141.69	136.88	159.63
3	IV	262.10	268.17	233.13	256.82
4	III-vertical	326.77	418.31	320.41	355.75
5	VI	366.30	348.46	289.25	367.75

Table 3.20 Natural frequencies of the wall W2-A with plaster of Building 2.

Mode	Mode name	Frequencies [Hz]			
		Experimental	Numerical		
			Shell thin isotropic	Shell thick isotropic	Shell thin orthotropic
1	I	64.31	64.07	63.85	62.86
2	II-horizontal	102.40	118.62	116.68	104.32
3	IV	161.50	209.58	202.81	207.79

Table 3.21 Natural frequencies of the wall W3-A with plaster of Building 2.

Mode	Mode name	Frequencies [Hz]			
		Experimental	Numerical		
			Shell thin isotropic	Shell thick isotropic	Shell thin orthotropic
1	I	34.24	34.17	34.37	34.40
2	II-horizontal	67.50	74.85	74.52	73.56
3	II-vertical	70.63	64.18	64.12	66.53
4	IV	99.28	102.49	101.59	103.41
5	III-vertical	116.50	112.06	110.71	117.32
6	III-horizontal	136.30	137.52	134.88	134.12
7	VI	152.40	148.37	145.71	152.43

3.4.4. Upgrading of the global f.e. models of the buildings

The global f.e. models of the edifices previously described are adjourned to consider another key stage of the construction process, i.e. after the construction of the infill masonry walls. In detail, for Building 1, this further model refers to the state of work progress at the date of November 7, 2016 and it is called Mod1-B (Figure 3.3a), while for Building 2 at the date of July 21, 2016 and it is called Mod2-B (Figure 3.3b). The external and internal infill masonry walls are modelled as thin isotropic shell elements with their real dimensions and thickness and considering their effective positions and openings, if present. The masses of these walls are taken into account automatically by the software on the basis of their geometric dimensions and specific weight. The mechanical properties of the wall masonries are taken in accordance with the results of the numerical analyses performed before on the infill masonry panels and considering the walls as thin isotropic shell elements.

As concern Building 1, six infill masonry walls typologies are adopted to build all the infills: three to realize the external infills (EWF-0, EW-F1 and EWF-2) and three for the internal ones (IWF-0, IWF-1 and IWF-2). The three internal typologies were tested and investigated hence it was possible to obtain their mechanical properties. For the external infills, the material properties to use in the modelling are estimated on the basis of the results of the internal ones. In fact, the EWF-2 typology is built with hollow clay bricks with the same thickness of the IWF-2 typology, so their properties are assumed to be the same. The EWF-0 and EWF-1 typologies are realized with coupled leaf panels with the same thicknesses of some of the internal walls, so the properties of these composite walls are estimated on the basis of the material properties of each leaf. In the f.e. model that refers to the date of November 7, 2016, also the steel structures of the two inclined covering flaps are modelled.

Regarding Building 2, only three infill masonry wall typologies are used to build all the infills. All these typologies are tested and investigated, so the material properties are known. As concern the EWA-0 typology adopted for all the external infills, it is evident that the material properties determined before considering the out of plane behaviour of the panel cannot be used to represent their in plane behaviour. Consequently, only for this typology, the mechanical material properties are estimated on the basis of ambient vibration measurements results, with the aim to fit the numerical modal parameters with the experimental ones, in terms of natural frequency and mode shapes of the entire building. The elastic modulus determined with this procedure is equal to 3300 MPa for the case without plaster. Moreover, the acoustical and thermal insulation layer 12 cm thick placed over the ground floor is considered and modelled within the global f.e. model as a thin layer positioned at the base of all the infills. In fact, all of them are built over this layer.

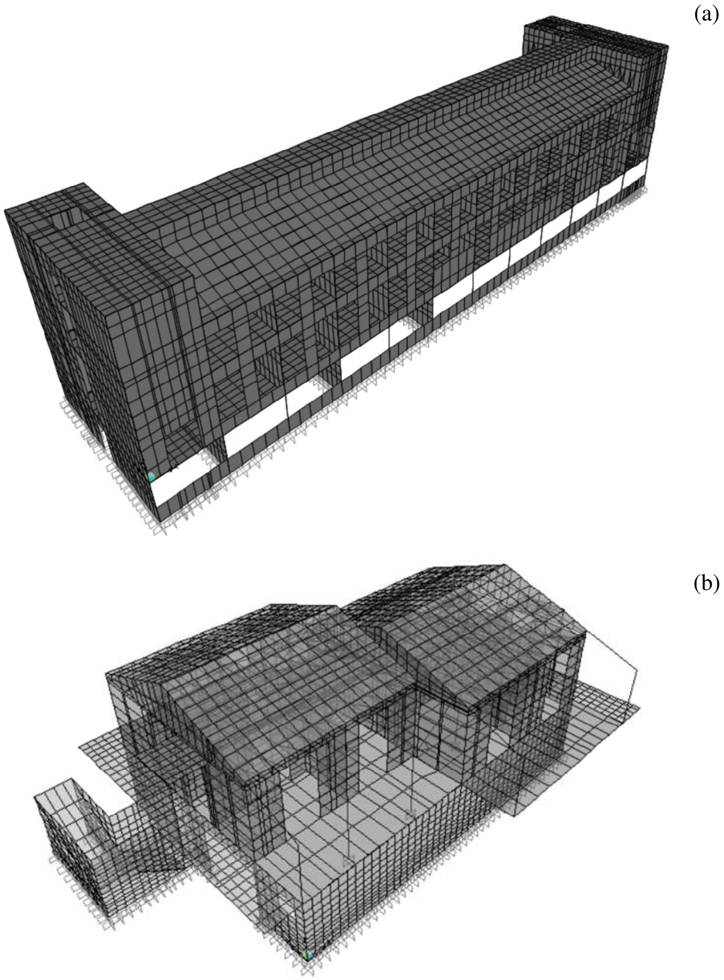

Figure 3.3 Developed f.e. models with the infill masonry walls: (a) Mod1-B, (b) Mod2-B.

3.5. Numerical results and comparison with the experimental ones

The numerical modal parameters of the two buildings are determined considering the cases before and after the construction of the infill masonry walls. Table 3.22 and Table 3.23 report the numerical natural frequencies for the first three vibrational modes of the bare building structures (August 25, 2016 for the Building 1 and June 1, 2016 for the Building 2) and after the construction of the infills (November 7, 2016 for the Building 1 and July 21, 2016 for the Building 2); Figure 3.4 and Figure 3.5 show the relevant mode shapes for the Building 1 and 2, respectively.

In Table 3.24 and Table 3.25 comparison between the experimental and numerical natural frequencies relevant to both the buildings and obtained from the two different key stages of the construction processes are listed. For both buildings case studies, the numerical frequencies reached before and after the infills construction show a very good agreement with the corresponding experimental ones, especially for the first two vibration modes, while for the third one the numerical frequencies obtained are slightly lower than the experimental ones. In order to compare the mode shapes identified experimentally with those obtained numerically, for both buildings case studies, the modal assurance criterion (MAC) index is calculated. This index indicates how well the analytical mode shapes fit the experimental ones; the closer the value approaches to one, the more similar are the mode shapes. Figure 3.6 and Figure 3.7 portray the MAC values between the experimental and numerical mode shapes for Building 1 and Building 2 in both construction stages considered (before and after the infills). The corresponding modes (diagonal entries) have high MAC values, indicating a very good agreement between experimental and numerical mode shapes for all cases.

Table 3.22 Numerical natural frequencies for Building 1.

Mode	Mode name	Frequency [Hz]	
		August 25, 2016	November 7, 2016
1	1st N-S	2.47	5.20
2	1st E-W	3.32	5.71
3	1st Rot	3.87	6.14

Table 3.23 Numerical natural frequencies for Building 2.

Mode	Mode name	Frequency [Hz]	
		June 1, 2016	July 21, 2016
1	1st N-S	5.77	10.80
2	1st E-W	6.25	12.81
3	1st Rot	7.69	15.12

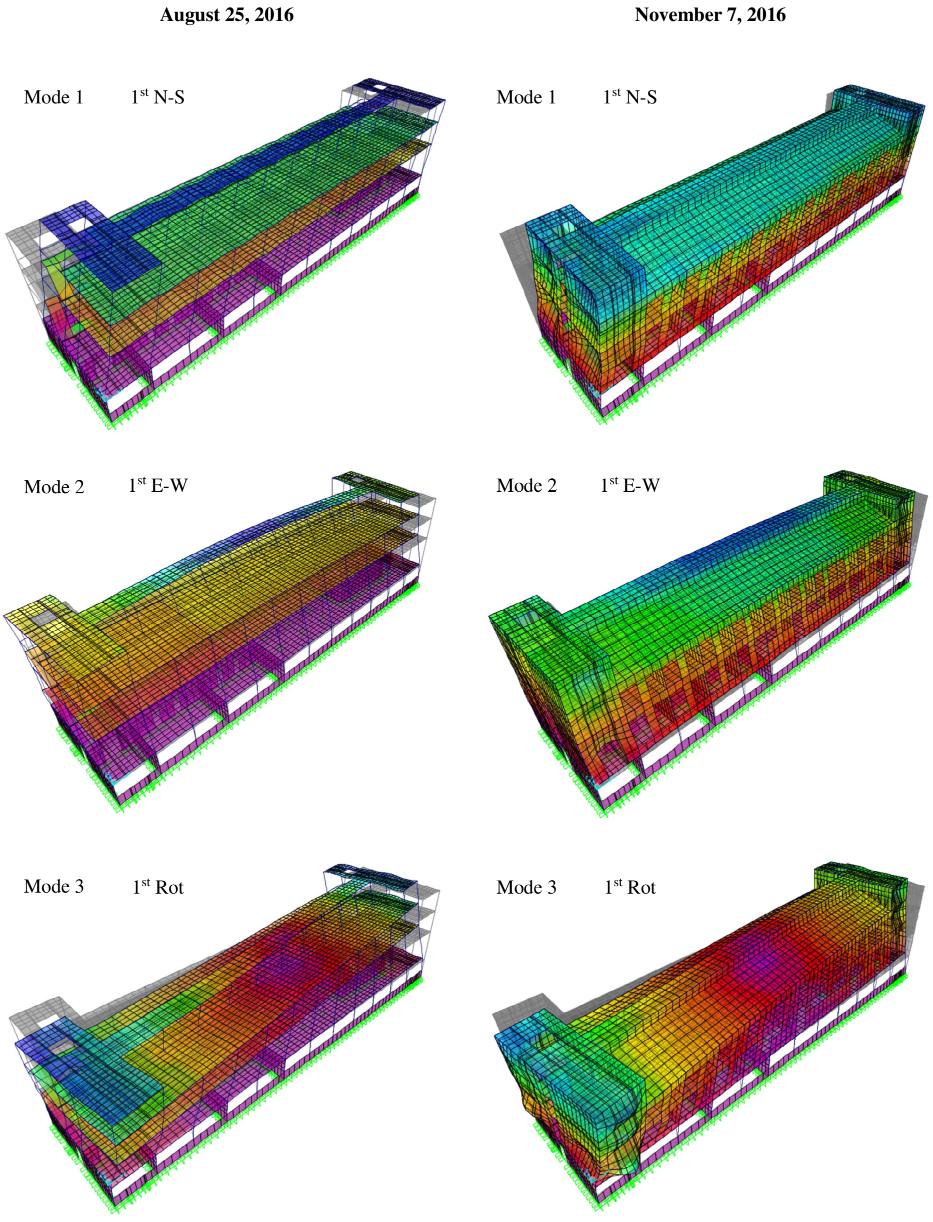

Figure 3.4 Numerical mode shapes for Building 1.

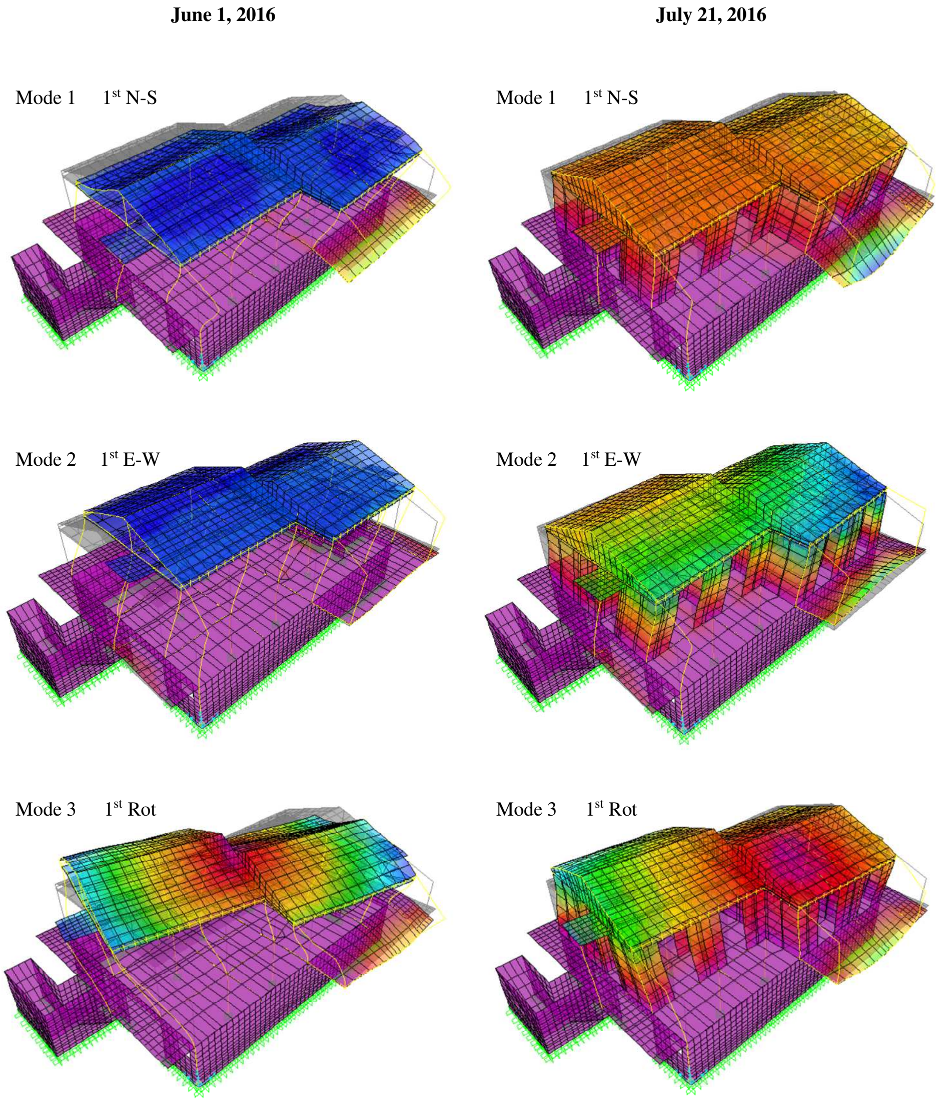

June 1, 2016 **July 21, 2016**

Mode 1 1st N-S Mode 1 1st N-S

Mode 2 1st E-W Mode 2 1st E-W

Mode 3 1st Rot Mode 3 1st Rot

Figure 3.5 Numerical mode shapes for Building 2.

Table 3.24 Comparison between experimental and numerical natural frequencies for Building 1.

Mode	Mode name	Frequency [Hz]			
		August 25, 2016		November 7, 2016	
		Experimental	Numerical	Experimental	Numerical
1	1st N-S	2.57	2.47	5.24	5.20
2	1st E-W	3.32	3.32	5.75	5.71
3	1st Rot	4.12	3.87	6.41	6.14

Table 3.25 Comparison between experimental and numerical natural frequencies for Building 2.

Mode	Mode name	Frequency [Hz]			
		June 1, 2016		July 21, 2016	
		Experimental	Numerical	Experimental	Numerical
1	1st N-S	5.77	5.77	10.71	10.80
2	1st E-W	6.12	6.25	13.04	12.81
3	1st Rot	7.85	7.69	15.75	15.12

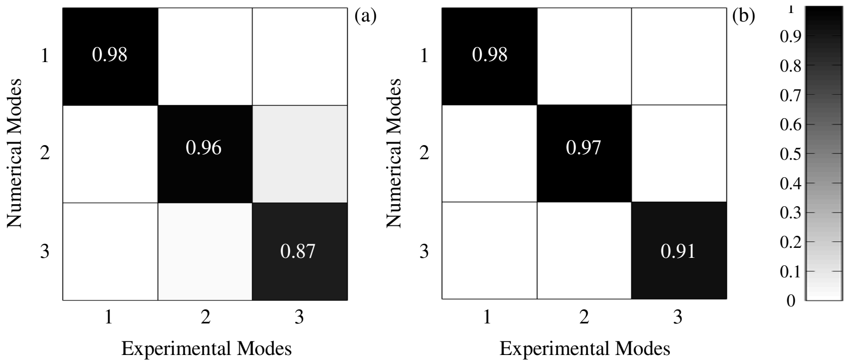

Figure 3.6 MAC indexes for Building 1: (a) August 25, 2016, (b) November 7, 2016.

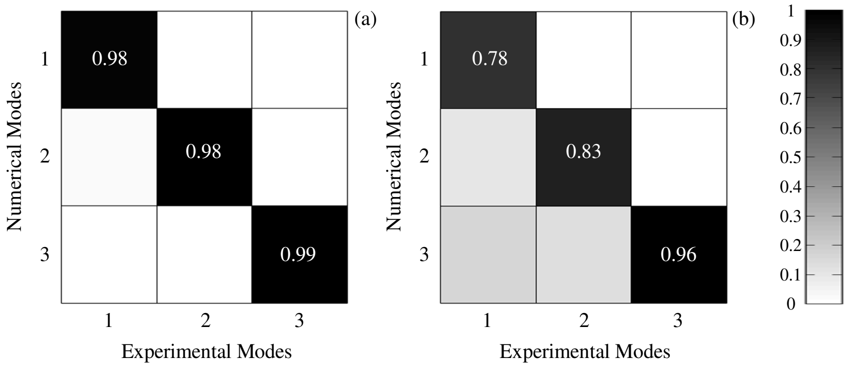

Figure 3.7 MAC indexes for Building 2: (a) June 1, 2016, (b) July 21, 2016.

Chapter 4.

Experimental tests and numerical studies of masonry walls constructed under laboratory conditions

4.1. Specimens descriptions

In the testing Laboratory of Materials and Structures of the Faculty of Engineering at Università Politecnica delle Marche, three masonry wall specimens were built and tested. All the three specimens were composed by the same construction materials (hollow clay bricks, mortar for joints and plaster) used in some infill masonry walls of the buildings case studies investigated and were constructed over a steel plate 1 cm thick. The masonry wall specimens were composed by hollow clay bricks and, in detail, the specimen 1 (S1) with hollow clay bricks with dimensions of 20 x 25 x 19 cm, placed with the 20 cm side in the thickness direction, specimen 2 (S2) by hollow clay bricks with dimensions of 12 x 50 x 25 cm, with the 12 cm side oriented in the thickness direction and specimen 3 (S3) with hollow clay bricks with dimensions of 8 x 25 x 25 cm and with the 8 cm long side in the thickness direction. For all the specimens the bed joints had a thickness of about 1 cm, while the head joints were almost completely absent and the two main faces were covered by plaster layer 1.50 cm thick. In Table 4.1 specific weight of the three specimens before and after the plaster realization are listed. In Figure 4.1 the geometry of the specimens is illustrated, while Figure 4.2 displays some pictures inherent to their construction process.

Table 4.1 Specific weight of the specimens.

Specimen	Specific weight [kN/m^3]	
	Without plaster	With plaster
S1	7.98	8.81
S2	8.70	9.77
S3	6.52	8.67

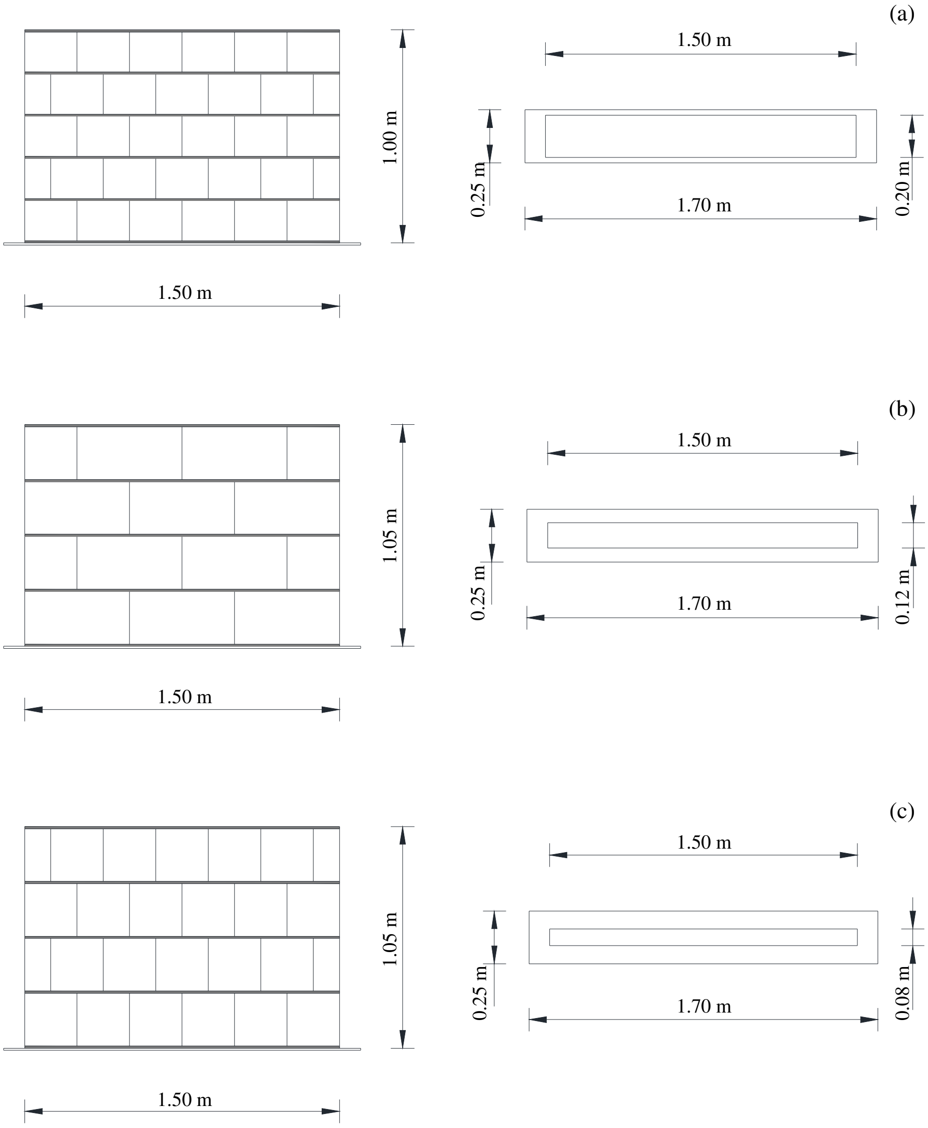

Figure 4.1 Specimens geometry: (a) S1, (b) S2, (c) S3.

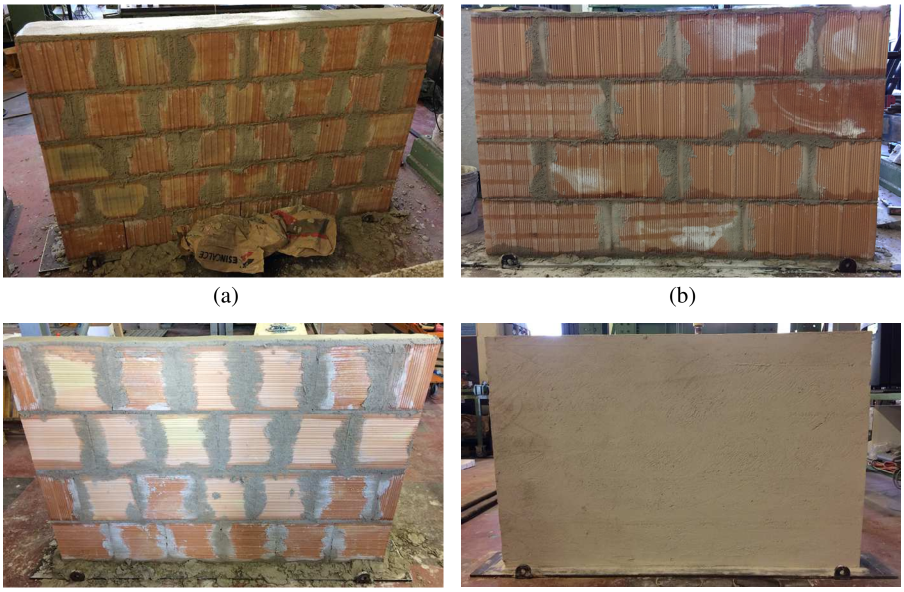
(a) (b)

(c) (d)

Figure 4.2 Pictures of the specimens during the construction: (a) S1, (b) S2, (c) S3, (d) S3 with plaster.

4.2. Experimental dynamic tests

4.2.1. *Dynamic tests set up*

The instrumentation used to perform the experimental dynamic tests on the specimens is the same used for the in situ dynamic tests on the infill masonry walls and consists of a PCB Impulse Force Test Hammer (model 086D20), two PCB uniaxial shear piezoelectric accelerometers (sensitivity of 0.3 V/g and frequencies range samples of 1-2000 Hz), a 24-bit Data Acquisition system (DAQ) with chassis and cabling to connect the hammer and the accelerometers to the acquisition system. The latter is connected to a laptop equipped with a LabView software able to store the recorded data. The acquisition parameters adopted for all the performed tests are listed in Table 4.2.

Table 4.2 Acquisition parameters.

Sampling frequency	51200	Hz
Number of samples	51200	(each hammer impact)
Time length	1	s (each hammer impact)

The aim of the tests performed is the investigation of the out of plane dynamic behaviour of the specimens and then, the estimation of their mechanical properties on the basis of these results. All the experimental tests were performed on one face of the walls. The methodology adopted to conduct the tests was almost the same adopted to perform the in situ dynamic tests on the infill masonry walls and it is summarized hereinafter. The masonry panel was divided with a regular grid of 25 points where the impulsive forces were applied and the accelerometers were placed. The vertical lines were identified with a letter starting from the left, while the horizontal lines with a number starting from the top, so that each grid point was identified with an alphanumeric code. The two accelerometers, called Acc.1 and Acc.2, were placed on two grid points recognised with C1 and E3 code, respectively, with the aim to identify as many vibrational modes as possible. The accelerometers, measuring along the horizontal direction perpendicular to the infill panels, were fixed by means of hot glue. The accelerometers and the hammer were connected to the acquisition system by means of coaxial cables. The acquisition system was connected to the laptop through an USB cable. The tests started applying the impulsive forces at each grid point using the instrumented hammer, while the accelerometers remained always in the same positions. For each impact point three or more impulsive forces were applied so to get a reliable data set. Data recorded during the in situ tests have to be checked and processed before their use in a software for the determination of the modal parameters. For each grid point the strokes that show anomalous signals, both in terms of impulse and acceleration measurements, were discarded. Moreover, for all the impact points the number of strokes has to be the same (usually three or four strokes) so the strokes in excess were removed from the data set. Finally, the number of data was reduced through resampling with lower frequency values.

A schematic layout of the grid used for the specimen S1 is shown in Figure 4.3, while for the specimens S2 and S3 is shown in Figure 4.4. It is worth noting that the out of plane dynamic tests are repeated before and after the realization of the plaster for all the specimens (Figure 4.5). Furthermore, the tests conducted on the specimens after the plaster realization are replicated keeping the walls suspended from the ground by means of chains hooked into four points of the base steel plate, as is shown in Figure 4.6.

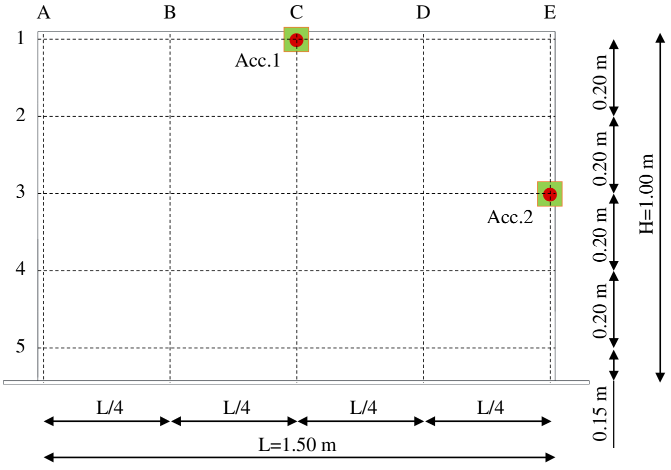

Figure 4.3 Schematic layout of the standard measuring grids on the specimen S1.

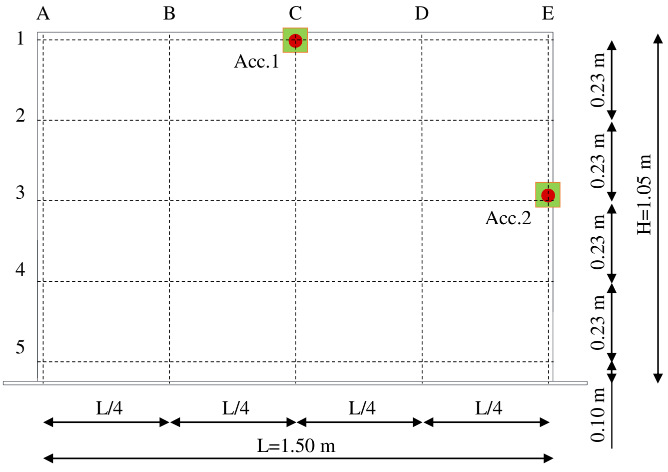

Figure 4.4 Schematic layouts of the standard measuring grids on the specimens S2 and S3.

Figure 4.5 Impact out of plane tests: (a) before plaster, (b) after plaster.

Figure 4.6 Impact out of plane tests with the suspended specimens.

4.2.2. *Impact test results*

The results obtained from the data recorded during the dynamic tests previously described are the modal parameters of the tested specimens relevant to their out of plane dynamic behaviour. The modal analysis whose made the determination of these parameters possible were carried out through the ModalView software, capable to identify the natural frequencies and the corresponding mode shapes.

As regard the tests without plaster and considering the specimens leaned on the ground, the out of plane results in terms of natural frequencies are reported in Table 4.3 for the specimen S1, in Table 4.4 for the specimen S2 and in Table 4.5 for the specimen S3; the relevant mode shapes are displayed in Figure 4.7, Figure 4.8 and Figure 4.9, respectively.

Considering the tests performed on the same walls leaned on the ground but after the plaster realization, the natural frequencies are listed from Table 4.6 to Table 4.8; the corresponding mode shapes are shown from Figure 4.10 to Figure 4.12.

Considering the tests with the plastered panels suspended from the ground, the results in terms of natural frequencies for the out of plane dynamic behaviour are listed in Table 4.9 up to Table 4.11 and the relevant mode shapes in Figure 4.13 up to Figure 4.15.

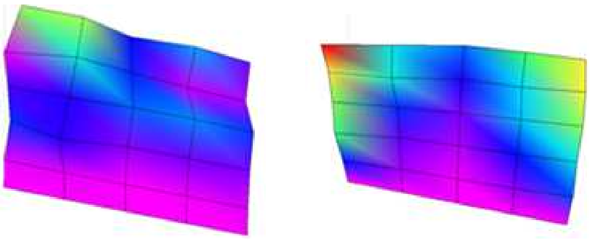

Mode 1 Mode 2

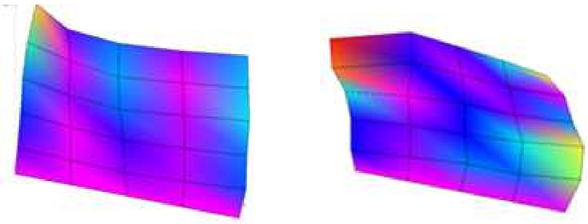

Mode 3 Mode 4

Figure 4.7 Experimental out of plane mode shapes for the specimen S1 without plaster and leaned on the ground.

Table 4.3 Experimental out of plane natural frequencies for the specimen S1 without plaster and leaned on the ground.

Mode	Mode name	Frequency [Hz]
1	I-vertical	19.00
2	I-horizontal	52.21
3	II-horizontal	121.40
4	II-vertical	190.25

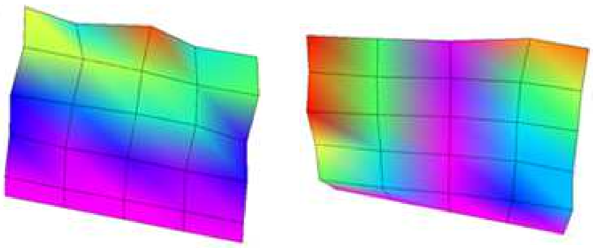

Mode 1 Mode 2

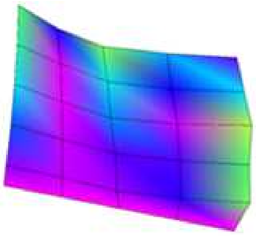

Mode 3

Figure 4.8 Experimental out of plane mode shapes for the specimen S2 without plaster and leaned on the ground.

Table 4.4 Experimental out of plane natural frequencies for the specimen S2 without plaster and leaned on the ground.

Mode	Mode name	Frequency [Hz]
1	I-vertical	11.87
2	I-horizontal	62.15
3	II-horizontal	170.30

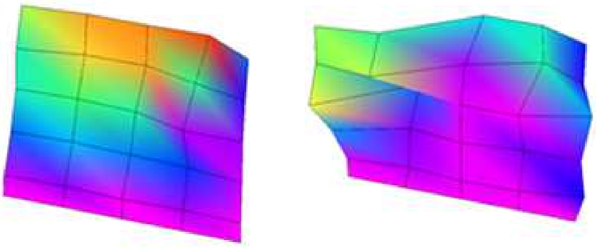

Mode 1 Mode 2

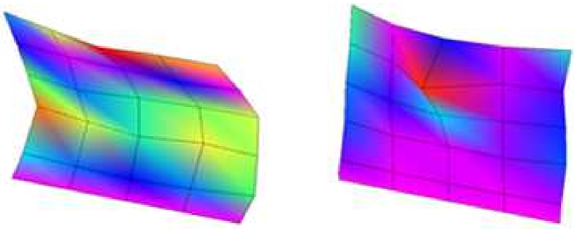

Mode 3 Mode 4

Figure 4.9 Experimental out of plane mode shapes for the specimen S3 without plaster and leaned on the ground.

Table 4.5 Experimental out of plane natural frequencies for the specimen S3 without plaster and leaned on the ground.

Mode	Mode name	Frequency [Hz]
1	I-vertical	14.85
2	I-horizontal	37.26
3	II-vertical	101.40
4	II-horizontal	127.30

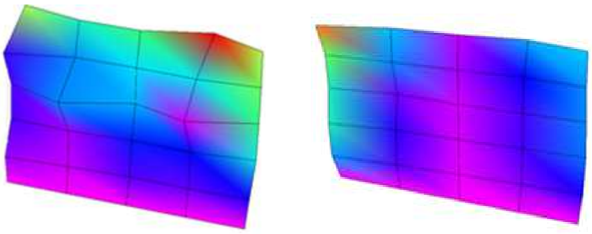

Mode 1 Mode 2

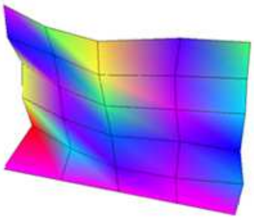

Mode 3

Figure 4.10 Experimental out of plane mode shapes for the specimen S1 with plaster and leaned on the ground.

Table 4.6 Experimental out of plane natural frequencies for the specimen S1 with plaster and leaned on the ground.

Mode	Mode name	Frequency [Hz]
1	I-vertical	20.72
2	I-horizontal	75.66
3	II-horizontal	219.20

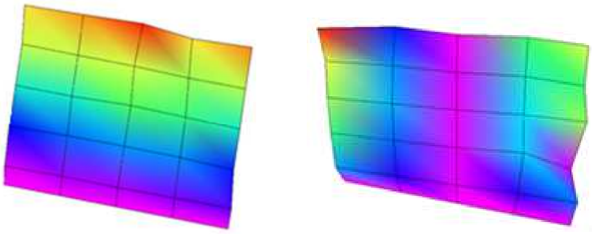

Mode 1 Mode 2

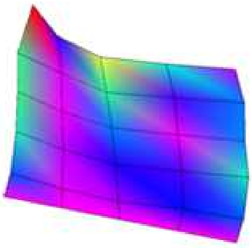

Mode 3

Figure 4.11 Experimental out of plane mode shapes for the specimen S2 with plaster and leaned on the ground.

Table 4.7 Experimental out of plane natural frequencies for the specimen S2 with plaster and leaned on the ground.

Mode	Mode name	Frequency [Hz]
1	I-vertical	12.22
2	I-horizontal	71.23
3	II-horizontal	193.33

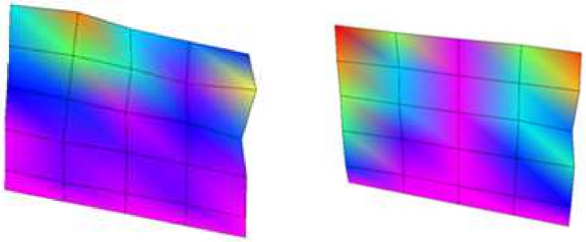

Mode 1 Mode 2

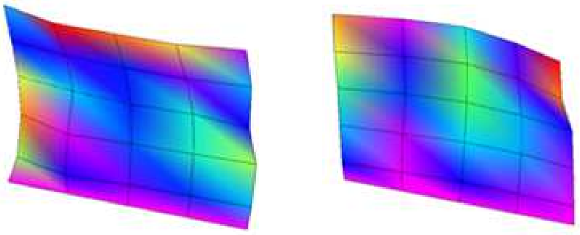

Mode 3 Mode 4

Figure 4.12 Experimental out of plane mode shapes for the specimen S3 with plaster and leaned on the ground.

Table 4.8 Experimental out of plane natural frequencies for the specimen S3 with plaster and leaned on the ground.

Mode	Mode name	Frequency [Hz]
1	I-vertical	17.00
2	I-horizontal	53.16
3	II-vertical	132.80
4	II-horizontal	156.80

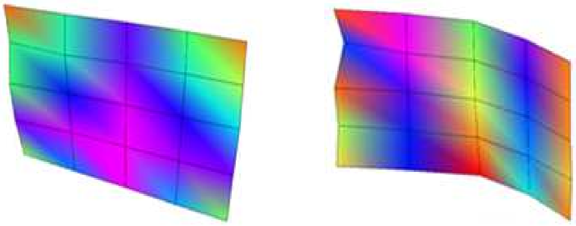

Mode 1 Mode 2

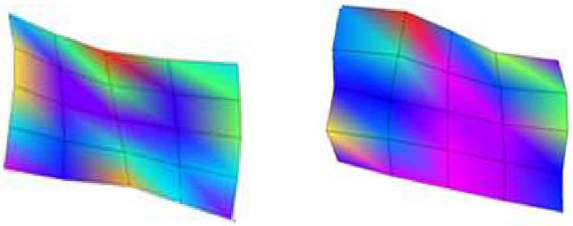

Mode 3 Mode 4

Figure 4.13 Experimental out of plane mode shapes for the specimen S1 with plaster and suspended.

Table 4.9 Experimental out of plane natural frequencies for the specimen S1 with plaster and suspended.

Mode	Mode name	Frequency [Hz]
1	A	154.83
2	B	184.73
3	C	314.30
4	D	452.63

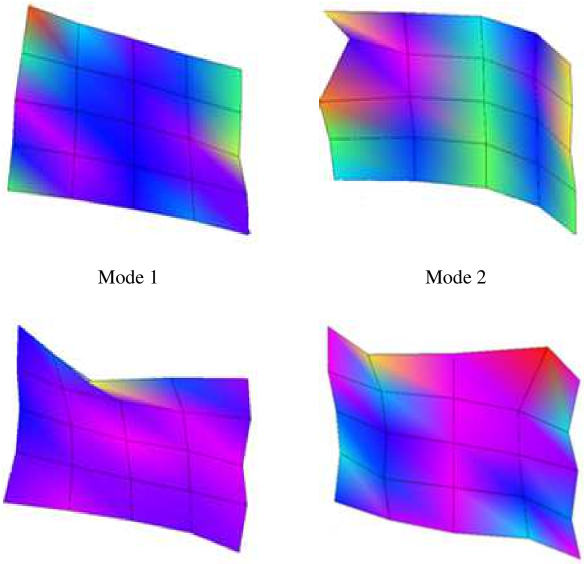

Mode 1 Mode 2

Mode 3 Mode 4

Figure 4.14 Experimental out of plane mode shapes for the specimen S2 with plaster and suspended.

Table 4.10 Experimental out of plane natural frequencies for the specimen S2 with plaster and suspended.

Mode	Mode name	Frequency [Hz]
1	A	122.40
2	B	159.63
3	E	256.66
4	D	393.10

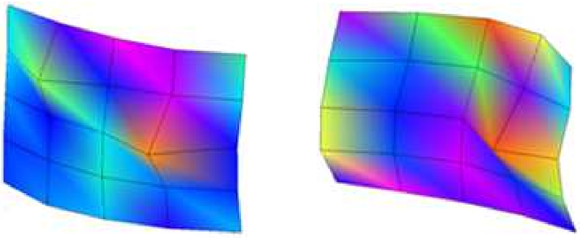

Mode 1 Mode 2

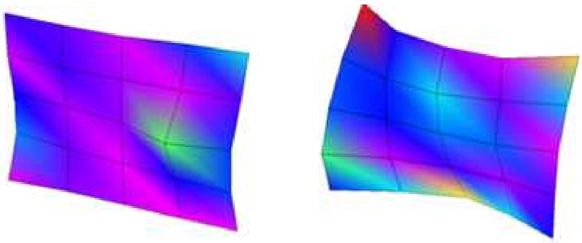

Mode 3 Mode 4

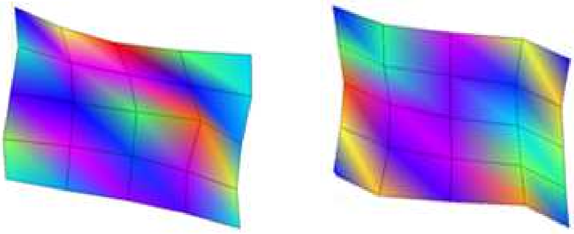

Mode 5 Mode 6

Figure 4.15 Experimental out of plane mode shapes for the specimen S3 with plaster and suspended.

Table 4.11 Experimental out of plane natural frequencies for the specimen S3 with plaster and suspended.

Mode	Mode name	Frequency [Hz]
1	F	117.55
2	G	148.30
3	A	198.20
4	H	216.40
5	I	286.30
6	D	330.58

In Table 4.12 and Table 4.13 the experimental out of plane natural frequencies obtained from the three tested specimens leaned on the ground before and after the plaster realization are summarized. Considering the results before the realization of the plaster it is not possible to individuate a correlation between the modes order and the thickness of the specimens while, in the case with plaster, it can be observed that the wall with higher block thickness (S1) reaches the highest values of natural frequencies and vice versa, except for the first mode, where the specimen S3 (hollow clay block thickness of 8 cm) has a higher frequency value with respect to the specimen S2 (hollow clay block thickness of 12 cm). It is worth noting that the first frequency value is not very reliable inasmuch it can be affected by the constraint conditions, whose can be considered neither as fixed or simply supported. After the realization of the plaster it can be seen that the frequency values are greater than those obtained in the case without plaster; in particular, the percentage increase of the frequency values obtained after the plaster realization ranges from a minimum of 3% to a maximum of 81% considering all the tested specimens (Table 4.14). Considering the specimen S1 it can be noted that the mode called II-vertical has not been found in the case with plaster and for the specimen S2 this mode is never found; furthermore, for the specimen S3, the modes called II-horizontal and II-vertical are reversed with respect to the other specimens, both in the case without and with plaster.

In Table 4.15 the values of out of plane natural frequencies for the specimens with plaster and suspended from the ground are listed. Only for three modes it is possible to make a comparison among the specimens; in particular, considering the mode called A, it is possible to see that the higher value of frequencies is reached by the specimen S3, then the second one is relative to the specimen S1 and, at the end, the last value is relative to the specimen S2. Instead, for the mode called D, the higher value of frequency is achieved by the specimen S1, then S2 and lastly S3. This frequency order is the same found for the specimens simply supported on the ground and with plaster. Also for the mode B, that it has been identified only for the specimen S1 and S2, the higher value of frequency is reached for the specimen S1 and then S2.

Table 4.12 Experimental out of plane natural frequencies for the specimens tested before the plaster realization and leaned on the ground.

Mode name	Frequency [Hz]		
	S1	S2	S3
I-vertical	19.00	11.87	14.85
I-horizontal	52.21	62.15	37.26
II-horizontal	121.40	170.30	127.30
II-vertical	190.25	/	101.40

Table 4.13 Experimental out of plane natural frequencies for the specimens tested after the plaster realization and leaned on the ground.

Mode name	Frequency [Hz]		
	S1	S2	S3
I-vertical	20.72	12.22	17.00
I-horizontal	75.66	71.23	53.16
II-horizontal	219.20	193.33	156.80
II-vertical	/	/	132.80

Table 4.14 Percentage change of the out of plane natural frequency values for the specimens tested after the plaster realization.

Mode name	Frequency percentage change [%]		
	S1	S2	S3
I-vertical	+9	+3	+14
I-horizontal	+45	+15	+43
II-horizontal	+81	+14	+23
II-vertical	/	/	+31

Table 4.15 Experimental out of plane natural frequencies for the specimens tested after the plaster realization and suspended from the ground.

Mode name	Frequency [Hz]		
	S1	S2	S3
A	154.83	122.40	198.20
B	184.73	159.63	/
C	314.30	/	/
D	452.63	393.10	330.58
E	/	256.66	/
F	/	/	117.55
G	/	/	148.30
H	/	/	216.40
I	/	/	286.30

4.3. In plane lateral load tests

4.3.1. Test programme

In plane lateral load tests for the characterization of the specimen material properties were performed after the plaster realization. These tests were useful in determining the mechanical properties of the masonry and, in particular, the elastic modulus *E*. The horizontal load was applied in terms of programmed forces, cyclically imposed in one direction (under compression), with step-wise increased amplitudes up to the collapse of the specimens. The load was applied approximately at the top of the walls, at a distance about 95 cm from the base. During the tests, forces acting on the walls and displacements due to their application were measured and recorded. In detail, to monitor the displacements during the tests, seven displacement transducers were used: three measuring in horizontal direction (one at the bottom, one in half and one at the top of the specimens), three measuring in vertical direction (one in the upper right and one in the upper left parts of the walls and one at the bottom right part) and one along the diagonal direction of the panels. In order to prevent the rotation of the walls due to the horizontal forces, two vertical steel ties were used to take the tension forces developed on the tensioned side of the walls. Figure 4.16 shows an example of the test set up for the specimen S3, while Figure 4.17 shows a schematic layout valid for all the specimens and where the positions of the displacement transducers and of the horizontal force are indicated.

Figure 4.16 Set up of the experimental lateral load tests.

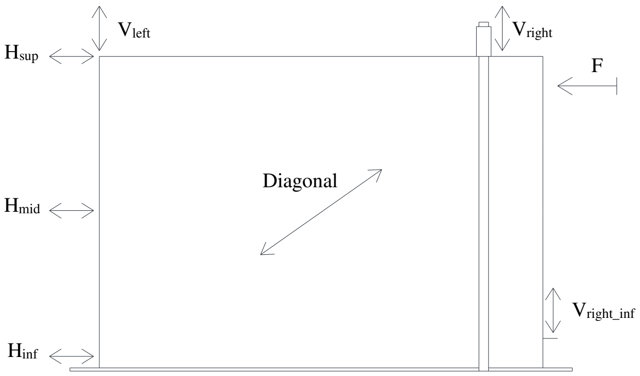

Figure 4.17 Force and displacements measuring layout for the lateral load tests.

4.3.2. *Test results*

For each specimen some loading and unloading cycles were performed at different levels of horizontal forces and all the walls failed with a diagonal shear crack that follows the bed and head joints of the masonry. Only for the specimen S2, in addition to the shear crack, another vertical crack opened on the opposite side with respect to the one where the force was applied.

For the specimen S1 six loading and unloading cycles were performed (10 kN, 15 kN, 40 kN, 50 kN and two at 70 kN) and the wall failed at a force value about 70kN. The specimen S2 was subjected to three loading and unloading cycles (40 kN, 50 kN and 50 kN again) and the first cracks appeared at a horizontal force of about 50 kN. Finally, the specimen S3 was tested with six loading and unloading cycles (10 kN, 20 kN, 30 kN, 40 kN, 49 kN and 55kN) and the end of the test is determined by cracks at a horizontal force of about 55 kN.

Figure 4.18 displays the cracks over the walls at the end of the tests and after the plaster removal. Figure 4.19 up to Figure 4.21 show the displacements monitored during the tests for all the specimens. As concerns the horizontal displacements before the collapse, for all specimens it is possible to see that the maximum one is reached at the top of the wall, then in the middle and lastly at bottom. This proves that the in plane deformation of the panel increases by moving away from the base, assuming a deformation shape that varies from double fixed to cantilever, according to the constraint conditions. The vertical displacements are lower than the horizontal ones but not equal to zero, so it is evident that the specimens slightly rotate during the application of the horizontal forces. The diagonal displacements are very low for all specimens at each loading phase but not equal to zero, demonstrating that the horizontal forces applied at the top of the walls allow the compressed diagonal to be established along the specimen. For the specimen S1 and S3 the last cycle (the one corresponding to the cracking) lead to high horizontal displacements at the top, in the middle and at the bottom after the break. The high displacements of the specimen S1 (both horizontal and vertical) of the first cycles are due probably to a low screws tighten of the two vertical steel ties.

Specimen S1

Specimen S2

Specimen S3

Figure 4.18 Damage to masonry specimens at the end of the lateral load tests.

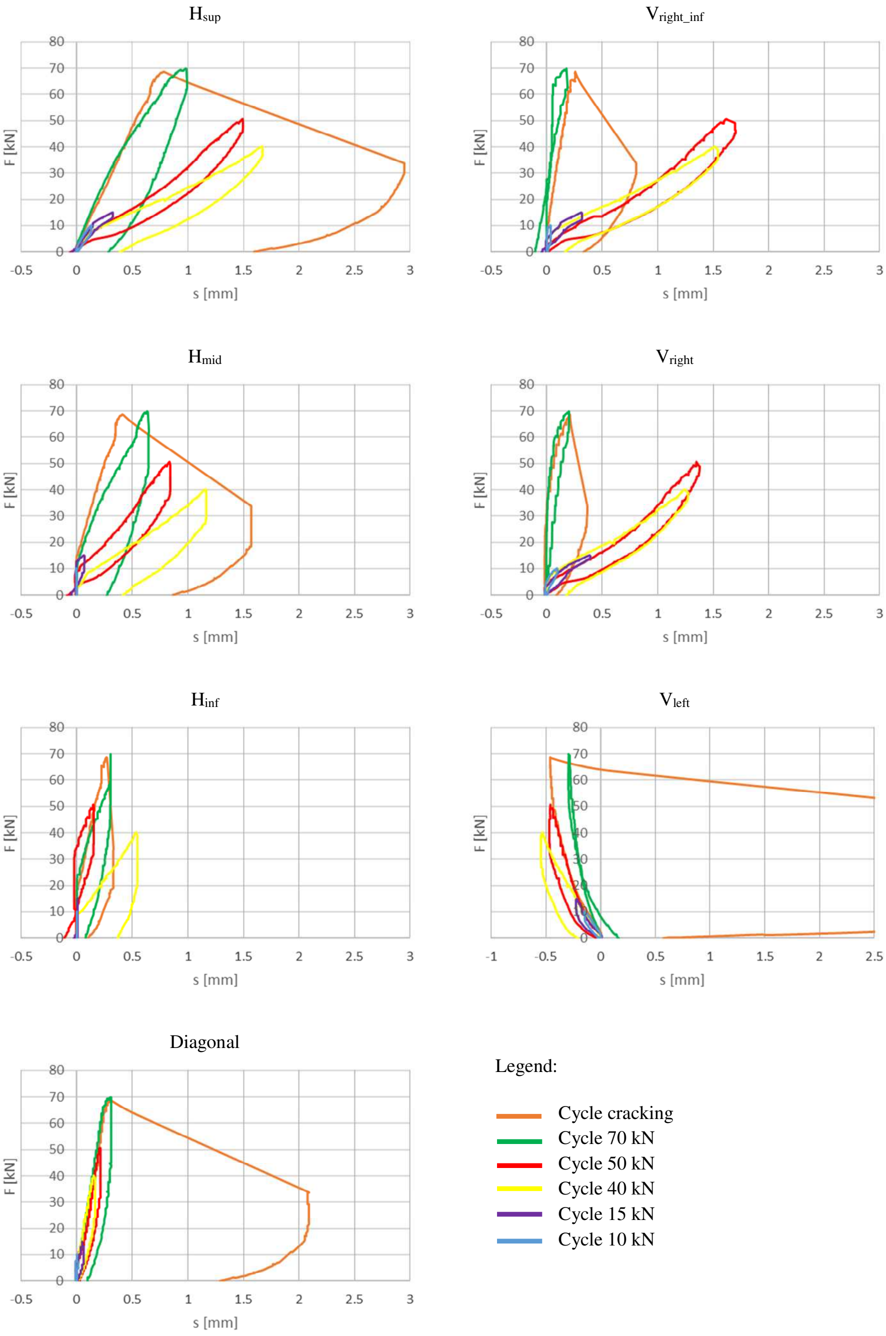

Figure 4.19 Displacements recorded during the lateral load tests on the specimens S1.

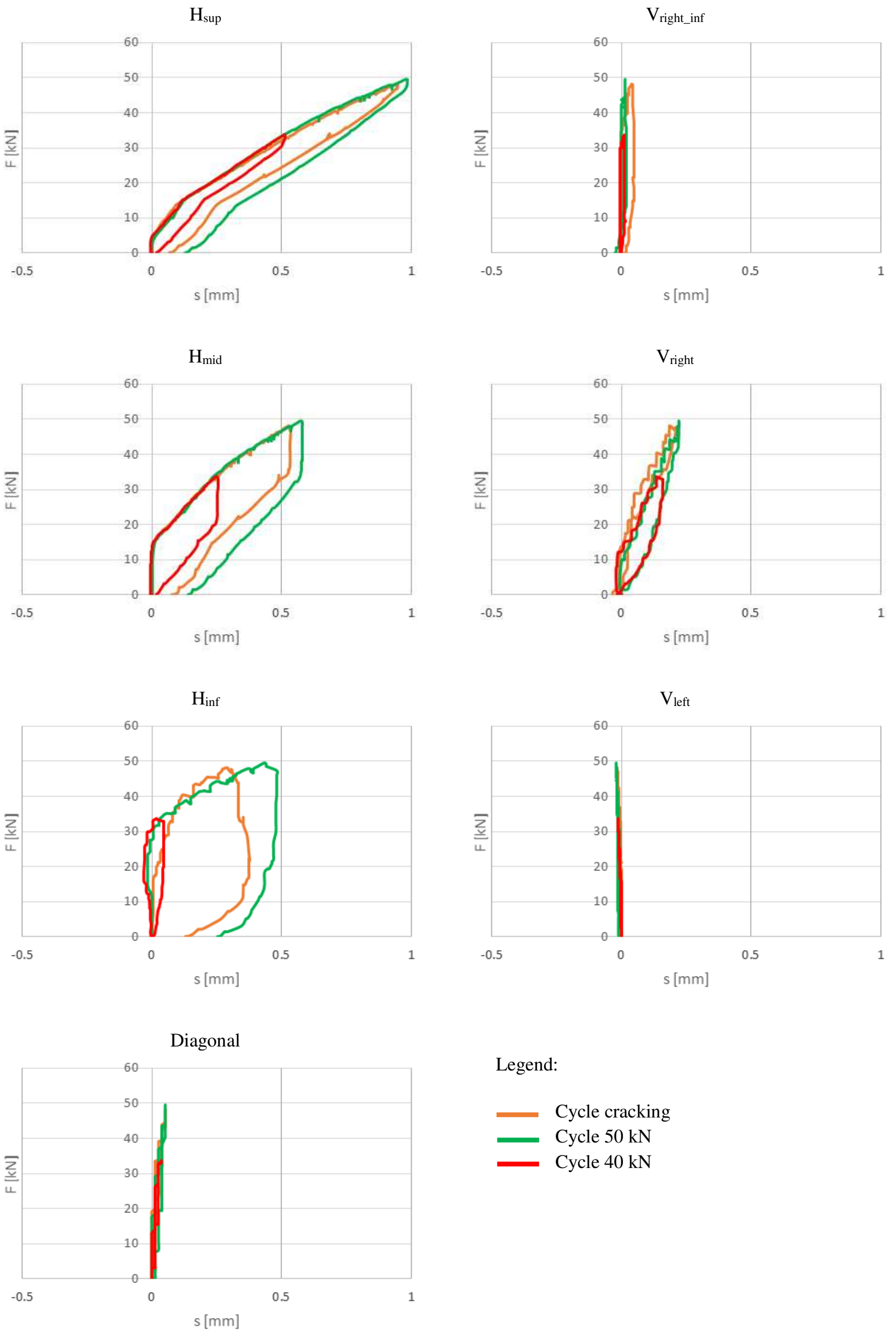

Figure 4.20 Displacements recorded during the lateral load tests on the specimens S2.

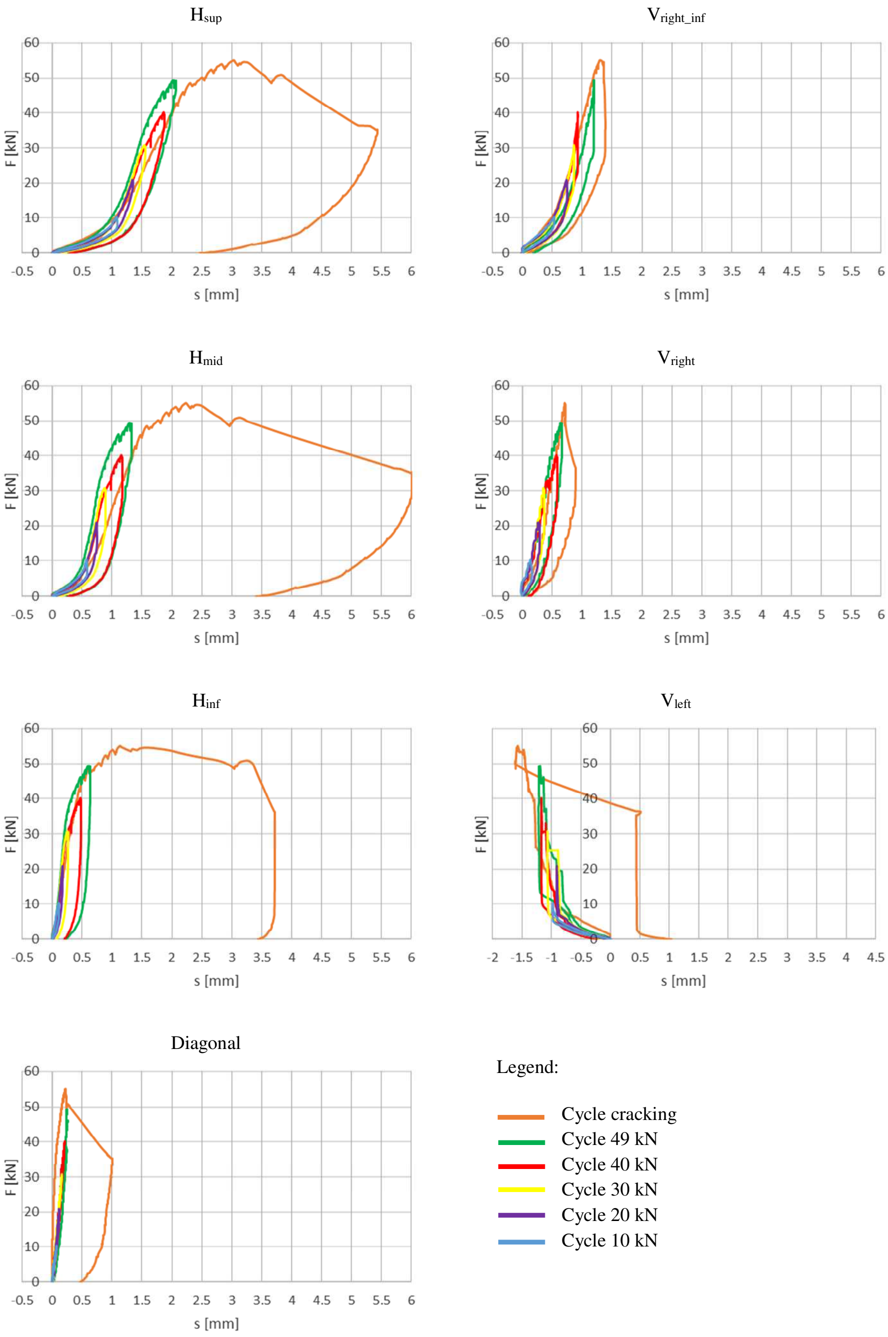
H_{sup}

V_{right_inf}

H_{mid}

V_{right}

H_{inf}

V_{left}

Diagonal

Figure 4.21 Displacements recorded during the lateral load tests on the specimens S3.

4.4. Estimation of the mechanical properties of the specimens masonry

4.4.1. *Mechanical properties determined by dynamic test results*

To estimate the mechanical properties of the specimens masonry on the basis of the dynamic test results, numerical f.e. models are developed by means of the code SAP2000. For the out of plane dynamic tests with the specimens simply supported on the ground, each wall is modelled with shell elements with the same geometric dimensions of the real walls (length, height and thickness) (Figure 4.22a). The shell element (or each sub-shell element of a meshed area) has its own element local coordinate system that is used to define material properties, loads and output. The axes of this local system are denoted 1, 2 and 3. The first two axes lie in the plane of the element while the third axis is normal. The two lateral vertical edge and the upper edge of the walls are free, while the lower edge is considered fixed in the three translational global directions (*X*, *Y* and *Z*). Furthermore, to simulate the fact that the plate is not perfectly flat and the out of plane dynamic behaviour of the walls could be influenced by its small rotation, rotational springs are added at all the basement joints. The stiffness values of these springs are evaluated on the bases of the first out of plane frequency of the specimens. The masses of the walls are automatically considered by the software according to their geometry and considering the specific weight previously determined. To analyse the suspended specimens the developed f.e. models are similar to those described before. Moreover, in this case also the steel base plate is modelled in continuity with the infill walls. To simulate the fact that the suspended specimens are considerate free in the three-dimensional space, three elastic springs are modelled as constraint conditions in each of the four hooking points of the steel base plate. These springs are placed in *X*, *Y* and *Z* global directions with very low values of stiffness (Figure 4.22b). In order to obtain the natural frequencies and the relevant mode shapes, modal analysis with eigen-vectors are carried out. With the second modelling strategy (for the suspended specimens), the first vibrational modes of the specimens represent the rigid displacements in the space and so these are discarded, considering only the subsequent vibration modes of the wall specimens.

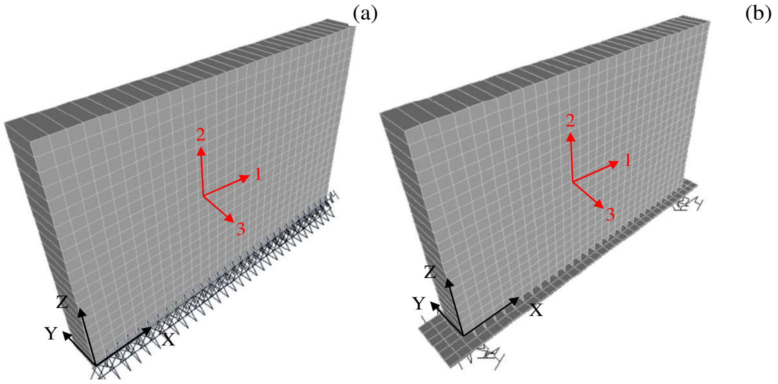

Figure 4.22 F.e. models developed: (a) simply supported specimens, (b) suspended specimens.

The masonry mechanical properties, i.e. the elastic modulus *E*, the shear modulus *G* and the Poisson's coefficient ν, are investigated and updated taking into account the abovementioned modelling strategies, assuming that the geometric characteristics (length, height and thickness) and the masses are known. The target is to determine the mechanical properties in such a way that the numerical modal parameters fit the experimental ones (i.e. obtained by the dynamic tests). The shell elements representing the infill masonry walls are considered as thin shell elements, i.e., their plate bending behaviour is governed by the Kirchhoff's theory, neglecting transverse shear deformation; the masonry material is considered as isotropic. The Kirchhoff's formulation is governed by a differential equation for the deflection that depends on the thickness of the plate *h* and, through the constant *D*, on two mechanical properties of the material: the elastic modulus *E* and the Poisson's coefficient ν, as is shown in the following formula

$$D = \frac{Eh^3}{12\left(1-\nu^2\right)} \tag{29}$$

The Poisson's coefficient ν is assumed to be constant and equal to 0.2 as its variation does not significantly affect the out of plane dynamic behaviour of the shell, while the only unknown parameter of the material mechanical properties is the elastic modulus *E*, which is calibrated during the updating procedure.

As concerns the out of plane dynamic behaviour of the simply supported specimens, the updating procedures conclude when the numerical modal parameters fit the experimental ones. It is worth noting that the first experimental out of plane modes for all specimens are not to consider reliable since it is reasonable to think that they can be affected by the constraint conditions. Moreover, the updating procedures are performed both in the case without and with plaster. The elastic moduli for all the specimens obtained at the end of the updating procedures are listed in Table 4.16. As can be seen, the values for the specimen S2 are in good agreement with those obtained from the in situ tests for the walls 12 cm thick called W3-F (in particular in the case with plaster), while for the other specimens the elastic moduli are quite different from those obtained by the in situ tests on the walls with thickness of 8 cm (W2-F and W3-A) and 20 cm (W1-F).

Lastly, the elastic moduli estimated with the updating procedure considering the out of plane dynamic behaviour of the suspended specimens are listed in Table 4.17. As before, the updating procedure concludes when the numerical out of plane modal parameters fit the experimental ones. Comparing these results with those obtained by the in situ tested walls with the same thickness, it is possible to see how the elastic moduli are quite different from each other.

Table 4.16 Elastic moduli *E* estimated by the out of plane dynamic behaviour of the simply supported specimens.

Specimen	E [MPa]	
	Without plaster	With plaster
S1	900	1900
S2	4500	4700
S3	2700	3600

Table 4.17 Elastic moduli *E* estimated by the out of plane dynamic behaviour of the suspended specimens.

Specimen	E [MPa] With plaster
S1	2700
S2	5200
S3	4500

Making a comparison between the elastic moduli determined by the out of plane dynamic test results for both simply supported and suspended specimens, it is possible to determine a repetitive correlation between them. In fact, the higher value of elastic modulus is that one obtained for the specimen S2 (hollow clay brick with thickness of 12 cm), then the one for the specimen S3 (hollow clay brick 8 cm thick) and lastly the one relevant to the specimen S1 (hollow clay brick with thickness of 20 cm).

From Table 4.18 to Table 4.26 the out of plane natural frequencies for all modes of each investigated specimen are reported. In particular, the experimental natural frequencies obtained for different type of dynamic tests (simply supported and suspended specimens, before and after the realization of the plaster) are listed next to the numerical ones obtained from the f.e. models previously described and using the mechanical masonry properties resulting from the updating procedures performed before. Considering the out of plane tests for the simply supported specimens without plaster, it can be observed that the numerical natural frequencies are in good agreement with the experimental ones. The same consideration can be done for the case with plaster. For the out of plane dynamic tests with the suspended specimens it can be noted that the numerical natural frequencies are in quite good agreement with the experimental ones, but worse than before with the specimens leaned on the ground. Moreover, for the specimens S3 the first and the third numerical modes are not found.

Table 4.18 Out of plane natural frequencies for the specimen S1 without plaster and leaned on the ground.

Mode	Mode name	Frequency [Hz]	
		Experimental	Numerical
1	I-vertical	19.00	20.08
2	I-horizontal	52.21	52.98
3	II-horizontal	121.40	137.09
4	II-vertical	190.25	166.81

Table 4.19 Out of plane natural frequencies for the specimen S2 without plaster and leaned on the ground.

Mode	Mode name	Frequency [Hz]	
		Experimental	Numerical
1	I-vertical	11.87	12.26
2	I-horizontal	62.15	59.22
3	II-horizontal	170.30	166.62

Table 4.20 Out of plane natural frequencies for the specimen S3 without plaster and leaned on the ground.

Mode	Mode name	Frequency [Hz]	
		Experimental	Numerical
1	I-vertical	14.85	14.86
2	I-horizontal	37.26	38.90
3	II-vertical	101.40	102.32
4	II-horizontal	127.30	118.07

Table 4.21 Out of plane natural frequencies for the specimen S1 with plaster and leaned on the ground.

Mode	Mode name	Frequency [Hz]	
		Experimental	Numerical
1	I-vertical	20.72	20.33
2	I-horizontal	75.66	78.49
3	II-horizontal	219.20	214.37

Table 4.22 Out of plane natural frequencies for the specimen S2 with plaster and leaned on the ground.

Mode	Mode name	Frequency [Hz]	
		Experimental	Numerical
1	I-vertical	12.22	12.03
2	I-horizontal	71.23	70.63
3	II-horizontal	193.33	200.12

Table 4.23 Out of plane natural frequencies for the specimen S3 with plaster and leaned on the ground.

Mode	Mode name	Frequency [Hz]	
		Experimental	Numerical
1	I-vertical	17.00	16.75
2	I-horizontal	53.16	51.40
3	II-vertical	132.80	139.22
4	II-horizontal	156.80	156.92

Table 4.24 Out of plane natural frequencies for the specimen S1 with plaster suspended.

Mode	Mode name	Frequency [Hz]	
		Experimental	Numerical
1	A	154.83	154.13
2	B	184.73	216.09
3	C	314.30	409.34
4	D	452.63	469.14

Table 4.25 Out of plane natural frequencies for the specimen S2 with plaster suspended.

Mode	Mode name	Frequency [Hz]	
		Experimental	Numerical
1	A	122.40	122.13
2	B	159.63	193.80
3	E	256.66	364.75
4	D	393.10	340.53

Table 4.26 Out of plane natural frequencies for the specimen S3 with plaster suspended.

Mode	Mode name	Frequency [Hz]	
		Experimental	Numerical
1	F	117.55	/
2	G	148.30	148.79
3	A	198.20	/
4	H	216.40	185.73
5	I	286.30	315.63
6	D	330.58	349.80

4.4.2. Mechanical properties determined by the lateral load test results

In this part the interpretation of the experimental data of the lateral load tests will be discussed for each considered masonry typology. A common approach to interpret the in plane response of masonry walls is to idealize the behaviour of the masonry panel subjected to a sequence of lateral loads with a bilinear envelope (Magenes et al., 2008) (Figure 4.23).

The first step in the evaluation of the bilinear curve is the construction of a cyclic envelope of the displacement curves. The second step is the evaluation of the elastic stiffness k_{el} which is obtained by drawing the secant to the experimental envelope at $0.70V_{max}$, where V_{max} is the maximum shear of the envelope curve:

$$\begin{cases} k_{el} = \dfrac{V_{cr}}{\delta_{cr}} \\ V_{cr} = 0.70 \cdot V_{\max} \end{cases} \tag{30}$$

The third step consists of the estimation of the ultimate displacement (δ_u). The ultimate displacement on the envelope curve is evaluated as the displacement corresponding to a strength degradation equal to 20% of V_{max}. The value of the shear V_u, corresponding to the horizontal branch of the bilinear curve, has been found by ensuring that the areas below the cyclic envelope curve (evaluated numerically as a sum of discrete areas A_i) and below the equivalent bilinear curve are equal.

$$\begin{cases} A_{envelope} = \sum A_i \\ A_{bilinear} = V_u \cdot \delta_u - \dfrac{V_u^2}{2 \cdot k_{el}} \end{cases} \tag{31}$$

$$V_u = k_{el} \cdot \left[\delta_u - \sqrt{\delta_u^2 - \frac{2 \cdot A_{envelope}}{k_{el}}} \right] \tag{32}$$

Knowing the elastic stiffness k_{el} and the value of V_u, it is possible to evaluate the elastic displacement δ_e (or δ_y) as V_u/k_{el}.

Figure 4.24 up to Figure 4.26 display the construction of bilinear curves for each specimen, while Table 4.27 up to Table 4.29 summarize the main features of these bilinear curves. For the specimen S3 the first part of the test results (data between 0 kN and 10 kN of horizontal force level) is neglected, inasmuch in this range the behaviour of the wall is strongly different from the rest of the curve and seems to be influenced by other external factors.

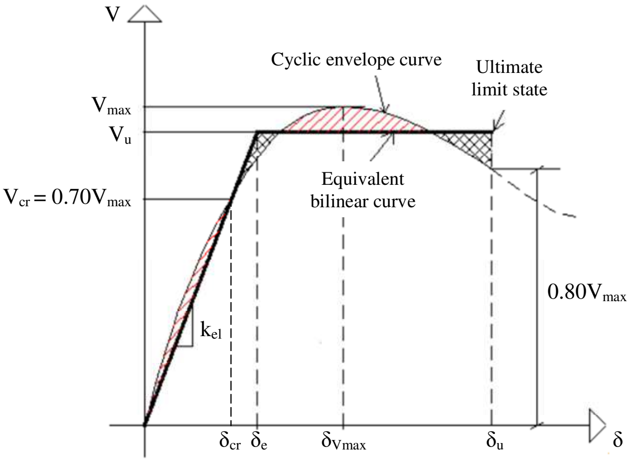

Figure 4.23 Lateral displacements envelope and its bilinear idealization.

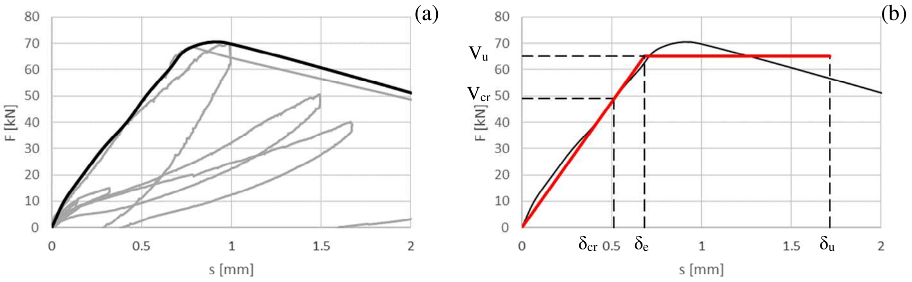

Figure 4.24 Bilinear idealization of the specimen S1: (a) envelope of the top horizontal displacements, (b) bilinear curve.

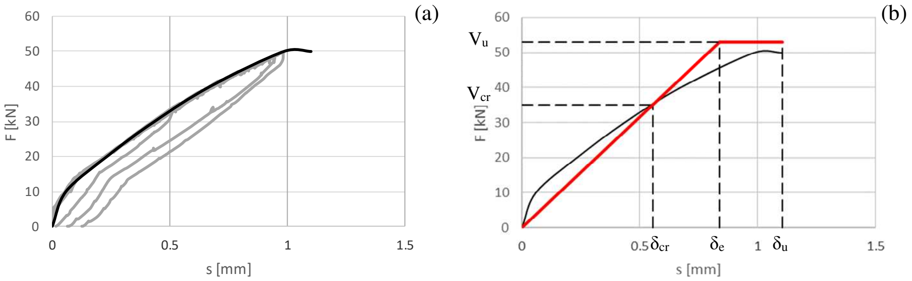

Figure 4.25 Bilinear idealization of the specimen S2: (a) envelope of the top horizontal displacements, (b) bilinear curve.

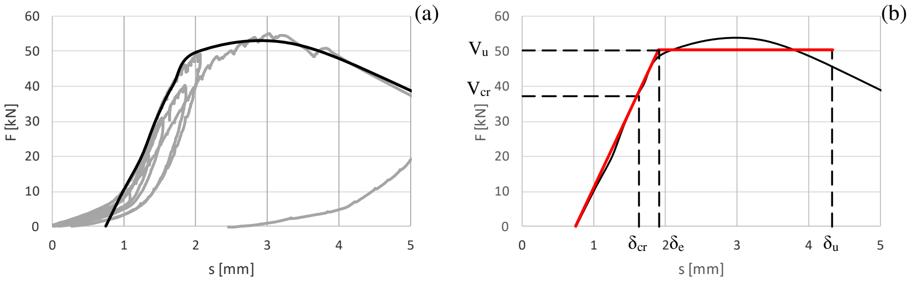

Figure 4.26 Bilinear idealization of the specimen S3: (a) envelope of the top horizontal displacements, (b) bilinear curve.

Table 4.27 Features of the bilinear curve for the specimen S1.

V_{cr}	49.00	kN
δ_{cr}	0.513	mm
k_{el}	95516.57	kN/m
δ_u	1.713	mm
V_u	65.24	kN
δ_e	0.682	mm

Table 4.28 Features of the bilinear curve for the specimen S2.

V_{cr}	35.00	kN
δ_{cr}	0.554	mm
k_{el}	63181.34	kN/m
δ_u	1.105	mm
V_u	52.88	kN
δ_e	0.837	mm

Table 4.29 Features of the bilinear curve for the specimen S3.

V_{cr}	36.40	kN
δ_{cr}	1.642	mm
k_{el}	40820.10	kN/m
δ_u	4.333	mm
V_u	50.26	kN
δ_e	1.914	mm

Following the construction of the bilinear curve, the initial elastic stiffness k_{el} can be determined as defined before. This parameter is a function of the elastic modulus E and the shear modulus G, of the dimensions and of the boundary conditions of the specimen and the extent of cracking. For wall having thickness t, length l and height h, the elastic stiffness is given by the following expression:

$$k_{el} = \frac{1}{\frac{h^3}{\beta \cdot (\alpha EJ)} + \frac{1.2h}{\alpha GA}} \tag{33}$$

where E is the elastic modulus, G is the shear modulus, A is the area of the section of the wall ($t \cdot l$), J is the moment of inertia of the section of the wall ($1/12 \cdot tl^3$), α is the reduction factor accounting for the effect of cracking (assumed equal to 0.37 as specified from Frumento et al., 2009) and β is the boundary condition coefficient that is equal to 12 in the case of double fixed boundary conditions and equal to 3 in the case of cantilever boundary conditions. The shear modulus G is computed assuming a ratio between E and G (for instance $G/E = 0.4$ according to EC6). Once the value of k_{el} is known (e.g. from lateral force tests), the only one unknown is the modulus E, which can be determined by inverting the Eq.(33):

$$E = k_{el} \cdot \left(\frac{h^3}{\beta \alpha J} + \frac{1.2h}{\gamma \alpha A} \right) \tag{34}$$

The elastic moduli of the specimens determined with the Eq.(34) are listed in Table 4.30. The highest value of Young modulus is reached by the specimen S2 (hollow clay bricks 12 cm thick), then the specimens S1 (bricks 20 cm thick) and then the specimen S3 (hollow clay bricks 8 cm thick). The same elastic moduli order, starting from the highest value, was obtained considering the numerical analyses of the in situ tested walls, when their out of plane dynamic behaviour was taken into account. Besides, making a comparison between the walls with homogeneous features, the elastic modulus values obtained statically from the lateral load tests are lower with respect to those dynamically estimated from in situ test results (comparison from S1 and W1-F, S2 and W3-F, S3 and W2-F and/or W3-A). This is due to the fact that the static elastic modulus is calculated from shear-displacement curve obtained from static test in which the displacements are due to both elastic and viscous deformations. The dynamic elastic modulus, instead, is determined considering the initial tangent modulus of the shear-displacement curve of a static test, where the acting forces are low and the displacements are due only to elastic deformations. Obviously, the dynamic values are higher than the static ones.

Table 4.30 Elastic moduli of the specimens determined from the lateral load tests.

Specimen	E [MPa]
S1	2744
S2	2976
S3	2622

4.4.3. Validation of the lateral load test results

Numerical analyses by means of f.e. models of the infill specimens are performed to verify the reliability of the masonry mechanical properties estimated by the interpretation of the lateral load test results. The f.e. models adopted are the same developed for the investigation of the dynamic behaviour and properly adjourned to considered the constraint conditions of the specimens during the lateral load tests. Moreover, the mechanical properties of the masonry are assumed to be the same determined from the shear test results and listed in Table 4.30. The horizontal load is applied in terms of step-wise increased amplitude forces in one direction and, as a results of the numerical analyses, the displacements of the points corresponding at the positions of the transducers in the experimental tests, are monitored.

Figure 4.27 up to Figure 4.29 shows the comparison between the experimental and numerical results in terms of displacements of the monitored points (three displacements in horizontal direction, one at the top, one in half and one at the bottom of the wall, and three displacements in vertical direction, one in the upper right and one in the upper left parts of the walls and one at the bottom right part). In detail, for each monitored point, the numerical displacements, drawn with the black lines, are overlapped over the experimental ones, identified with light grey lines.

As it can be seen, the numerical displacements match very well the experimental ones. In particular, for all specimens the experimental and numerical horizontal displacements at the top and in the middle of the panels are in very good agreement, while those at the bottom show a good agreement only in the first steps of the loading tests. This may be due to the progressive local breakage occurring at the base of the walls (corresponding to the contrast point with the surrounding steel frame) as the horizontal force increases. This phenomenon is not considered by the numerical models developed. As regards the vertical translations it can be noted how, also in this case, the numerical displacements match very well the experimental ones, in particular for the specimens S1 and S3.

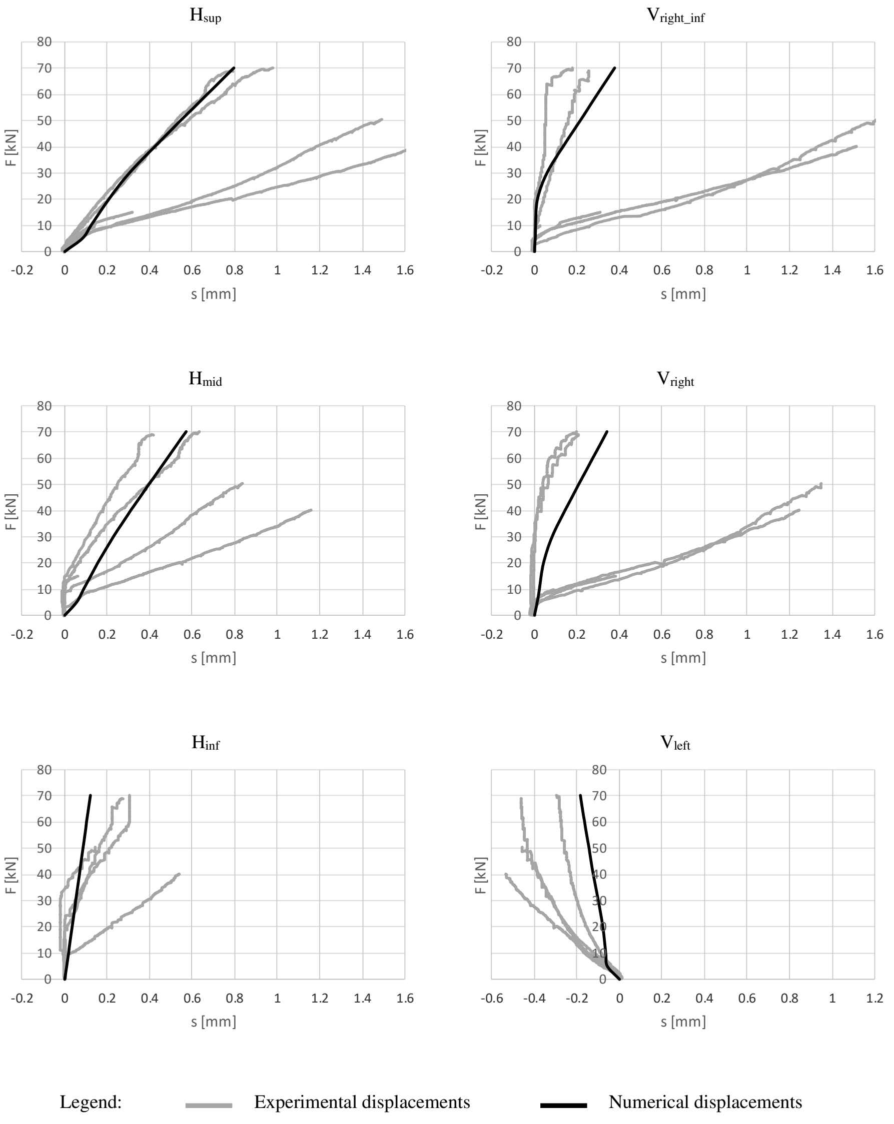

Figure 4.27 Comparison between experimental and numerical lateral load test displacements for the specimen S1.

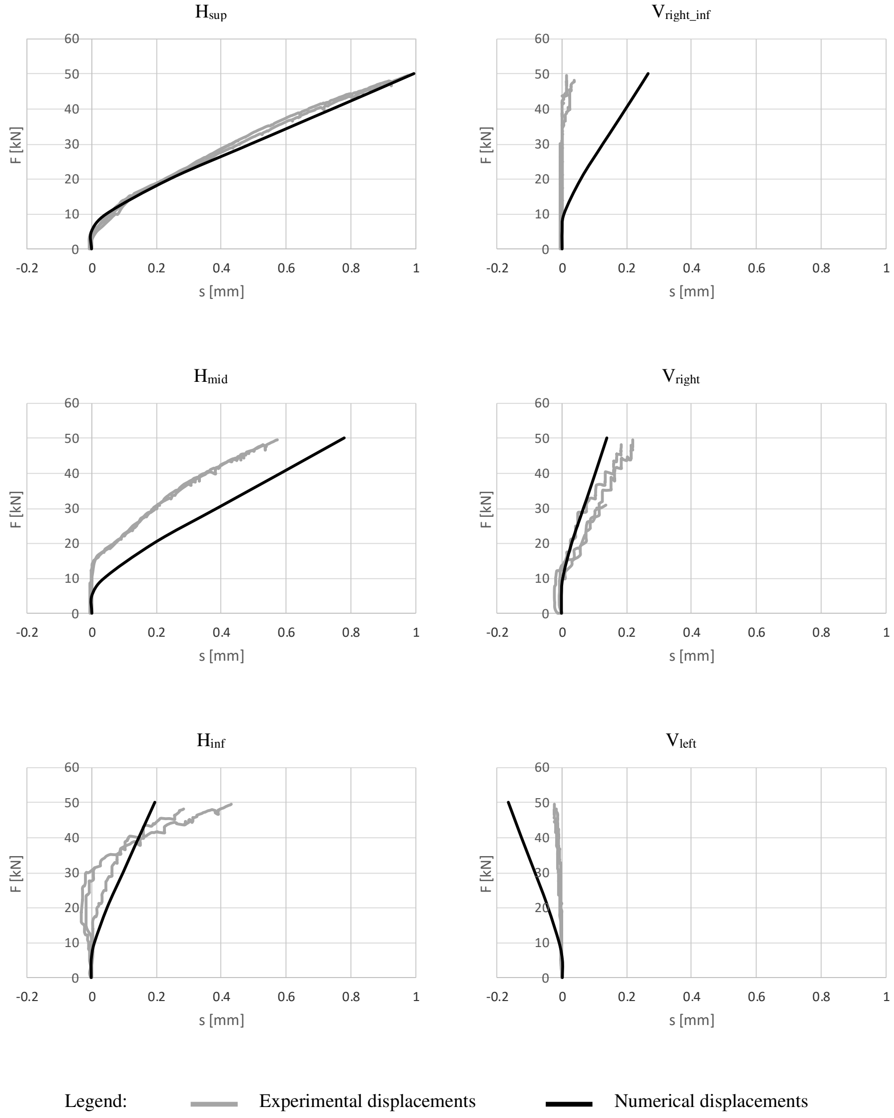

Figure 4.28 Comparison between experimental and numerical lateral load test displacements for the specimen S2.

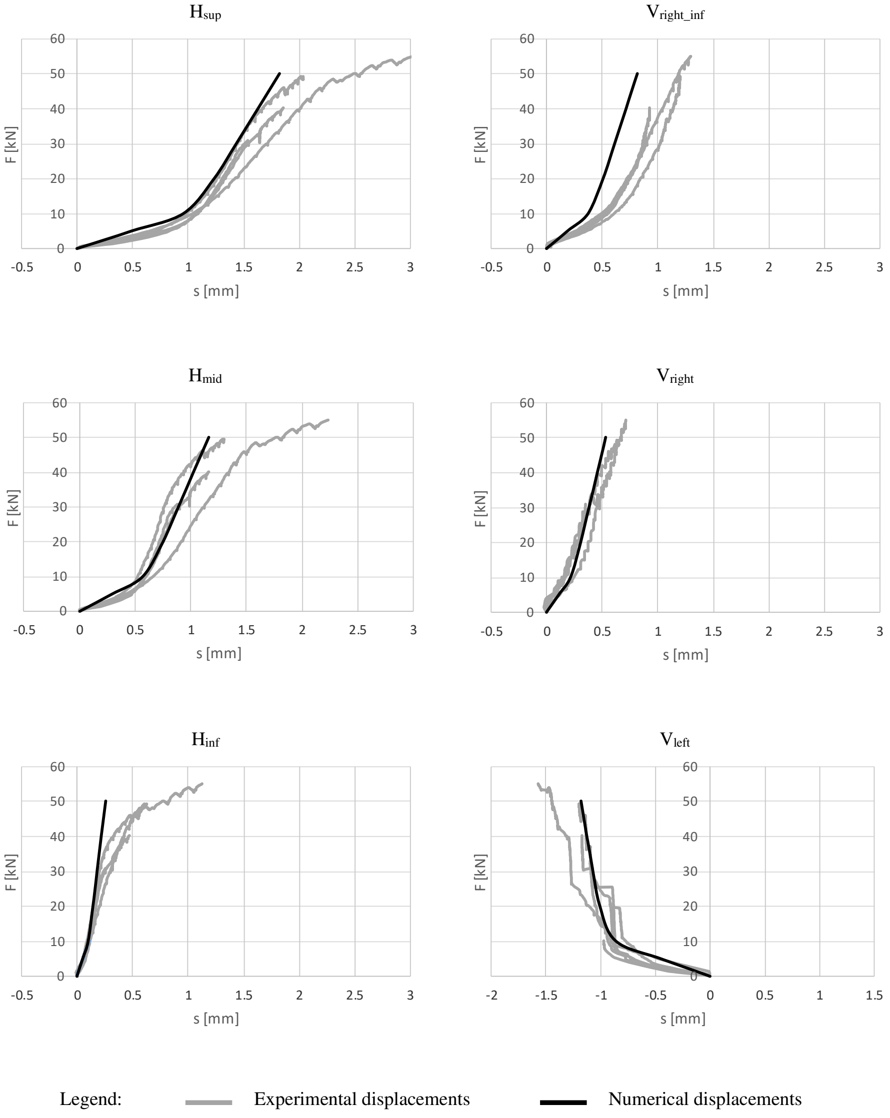

Figure 4.29 Comparison between experimental and numerical lateral load test displacements for the specimen S3.

Conclusions

This thesis dealt with the contribution of the infill masonry walls on the global dynamic behaviour of r.c. frame buildings. The purpose was to examine different methodologies to estimate the mechanical properties of the infills, whose can be used to model these non-structural elements within global f.e. models of buildings. The innovative procedure proposed consists in determining the infill mechanical properties through the results of dynamic impact load tests performed on in situ walls. These tests are fast and non-invasive and can be carried out in all types of non-structural elements, both during the construction and all along the life of a building.

The research activity can be divided in two main parts: the first one concerning the estimation of the infill material properties on the basis of in situ dynamic tests results and the calibration of global f.e. models of the buildings considering the infills. The second part referring to the evaluation of the reliability of the previous results using laboratory test outcomes. For what concerns the in situ experimental investigation, impact load tests with instrumented hammer were performed on homogeneous infill panels to estimate their out of plane dynamic behaviour. From the experimental results obtained and through comparison between the numerical ones achieved by f.e. models, the mechanical properties of the infills were estimated. Afterwards, taking into account two building case studies, the infill masonry walls are modelled within their global f.e. models with the mechanical properties previously obtained from the impact tests. To assess the effectiveness of these complete global f.e. models and to predict the dynamic behaviour of the buildings, the numerical global modal parameters were compared with the experimental ones, obtained by operational modal analyses based on ambient vibration measurements of the buildings. As regards the second part of the research activity, three infill masonry wall specimens were built and tested in the testing Laboratory of Materials and Structures of the Faculty of Engineering at Università Politecnica delle Marche. To evaluate the accuracy of the mechanical infill properties reached by in situ dynamic tests, impact load tests were performed on the specimens. The mechanical properties of these walls were estimated by comparing the dynamic experimental results, in terms of modal parameters, with the numerical ones resulting by f.e. models of them. Furthermore, the material properties determined dynamically are compared with those obtained from the results of classical static tests performed on the specimens (lateral load tests).

For what concerns the results of the impact load tests on in situ infill masonry walls, it can be observed that the stiffness of the walls without plaster, in terms of elastic modulus values, was directly proportional to the thickness of the hollow clay bricks, except for the W1-A wall. This could be due to the fact that the out of plane bending stiffness of the latter wall could be influenced, and in particular reduced, by the notable width of the bed joints and the particular dimensions of the bricks (wider than high). It follows that, in this case, the mechanical properties estimated for the out of plane dynamic behaviour of the panel can be different from those that characterize the in plane dynamic behaviour. After the plaster realization it can be noted that the elastic modulus values were always greater than those reached in the case without plaster, as expected. Furthermore, the tested walls with the same hollow clay brick thickness have very similar elastic modulus values, especially for the case without plaster, so this proves the repetitiveness of the test results. In the case with plaster the differences between the *E* moduli are slightly greater than before, but the mechanical properties of the panels depend also by the typology of the plaster and its thickness, that could be different for each wall.

Considering the global dynamic behaviour of the building case studies, two key stages of the construction process were taken into account: at the end of the construction of the bare building structures and after the construction of the infills. For the first construction key stage, the experimental natural frequencies and mode shapes, obtained by operational modal analysis based on ambient vibration tests, are in very good agreement with the numerical ones obtained with the f.e. models of the bare buildings. Then, the infills were modelled within the global f.e. models and, also in this case, the experimental modal parameters match well the numerical ones. This leads to conclude that the infill mechanical properties estimated by in situ impact test results can be used also to characterize the in plane dynamic behaviour of the walls when included in a global structural model. Moreover, comparing the experimental and numerical modal parameters before and after the infill masonry walls, it is possible to note how the presence of these non-structural elements leads to a significant variation of the buildings modal parameters, especially increasing the natural frequency values.

In the first part of the experimental laboratory campaign, the specimens were tested dynamically by out of plane impact load tests and numerical analyses were performed with the aim to investigate their dynamic behaviour. From the results obtained it was possible to estimate the elastic moduli of the specimen materials. The Young modulus values for the specimen S2 are in good agreement with those obtained from the in situ tests for the walls 12 cm thick called W3-F (in particular in the case with plaster), while for the other specimens the elastic moduli are quite different from those obtained by the in situ tests on the walls with thickness of 8 cm (W2-F and W3-A) and 20 cm (W1-F). Considering the elastic moduli achieved by the results of the dynamic tests on the suspended specimens and making a comparison with those obtained by the in situ tested walls with the same thickness, it is possible to see how the elastic moduli are quite different from each other. Making a judgement between the elastic moduli determined by the out of plane dynamic test results for both simply supported and suspended specimens, it is possible to determine a repetitive correlation between them. In fact, the higher value of elastic modulus is that one obtained for the specimen S2 (hollow clay brick with thickness of 12 cm), then the one for the specimen S3 (hollow clay brick 8 cm thick) and lastly the one relevant to the specimen S1 (hollow clay brick with thickness of 20 cm). After the dynamic tests, in plane lateral load tests on the masonry specimens with plaster, were performed. From the results of these static tests it was possible to estimate the static elastic moduli of the specimen materials and, making a comparison between these moduli with the other ones dynamically estimated, it is possible to observe that the values dynamically estimated are greater than those statically estimated, except for the specimen S1, where the dynamic and static values are very close to each other.

Whereupon, numerical analyses by means of f.e. models of the infill specimens were performed to verify the reliability of the masonry mechanical properties estimated by the interpretation of the lateral load test results. The displacements obtained by the numerical analyses match well those measured during the experimental tests, so this proves the reliability of the elastic moduli estimated from the shear test results.

References

Allemang H. J., Host H. W., Brown D.L. (1983) Multiple input estimation of frequency response functions: excitation consideration. *ASME paper*, No.83-DET-73.

Astroza R., Ebrahimian H., Conte J.P., Restrepo J.I., Hutchinson T.C. (2015) Influence of the construction process and nonstructural components on the modal properties of a five-story building. *Earthquake Engineering and Structural Dynamics*, DOI: 10.1002/eqe.

Avitabile P, Haselton D. (1997) A new procedure for selecting modal testing reference locations. *Sound and Vibration*, 31, 24-29.

Beiraghi H. (2016) Fundamental period of masonry infilled moment-resisting steel frame buildings. *Structural Design of Tall and Special Buildings*, DOI: 10.1002/tal.1342, 1-10.

Biondi S., Colangelo F., Nuti C. (2000) La risposta sismica dei telai con tamponature murarie. *Attività del triennio 1996/98 del Gruppo Nazionale per la Difesa dei Terremoti.*

Bishop R.E.D., Gladwell G.M.L. (1963) An investigation into the theory of the resonance testing. *Philosophical trans. Of the Royal Society of London*, 255A (1055), 241-280.

Bono R.W. et al (1999) New developments in multi-channel test systems. *Proceedings of the 17th International Modal Analysis Conference*, Kissimmee, FL, USA, 518.

Brandt A. (2011) Noise and Vibration Analysis. *Signal Analysis and Experimental Procedures*, Wiley.

Brincker R., Zhang L. (2009) Frequency domain decomposition revisited. *Proc. of the International Operational Modal Analysis Conference* (*IOMAC'09*), 615-626.

Brincker R., Zhang L., Andersen P. (2000) Modal identification of output-only systems using frequency domain decomposition. *Smart Materials and Structures*, Vol.10, No.3, 441-445.

Broch J.T. (1980) *Mechanical vibration and shock measurements*, Bruel & Kjaer.

Calvi G.M., Bolognini D., Penna A. (2004) Seismic performance of masonry – infilled r.c. frames – benefits of slight reinforcements. *Proc. of SISMICA, 6th Congresso National de Sismologia e Engenharia Sismica*, Portugal.

Cantieni R. (2005) Experimental methods used in system identification of civil engineering structures. *Proc. 1st Int. Operational Modal Analysis*, Copenhagen, DK, 249-260.

Cawley P (1986) Rapid measurement of modal properties using FFT analysers with random excitation. *Trans. ASME, Journal of Vibration, Acoustic, Stress and Reliability in Design*, 108, 394-398.

CEN-EN 1996-1-1 (2005) Eurocode 6: Design of masonry structures, Part 1-1: General rules for reinforced and unreinforced masonry structures.

Circolare 2/2/2009 (2009) Istruzioni per l'applicazione delle "Nuove Norme Tecniche per le Costruzioni" di cui al D.M. 14/1/2008, G.U. n.47 del 26/2/2009, suppl. ord. n.27.

Cogger N.D., Webb R.V. (1983) Frequency response analysis. *Technical report 010/83*, Solatron.

Corelli D., Brown D.L. (1984) Impact testing considerations. *Proceeding of the 3rd International Modal Analysis Conference*, Orlando, FL, 735-742.

Crisafulli F.J. (1997) Seismic behavior of reinforced concrete structures with masonry infills. *PhD Thesis*, University of Canterbury, New Zeland.

D.M. 4/1/2008 (2008) Norme Tecniche per le Costruzioni, G.U. n.29 del 4/2/2008, suppl. ord. n.30.

Ewins D.J. (1984) *Modal-testing – theory and practice*. Research studies press. UK.

Ewins D.J., Griffin J. (1981) A state-of-the-art assessment of mobility measurement techniques – results for the mid-range structures. *Journal of sound and vibration*. 78(2), 197-222.

FEMA450. NEHRP Recommended Provisions for Seismic Regulations for New Buildings and Other Structures, *Federal Emergency Management Agency*, Washington (DC).

Frumento S., Magenes G., Morandi P., Calvi G.M. (2009) Interpretation of experimental shear tests on clay brick masonry walls and evaluation of q-factors for seismic design. *Research report No.02*.09. Eucentre and University of Pavia.

Furtado A., Rodrigues H., Arede A., Varum H. (2017) Modal identification of infill masonry walls with different characteristics. *Engineering Structures*, 145, 118-134.

Giacchetti R., Bufarini S., D'Aria V. (2005) Il controllo strutturale degli edifici in cemento armato e in muratura. *EPC Libri*.

Halvorsen W.G., Brown D.L. (1997) Impulse technique for structural frequency response. *Journal of sound and vibration*, November, 8-21.

Harris C.M. (1995) *Shock and vibration handbook*. McGraw-Hill, ISBN 0-07-026920-3.

Hatzigeorgiou G.D., Kanapitsas G. (2013) Evaluation of fundamental period of low-rise and mid-rise reinforced concrete buildings. *Journal of Earthquake Engineering and Structural Dynamics*, Vol.42(11), 1599.

He J., Fu Z. F. (2001) Modal analysis. *Butterworth-Heinemann*, Oxford.

Hencky H. (1947) Uber die berucksichtigung der schubverzerrungen in ebenen plattern. *Ing. Arch. 16*, 72-76.

James G.H., Carne T.G., Lauffer J.P. (1995) The natural excitation technique (NExT) for modal parameter extraction from operating structures. *The International Journal of Analytical and Experimental Modal Analysis*, Vol.10, No.4, 260-277.

Juang J.N. (1994) Applied System Identification. *Prentice-Hall Englewood Cliffs*, New Jersey, USA.

Koken (2003) A theoretical and experimental investigation of the behavior of the multi-storey and multi-bay infilled steel frames under reversed cycling horizontal loading. *Ph.D. Thesis*, Konya, Selkuk University.

Kromm A. (1955) Uber die randquerklafe bei gestuzten plattem. *Zamm 35*, 231-242.

Lekhnitskii S.G. (1968) Anisotropic plates. *Gordon and Breach*, New York.

Magenes G., Morandi P. (2008) Proposals for the evaluation of the q-factor from cyclic test results on masonry walls. *ESECMaSE project*, University of Pavia and Eucentre.

Menditto G. (2002) Lezioni di scienza delle costruzioni – Volume 3, Parte 2: Strutture bidimensionali piane. *Pitagora editrice*, Bologna.

Mindlin R.D. (1951) Influence of rotatory inertia and shear on flexural motions of isotropic, elastic plates. *J. Appl. Mech.*, vol.18, 31-38.

ModalVIEW version R2 (2012/2013) Application for modal testing and analysis. *ABSignal Inc.*

Morandi P., Hak S., Magenes G. (2011) Comportamento sismico delle tamponature in laterizio in telai in c.a.: definizione dei livelli prestazionali e calibrazione di un modello numerico. *Proc. of ANIDIS 2011*, Bari.

Ozkaynak H., Yuksel E., Yalcin C. (2014) Masonry infill walls in reinforced concrete frames as a source of structural damping. Journal of *Earthquake Engineering and Structural Dynamics*, Vol.43, 949-968.

Panc V. (1975) Theories of elastic plates. *Leyden Noordhoff International Publishing*.

Popovics J.S., Zemajtis J., Shkolnik I. (2008) A study of static and dynamic modulus of elasticity of concrete. *ACI-CRC Final report*, University of Illinois, Urbana, IL.

Reissner E. (1944) On the theory of bending of elastic plates. *J Math Phys*, vol. 23, 184-191.

Reissner E. (1945) The effect of transverse shear deformation on the bending of elastic plates. *J Appl Mech*, vol. 12, A69-A77.

Reissner E. (1975) On transverse bending of plates, including effect of transverse shear deformation. *Journal of solids and structures*, vol.11, 569-573.

Reissner E. (1976) On the theory of transverse bending of elastic plates. *International journal of solids and structures*, vol.12, 545-554.

SAP2000 advanced v14.1.0 (2009) Static and dynamic finite element analysis of structures. *CSI Computer and Structure Inc.* Berkeley.

Stavridis A., Koutromanos I., Shing P.B. (2012) Shake-table tests of three-story reinforced concrete frame with masonry infill walls. *Journal of Earthquake Engineering and Structural Dynamics*, Vol.41, 1089-1108.

UNI-EN-12504-4 (2004) Testing concrete, Part 4: Determination of ultrasonic pulse velocity.

Van Overshee P., De Moor B. (1996) Subspace identification for linear systems: theory-implementation-application. *The Netherlands: Kluwer Academic Publishers*, Dordrecht.

Vasil'ev V.V. (1998) Classical theory of plates: historical perspective and state-of-the-art. *Mechanics of Solids*, vol.33, No.3, 35-45.

Wang C.M., Lim G.T., Lee K.H. (1999) Relationship between Kirchhoff and Mindlin bending solution for Levi plates. *J. Appl. Mech.*, 66, 541-5.

Wang C.M., Reddy I.N., Lee L.H. (2000) Shear deformable beams and plates: relationships with classical solutions. *Elsevier*, Oxford.

Wang W., Shi M.X. (1977) Thick plate theory based on general solutions of elasticity. *Acta mechanica*, 123, 27-36.

Zihlin P.A. (1992) On Poisson's and Kirchhoff's theories of plates from the point of view of the modern theory of plates. *Mechanics of Solids*, No.3, 65-72.

Appendix A.

Fundamentals of plates theory

A.1. Thin isotropic plates

A.1.1. Introduction

Thin plates are initially flat structural members bounded by two parallel planes, called faces, and a cylindrical surface, called edge or boundary. The generators of the cylindrical surface are perpendicular to the plane faces. The distance between the plane faces is called the thickness (h) of the plate. It will be assumed that the plate thickness is small compared with other characteristic dimensions of the faces (length, width, diameter, etc.). Geometrically, plates are bounded either by straight or curved boundaries (Figure A.1). The static or dynamic loads carried by plates are predominantly perpendicular to the plate faces. It is common to divide the thickness h into equal halves by a plane parallel to its faces. This plane is called the *middle plane* (or simply, the *midplane*) of the plate (Figure A.2).

Being subjected to transverse loads, an initially flat plate deforms and the midplane passes into some curvilinear surface, which is referred to as the *middle surface*. In this thesis we will consider only plates of constant thickness. For such plates, the shape of a plate is adequately defined by describing the geometry of its middle plane. A plate resists transverse loads by means of bending, exclusively. The flexural properties of a plate depend greatly upon its thickness in comparison with other dimensions. Plates may be classified into three groups according to the ratio a/h, where a is a typical dimension of a plate in a plane and h is a plate thickness. These groups are:

1. *thick plates* having ratios $a/h \leq 8\ldots10$. The analysis of such bodies includes all the components of stresses, strains and displacements as for solid bodies using the general equations of three-dimensional elasticity;
2. *membranes* with ratios $a/h \geq 80\ldots100$ and they are devoid of flexural rigidity. Membranes carry the lateral loads by axial tensile forces N (and shear forces) acting in the plate middle surface, called *membrane forces*; they produce projection on a vertical axis and thus balance a lateral load applied to the plate-membrane;

3. *thin plates* with 8…10 ≤ *a/h* ≤ 80…100. Depending on the value of the ratio *w/h*, the ratio of the maximum deflection of the plate to its thickness, the part of flexural and membrane forces here may be different. Therefore, this group, in turn, may also be subdivided into two different classes.
    a. *Stiff plates* with *w/h* ≤ 0.2. This plates are flexural rigid thin plates. They carry loads two dimensionally, mostly by internal bending and twisting moments and by transverse shear forces. The middle plane deformations and the membrane forces are negligible. A fundamental feature of stiff plates is that the equations of static equilibrium for a plate element may be set up for an original (undeformed) configuration of the plate.
    b. *Flexible plates.* If the plate deflections are beyond a certain level, *w/h* ≤ 0.3, then, the lateral deflections will be accompanied by stretching of the middle surface. Such plates are referred to as flexible plates. These plates represent a combination of stiff plates and membranes and carry external loads by the combined action of internal moments, shear forces, and membrane (axial) forces. When the magnitude of the maximum deflection is considerably greater than the plate thickness, the membrane actions predominates. So, if *w/h* > 5, the flexural stress can be neglected compared with the membrane stress. Consequently, the load-carrying mechanism of such plates becomes of the membrane type, i.e., the stress is uniformly distributed over the plate thickness.

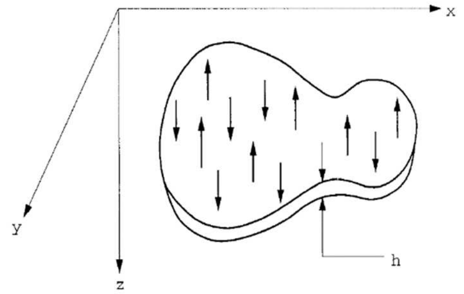

Figure A.1 General plate element.

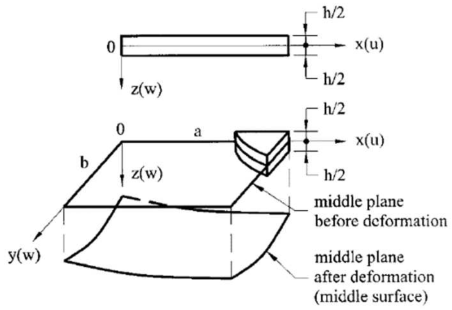

Figure A.2 Features of the middle plane.

A.1.2. General behaviour of plates

Consider a load-free plate shown in Figure A.3, in which the *xy* plane coincides with the plate's midplane and the z coordinate is perpendicular to it and is directed downwards. The fundamental assumptions of the linear, elastic, small-deflection theory of bending for thin plates may be stated as follows:

1. the material of the plate is elastic, homogeneous and isotropic;
2. the plate is initially flat;
3. the deflection (the normal component of the displacement vector) of the midplane is small compared with the thickness of the plate. The slope of the deflect surface is therefore very small and the square of the slope is a negligible quantity in comparison with unity;
4. the straight lines, initially normal to the middle plane before bending, remain straight and normal to the middle surface during the deformation and the length of such elements is not altered. This means that the vertical shear strains γ_{xz} and γ_{yz} are negligible and the normal strain ε_z may also be omitted. This assumption is referred to as the *hypothesis of straight normal*;
5. the stress normal to the middle plane σ_z is small compared with the other stress components and may be neglected in the stress-strain relations;
6. since the displacements of a plate are small, it is assumed that the middle surface remains unstrained after bending.

These assumptions, known as Kirchhoff hypothesis, result in the reduction of a three-dimensional plate problem to a two-dimensional one. Consequently, the governing plate equation can be derived in a concise and straightforward manner. The plate bending theory based on the above assumptions is referred to as the *classical* or *Kirchhoff's plate theory*.

A.1.3. Survey of elasticity theory

The classical theories of plates and shells are an important application of the theory of elasticity, which deals with relationship of forces, displacements, stresses and strains in an elastic body. When a solid body is subjected to external forces, it deforms, producing internal strains and stresses. The deformation depends on the geometrical configuration of the body, on applied loading, and on the mechanical properties of its material. In the theory of elasticity we restrict our attention to linear elastic materials; i.e., the relationships between stress and strain are linear and the deformations and stresses disappear when the external forces are removed. The classical theory of elasticity assumes the material is homogeneous and isotropic, i.e., its mechanical properties are the same in all directions and at all points.

Consider an elastic body of any general shape subjected to external loads which are in equilibrium. Then, consider a material point anywhere in the interior of the body. If we assign a Cartesian coordinate frame with the axes x, y, and z, as shown in Figure A.3, it is convenient to assign an infinitesimal element in the form of parallelepiped (dx, dy, dz), with faces parallel to the coordinate planes. Stresses acting on the faces of this element describe the intensity of the internal forces at a point on a particular face. These stresses can be broken down into a normal component (*normal stress*) and tangent component (*shear stress*) to the particular face. As a result, the three stress components, denoted by σ_{xx}, τ_{xy}, τ_{xz}, …, will act on each face of the element. The subscript notation for the stress components is interpreted as follows: the first subscript indicates the direction of an outer normal to the face on which the stress component acts; the second subscript relates to the direction of the stress itself.

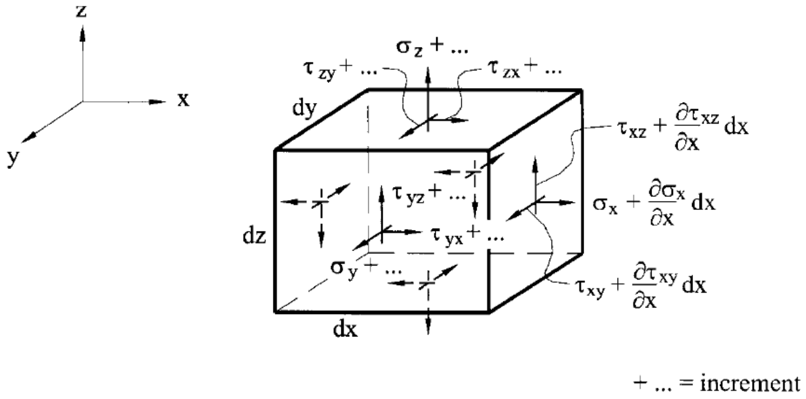

Figure A.3 Infinitesimal element in the form of parallelepiped.

The following sign convention will be adapted for the stress components: the positive sign for the normal stress will correspond to a tensile stress, while the negative sign will correspond to a compressive stress. The sign agreement for the shear stresses follows from the relationship between the direction of an outer normal drawn to a particular face and the direction of the shear stress component on the same face. If both the outer normal and the shear stress are either in positive or negative directions relative to the coordinate axes, then the shear stress is positive. If the outer normal points in a positive direction while the stress in a negative direction (or vice versa), the shear stress is negative. On this basis, all the stress components shown in Figure A.3 are positive. On any one face these three stress components comprise a vector, called a surface traction. The above-mentioned set of the stress components acting on the faces of the element forms the stress tensor, T_s, i.e.,

$$Ts = \begin{pmatrix} \sigma_x & \tau_{xy} & \tau_{xz} \\ \tau_{yx} & \sigma_y & \tau_{yz} \\ \tau_{zx} & \tau_{zy} & \sigma_z \end{pmatrix} \tag{35}$$

which is symmetric with respect to the principal diagonal because of the reciprocity law of shear stresses, i.e.,

$$\tau_{xy} = \tau_{yx}; \tau_{xz} = \tau_{zx}; \tau_{yz} = \tau_{zy}. \tag{36}$$

Thus, only the six stress components out of nine in the stress tensor (Eq. (35)) are independent. The stress tensor, T_s, completely characterizes the three-dimensional state of stress at a point of interest. For elastic stress analysis of plates, the two-dimensional state of stress is of special importance. In this case, $\sigma_z = \tau_{yz} = \tau_{xz} = 0$; thus the two-dimensional stress tensor has a form:

$$T_s = \begin{pmatrix} \sigma_x & \tau_{xy} \\ \tau_{yx} & \sigma_y \end{pmatrix}, \text{ where } \tau_{xy} = \tau_{yx} \qquad (37)$$

Assume that the elastic body shown in Figure A.4 is supported in such a way that rigid body displacements (translations and rotations) are prevented. Thus, this body deforms under the action of external forces and each of its points has small elastic displacements. For example, a point *M* had the coordinates *x*, *y*, and *z* in initial undeformed state. After deformation, this point moved into position *M'* and its coordinates became the following $x' = x + u$, $y' = y + v$, $z' = z + w$, where *u*, *v*, and *w* are projections of the displacement vector of point *M*, vector ***MM'***, on the coordinates axes *x*, *y*, and *z*. In the general case, *u*, *v*, and *w* are functions of *x*, *y*, and *z*. Again, consider an infinitesimal element in the form of parallelepiped enclosing point of interest *M*. Assuming that a deformation of this parallelepiped is small, we can represent it in the form of the six simplest deformations sown in Figure A.4.

The first three deformations shown in Figure A.5a, b and c define the elongation (or contraction) of edges of the parallelepiped in the direction of the coordinate axes.

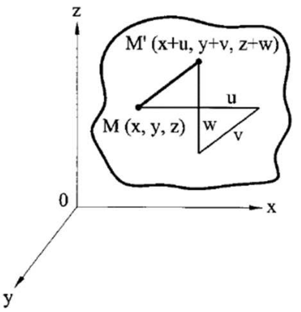

Figure A.4 Deformation of the elastic body.

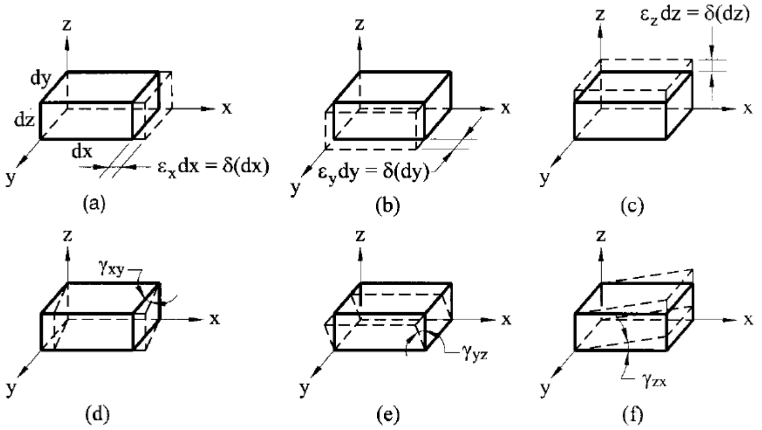

Figure A.5 Deformation of the infinitesimal element.

They can be defined as

$$\varepsilon_x = \frac{\delta(dx)}{dx}, \varepsilon_y = \frac{\delta(dy)}{dy}, \varepsilon_z = \frac{\delta(dz)}{dz} \tag{38}$$

and they are called the *normal* or *linear strains*. In Eq. (38) the increments δdx can be expressed by the second term in the Taylor series, i.e., δdx = ($\partial u/\partial x$)dx, etc.; thus, we can write

$$\varepsilon_x = \frac{\delta(dx)}{dx}, \varepsilon_y = \frac{\delta(dy)}{dy}, \varepsilon_z = \frac{\delta(dz)}{dz} \tag{39}$$

The three other deformations shown in Figure A.5d, e and f are referred to as shear strains because they define a distortion of an initially right angle between the edges of the parallelepiped. They are denoted by γ_{xy}, γ_{xz} and γ_{yz}. The subscripts indicate the coordinate planes in which the shear strains occur. Let us determine, for examples, the shear strain in the *xy* coordinate plane. Consider the projection of the parallelepiped, shown in Figure A.5d, on this coordinate plane. Figure A.6 shows this projection in the form of the rectangle before deformation (*ABCD*) and after deformation (*A'B'C'D'*). The angle *BAD* in Figure A.6 deforms to the angle *B'A'D'*, the deformation being the angle $\gamma' + \gamma''$. Thus, the shear strain is

$$\gamma_{xy} = \gamma' + \gamma'' \tag{40}$$

or it can be determined in terms of the in-plane displacements, *u* and *v*, as follows

$$\gamma_{xy} = \frac{\frac{\partial v}{\partial x}dx}{dx + \frac{\partial u}{\partial x}dx} + \frac{\frac{\partial u}{\partial y}dy}{dy + \frac{\partial v}{\partial y}dy} = \frac{\frac{\partial v}{\partial x}}{1 + \frac{\partial u}{\partial x}} + \frac{\frac{\partial u}{\partial y}}{1 + \frac{\partial v}{\partial y}} \tag{41}$$

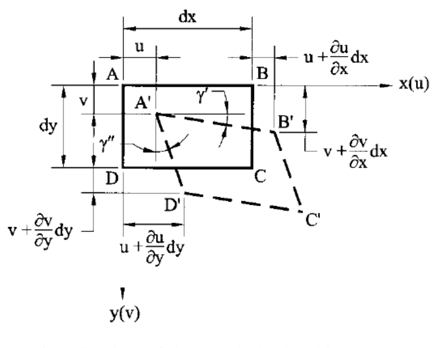

Figure A.6 Projection of the parallelepiped in plane coordinates.

Since we have confined ourselves to the case of very small deformations, we may omit the quantities $\partial u/\partial x$ and $\partial v/\partial y$ in the denominator of the last expression, as being negligibly small compared with unity. Finally, we obtain

$$\gamma_{xy} = \frac{\partial v}{\partial x} + \frac{\partial u}{\partial y} \tag{42}$$

Similarly, we can obtain γ_{xz} and γ_{yz}.. Thus, the shear strains are given by

$$\gamma_{xy} = \frac{\partial u}{\partial y} + \frac{\partial v}{\partial x}; \gamma_{xz} = \frac{\partial u}{\partial z} + \frac{\partial w}{\partial x}; \gamma_{yz} = \frac{\partial v}{\partial z} + \frac{\partial w}{\partial y} \tag{43}$$

Similar to the stress tensor at a given point, we can define a strain tensor as

$$T_D = \begin{pmatrix} \varepsilon_x & \frac{1}{2}\gamma_{xy} & \frac{1}{2}\gamma_{xz} \\ \frac{1}{2}\gamma_{yx} & \varepsilon_y & \frac{1}{2}\gamma_{yz} \\ \frac{1}{2}\gamma_{zx} & \frac{1}{2}\gamma_{zy} & \varepsilon_z \end{pmatrix} \tag{44}$$

It is evident that the strain tensor is also symmetric because of

$$\gamma_{xy} = \gamma_{yx}; \gamma_{xz} = \gamma_{zx}; \gamma_{yz} = \gamma_{zy} \tag{45}$$

The constitutive equations relate the stress components to strain components. For the linear elastic range, these equations represent the generalized Hooke's law. In the case of a three-dimensional isotropic body, the constitutive equations are given by

$$\varepsilon_x = \frac{1}{E}\left[\sigma_x - \nu(\sigma_y + \sigma_z\right], \varepsilon_y = \frac{1}{E}\left[\sigma_y - \nu(\sigma_x + \sigma_z\right], \varepsilon_z = \frac{1}{E}\left[\sigma_z - \nu(\sigma_y + \sigma_x\right], \tag{46}$$

$$\gamma_{xy} = \frac{1}{G}\tau_{xy}, \gamma_{xz} = \frac{1}{G}\tau_{xz}, \gamma_{yz} = \frac{1}{G}\tau_{yz}, \tag{47}$$

where E, v, and G are the modulus of elasticity, Poisson's ratio and the shear modulus, respectively. The following relationship exists between E and G

$$G = \frac{E}{2(1+\upsilon)} \tag{48}$$

The stress components introduce previously must satisfy the following differential equations of equilibrium

$$\frac{\partial \sigma_x}{\partial x}+\frac{\partial \tau_{xy}}{\partial y}+\frac{\partial \tau_{xz}}{\partial z}+F_x=0$$

$$\frac{\partial \sigma_y}{\partial y}+\frac{\partial \tau_{yx}}{\partial x}+\frac{\partial \tau_{yz}}{\partial z}+F_y=0 \tag{49}$$

$$\frac{\partial \sigma_z}{\partial z}+\frac{\partial \tau_{zx}}{\partial x}+\frac{\partial \tau_{zy}}{\partial y}+F_z=0$$

where F_x, F_y and F_z are the body forces (e.g., gravitational, magnetic forces). In deriving these equations, the reciprocity of the shear stresses, Eq. (45), has been used.

Since the three equations (49) for six unknowns are not sufficient to obtain a solution, three-dimensional stress problems of elasticity are internally statically indeterminate. Additional equations are obtained to express the continuity of a body. These additional equations are referred to as *compatibly equations*. In Eq. (39) and Eq. (43) we have related the six strain components to the three displacement components. Eliminating the displacement components by successive differentiation, the following compatibly equations are obtained

$$\frac{\partial^2 \varepsilon_x}{\partial y^2}+\frac{\partial^2 \varepsilon_y}{\partial x^2}=\frac{\partial^2 \gamma_{xy}}{\partial x \partial y}$$

$$\frac{\partial^2 \varepsilon_y}{\partial z^2}+\frac{\partial^2 \varepsilon_z}{\partial y^2}=\frac{\partial^2 \gamma_{yz}}{\partial y \partial z} \tag{50}$$

$$\frac{\partial^2 \varepsilon_z}{\partial x^2}+\frac{\partial^2 \varepsilon_x}{\partial z^2}=\frac{\partial^2 \gamma_{xz}}{\partial x \partial z}$$

$$\frac{\partial}{\partial z}\left[\frac{\partial \gamma_{yz}}{\partial x}+\frac{\partial \gamma_{xz}}{\partial y}-\frac{\partial \gamma_{xy}}{\partial z}\right]=2\frac{\partial^2 \varepsilon_z}{\partial x \partial y}$$

$$\frac{\partial}{\partial x}\left[\frac{\partial \gamma_{xz}}{\partial y}+\frac{\partial \gamma_{xy}}{\partial z}-\frac{\partial \gamma_{yz}}{\partial x}\right]=2\frac{\partial^2 \varepsilon_x}{\partial y \partial z} \tag{51}$$

$$\frac{\partial}{\partial y}\left[\frac{\partial \gamma_{xy}}{\partial z}+\frac{\partial \gamma_{yz}}{\partial x}-\frac{\partial \gamma_{xz}}{\partial y}\right]=2\frac{\partial^2 \varepsilon_y}{\partial x \partial z}$$

For a two-dimensional state of stress ($\sigma_z = 0$, $\tau_{xz} = \tau_{yz}\ 0$), the equilibrium conditions (Eq. (49)) become

$$\begin{aligned} &\frac{\partial \sigma_x}{\partial x} + \frac{\partial \tau_{xy}}{\partial y} + F_x = 0 \\ &\frac{\partial \sigma_y}{\partial y} + \frac{\partial \tau_{yx}}{\partial x} + F_y = 0 \end{aligned} \qquad (52)$$

and the compatibility equation is

$$\frac{\partial^2 \varepsilon_x}{\partial y^2} + \frac{\partial^2 \varepsilon_y}{\partial x^2} = \frac{\partial^2 \gamma_{xy}}{\partial x \partial y} \qquad (\gamma_{xz} = \gamma_{yz} = \varepsilon_z = 0) \qquad (53)$$

We can rewrite the Eq. (53) in terms of the stress components as follows

$$\left(\frac{\partial^2}{\partial x^2} + \frac{\partial^2}{\partial y^2} \right) \left(\sigma_x + \sigma_y \right) = 0. \qquad (54)$$

This equation is called Levy's equation. By introducing Airy's stress function $\Phi(x, y)$ which satisfies

$$\sigma_x = \frac{\partial^2 \Phi}{\partial y^2}, \sigma_y = \frac{\partial^2 \Phi}{\partial x^2}, \tau_{xy} = -\frac{\partial^2 \Phi}{\partial x \partial y} \qquad (55)$$

Eq. (54) becomes

$$\nabla^2 \nabla^2 \Phi = 0 \qquad (56)$$

where

$$\nabla^2 \equiv \frac{\partial^2}{\partial x^2} + \frac{\partial^2}{\partial y^2} \qquad (57)$$

is the two-dimensional Laplace operator.

Summarizing, for an elastic solid there are fifteen independent variables: six stress components, six strain components and three displacements. In the case where the compatibility is satisfied, there are fifteen equations: three equilibrium equations, six constitutive relations and six strain-displacements equations.

A.1.4. Small-deflection plate bending theory

Let u, v, and w be components of the displacement vector of points in the middle surface of the plate occurring in the x, y and z directions, respectively. The normal component of the displacement vector, w (called the *deflection*) and the lateral distributed load p are positive in the downward direction. As it follows from the assumption (4) previously mentioned

$$\varepsilon_z = 0, \qquad \gamma_{yz} = 0, \qquad \gamma_{xz} = 0. \tag{58}$$

Integrating the expressions (39) and (43) for ε_z, γ_{yz} and γ_{xz} and taking into account Eq. (58), we obtain

$$w^{(z)} = w(x,y), \qquad u^{(z)} = -z\frac{\partial w}{\partial x} + u(x,y), \qquad v^{(z)} = -z\frac{\partial w}{\partial y} + v(x,y) \tag{59}$$

where $u^{(z)}$, $v^{(z)}$ and $w^{(z)}$ are displacements of points at the distance z from the middle surface. Based upon assumption (6), we conclude that $u = v = 0$. Thus, Eq. (59) have the following form in the context of Kirchhoff's theory

$$w^{(z)} = w(x,y), \qquad u^{(z)} = -z\frac{\partial w}{\partial x}, \qquad v^{(z)} = -z\frac{\partial w}{\partial y} \tag{60}$$

As it follows from the above, the displacements $u^{(z)}$ and $v^{(z)}$ of an arbitrary horizontal layer vary linearly over a plate thickness while the deflection does not vary over the thickness. Figure A.7 shows a section of the plate by a plane parallel to Oxz,y = const., before and after deformation. Consider a segment AB in the positive z direction. We focus on an arbitrary point B which initially lies at a distance z from the undeformed middle plane (from the point A). During the deformation, point A displaces a distance w parallel to the original z direction to point A_1. Since the transverse shear deformations are neglected, the deformed position of point B must lie on the normal to the deformed middle plane erected at point A_1 (assumption (4)). Its final position is denoted by B_1. Due to the assumptions (4) and (5), the distance z between the abovementioned points during deformation remains unchanged and is also equal to z. We can also represent the displacement components $u^{(z)}$ and $v^{(z)}$, Eq. (59), in the form

$$u^{(z)} = -z\vartheta_x, \qquad v^{(z)} = -z\vartheta_y \tag{61}$$

where

$$\vartheta_x = \frac{\partial w}{\partial x}, \qquad \vartheta_y = \frac{\partial w}{\partial y} \tag{62}$$

are the angles of rotation of the normal (normal I-I in Figure A.7) to the middle surface in the *Oxz* and *Oyz* plane, respectively. Owing to the assumption (4), ϑ_x and ϑ_y are also slopes of the tangents to the traces of the middle surface in the abovementioned planes.

Substitution of Eq.(60) into the first two Eq. (39) and into the first Eq. (43), yields

$$\varepsilon_x^z = -z\frac{\partial^2 w}{\partial x^2}, \qquad \varepsilon_y^z = -z\frac{\partial^2 w}{\partial y^2}, \qquad \gamma_{xy}^z = -2z\frac{\partial^2 w}{\partial x \partial y} \tag{63}$$

where the superscript *z* refers to the in-plane strain components at a point of the plate located at a distance *z* from the middle surface. Since the middle surface deformations are neglected due to the assumptions (6), from here on, this superscript will be omitted for all the strain and stress components at points across the plate thickness. The second derivatives of the deflection on the right-hand side of Eq. (63) have a certain geometrical meaning. Let a section *MNP* represent some plane curve in which the middle surface of the deflected plate is intersected by a plane y = const. (Figure A.8). Due to the assumption (3), this curve is shallow and the square of the slope angle may be regarded as negligible compared with unity, i.e., $(\partial w/\partial x)^2 << 1$.

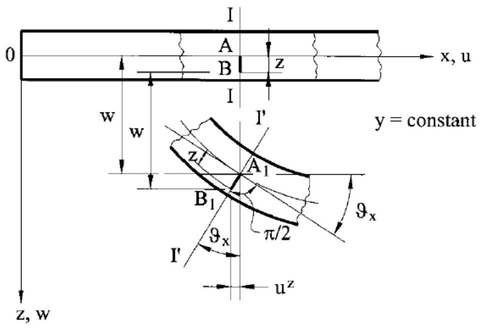

Figure A.7 Section of the plate before and after deformation.

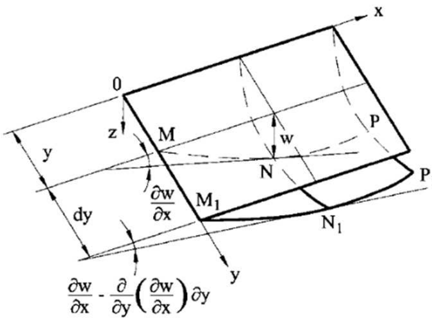

Figure A.8 Middle surface of the deflected plate intersected by a plane y = const.

Then, the second derivative of the deflection, $\partial^2 w/\partial x^2$ will define approximately the curvature of the section along the x axis, χ_x. Similarly, $\partial^2 w/\partial y^2$ defines the curvature of the middle surface χ_y along the y axis. The curvatures χ_x and χ_y characterize the phenomenon of bending of the middle surface in planes parallel to the Oxz and Oyz coordinate planes, respectively. They are referred to as bending curvature and are defined by

$$\chi_x = \frac{1}{\rho_x} = -\frac{\partial^2 w}{\partial x^2}, \qquad \chi_y = \frac{1}{\rho_y} = -\frac{\partial^2 w}{\partial y^2} \tag{64}$$

We consider a bending curvature positive if it is convex downward, i.e., in the positive direction of the z axis. The negative sign is taken in Eq. (64) since, for example, for the deflection convex downward curve MNP (Figure A.8), the second derivative, $\partial^2 w/\partial x^2$ is negative. The curvature $\partial^2 w/\partial x^2$ can be also defined as the rate of change of the angle $\vartheta_x = \partial w/\partial x$ with respect to distance x along this curve. However, the above angle can vary in the y direction also. It is seen from comparison of the curves MNP and $M_1N_1P_1$ (Figure A.8), separated by a distance dy. If the slope for the curve MNP is $\partial w/\partial x$ then for the curve $M_1N_1P_1$ this angle becomes equal to $\left[\frac{\partial w}{\partial x} - \frac{\partial}{\partial y}\left(\frac{\partial w}{\partial x}\right)dy\right]$ or $\left(\frac{\partial w}{\partial x} - \frac{\partial^2 w}{\partial x \partial y}dy\right)$. The rate of change of the angle $\partial w/\partial x$ per unit length will be $(-\partial^2 w/\partial x\partial y)$. The negative sign is taken here because it is assumed that when y increases, the slope angle of the tangent to the curve decreases (by analogy with the sign convention for the bending curvatures χ_x and χ_y). Similarly, can be convinced that in the perpendicular section (for the variable x), the rate of change of the angle $\partial w/\partial y$ is characterized by the same mixed derivative $(-\partial^2 w/\partial x\partial y)$. By analogy with the torsion theory of rods, the derivative $\partial^2 w/\partial x\partial y$ defines the warping of the middle surface at a point with coordinates x and y is called the twisting curvature with respect to the x and y axes and is denoted by χ_{xy}. Thus

$$\chi_{xy} = \chi_{yx} = \frac{1}{\rho_{xy}} = -\frac{\partial^2 w}{\partial x \partial y} \tag{65}$$

Taking into account Eq. (64) and (65) we can rewrite Eq. (63) as follows

$$\varepsilon_x = z\chi_x, \qquad \varepsilon_y = z\chi_y, \qquad \gamma_{xy} = 2z\chi_{xy} \tag{66}$$

In the case of a three-dimensional state of stress, stress and strain are related by the Eq. (46) and (47) of the generalized Hooke's law. From a mathematical standpoint, this means that the three new equations (58) are added to the system of governing equations of the theory of elasticity. So, the latter becomes overdeterminated and, therefore, it is necessary to also drop three equations. As a result, the three relations out of six of Hooke's law for strain (58) are discarded. Moreover, the normal stress component $\sigma_z = 0$. Solving Eq. (46) and (47) for stress component σ_x, σ_y and τ_{xy} yields

$$\sigma_x = \frac{E}{1-\nu^2}\left(\varepsilon_x + \nu\varepsilon_y\right), \qquad \sigma_y = \frac{E}{1-\nu^2}\left(\varepsilon_y + \nu\varepsilon_x\right), \qquad \tau_{xy} = G\gamma_{xy} \tag{67}$$

The stress components are shown in Figure A.9a. Introducing the plate curvatures, Eq. (64) and (65) and using Eq. (66), the above equations appear as follows:

$$\begin{aligned}
\sigma_x &= \frac{Ez}{1-\nu^2}\left(\chi_x + \nu\chi_y\right) = -\frac{Ez}{1-\nu^2}\left(\frac{\partial^2 w}{\partial x^2} + \nu\frac{\partial^2 w}{\partial y^2}\right)\\
\sigma_y &= \frac{Ez}{1-\nu^2}\left(\chi_y + \nu\chi_x\right) = -\frac{Ez}{1-\nu^2}\left(\frac{\partial^2 w}{\partial y^2} + \nu\frac{\partial^2 w}{\partial x^2}\right)\\
\tau_{xy} &= \frac{Ez}{1+\nu}\chi_{xy} = -\frac{Ez}{1+\nu}\frac{\partial^2 w}{\partial x \partial y}
\end{aligned} \tag{68}$$

It is seen from Eq. (68) that Kirchhoff's assumptions have led to a completely defined law of variation of the stresses through the thickness of the plate. Therefore, as in the theory of beams, it is convenient to introduce, instead of the stress components at a point problem, the total statically equivalent forces and moments applied to the middle surface, which are known as the stress resultants and stress couples. The stress resultants and stress couples are referred to as the shear forces, Q_x and Q_y, as well as the bending and twisting moments M_x, M_y and M_{xy}, respectively. Thus, Kirchhoff's assumptions have reduced the three-dimensional plate straining problem to the two-dimensional problem of straining the middle surface of the plate. Referring to Figure A.9, we can express the bending and twisting moments, as well as the shear forces, in terms of the stress components, i.e.

$$\begin{Bmatrix} M_x \\ M_y \\ M_{xy} \end{Bmatrix} = \int_{-h/2}^{h/2} \begin{Bmatrix} \sigma_x \\ \sigma_y \\ \tau_{xy} \end{Bmatrix} z\,dz \tag{69}$$

$$\begin{Bmatrix} Q_x \\ Q_y \end{Bmatrix} = \int_{-h/2}^{h/2} \begin{Bmatrix} \tau_{xz} \\ \tau_{yz} \end{Bmatrix} dz \tag{70}$$

Because of the reciprocity law of shear stresses ($\tau_{xy} = \tau_{yx}$), the twisting moments on perpendicular faces on an infinitesimal plate element are identical, i.e., $M_{xy} = M_{yx}$. The sign convention for the shear forces and the twisting moments is the same as that for the shear stresses. A positive bending moment is one which results in positive (tensile) stresses in the bottom half of the plate. Accordingly, all the moments and the shear forces acting on the element in Figure A.10 are positive. Note that the relations (69) and (70) determine the intensities of moments and shear forces, i.e., moments and forces per unit length of the plate midplane. Therefore, they have dimensional units as [*force · length/length*] or simply [*force*] for moments and [*force/length*] for shear forces, respectively. It is important to mention that while the theory of thin plates omits the effect of the strain components $\gamma_{xz} = \tau_{xz}/G$ and $\gamma_{yz} = \tau_{yz}/G$ on bending, the vertical shear forces Q_x and Q_y are not negligible. In fact, they are necessary for equilibrium of the plate element. Substituting Eq. (68) into Eq. (69) and integrating over the plate thickness, we derive the following formulas for the stress resultants and couples in terms of the curvatures and the deflection

$$\begin{aligned} M_x &= D(\chi_x + \nu\chi_y) = -D\left(\frac{\partial^2 w}{\partial x^2} + \nu\frac{\partial^2 w}{\partial y^2}\right) \\ M_y &= D(\chi_y + \nu\chi_x) = -D\left(\frac{\partial^2 w}{\partial y^2} + \nu\frac{\partial^2 w}{\partial x^2}\right) \qquad (71) \\ M_{xy} &= M_{yx} = D(1-\nu)\chi_{xy} = -D(1-\nu)\frac{\partial^2 w}{\partial x \partial y} \end{aligned}$$

where

$$D = \frac{Eh^3}{12(1-\nu^2)} \qquad (72)$$

is the *flexural rigidity* of the plate. It plays the same role as the flexural rigidity *EI* in beam bending. Note that $D > EI$; hence, a plate is always stiffer than a beam of the same span and thickness. Solving Eq. (71) for the second derivatives of the deflection and substituting the above into Eq. (68), we get the following expressions for stresses

$$\sigma_x = \pm\frac{12M_x}{h^3}z, \qquad \sigma_y = \pm\frac{12M_y}{h^3}z, \qquad \tau_{xy} = \pm\frac{12M_{xy}}{h^3}z \qquad (73)$$

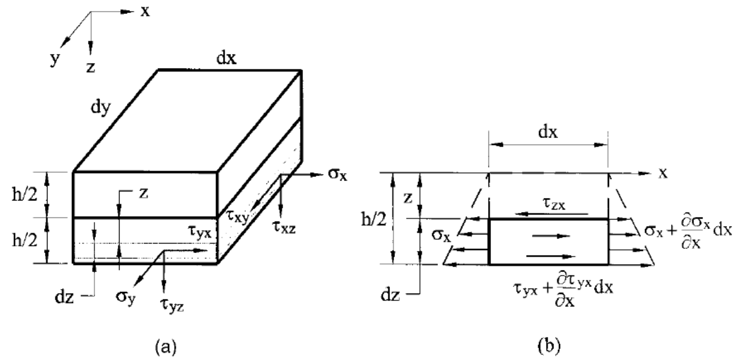

Figure A.9 Stress components of the infinitesimal element.

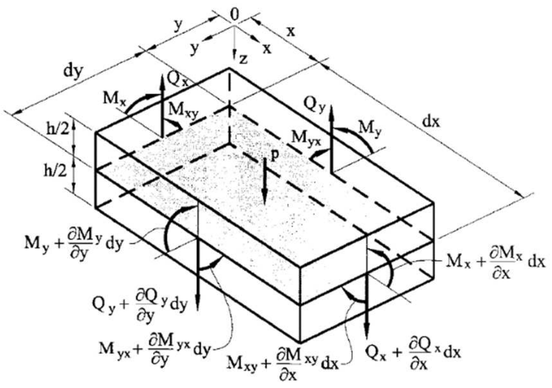

Figure A.10 Moments and the shear forces acting on the element.

Determination of the remaining three stress components τ_{xz}, τ_{yz} and σ_z through the use of Hooke's law is not possible due to the fourth and fifth assumptions, since these stresses are not related to strains. The differential equations of equilibrium for a plate element under a general state of stress (Eq. (49)) (assuming that the body forces are zero) serve well for this purpose, however. If the faces of the plate are free of any tangent external loads, then τ_{xz} and τ_{yz} are zero for $z = \pm h/2$. From the first two equations of Eq. (49) and Eq. (67), the shear stresses τ_{xz} and τ_{yz} are

$$\tau_{xz} = -\int_{-h/2}^{h/2}\left(\frac{\partial \sigma_x}{\partial x} + \frac{\partial \tau_{xy}}{\partial y}\right)dz = \frac{E\left(z^2 - h^2/4\right)}{2\left(1-\nu^2\right)}\frac{\partial}{\partial x}\nabla^2 w \qquad (74)$$

$$\tau_{yz} = -\int_{-h/2}^{h/2}\left(\frac{\partial \sigma_y}{\partial y} + \frac{\partial \tau_{xy}}{\partial x}\right)dz = \frac{E\left(z^2 - h^2/4\right)}{2\left(1-\nu^2\right)}\frac{\partial}{\partial y}\nabla^2 w \qquad (75)$$

where $\nabla^2(\,)$ is the *Laplace operator*, given by

$$\nabla^2 w = \frac{\partial^2 w}{\partial x^2} + \frac{\partial^2 w}{\partial y^2} \qquad (76)$$

It is observed from Eq. (73) and Eq. (74) and (75) that the stress components σ_x, σ_y and τ_{xy} (in-plane stresses) vary linearly over the plate thickness, whereas the shear stresses τ_{xz} and τ_{yz} vary according to a parabolic law, as shown in Figure A.11. The component σ_z is determined by using the third of Eq. (49), upon substitution of τ_{xz} and τ_{yz} from Eq. (74) and (75) and integration. As a result, we obtain

$$\sigma_z = -\frac{E}{2\left(1-\nu^2\right)}\left(\frac{h^3}{12} - \frac{h^2 z}{4} + \frac{z^3}{3}\right)\nabla^2\nabla^2 w \qquad (77)$$

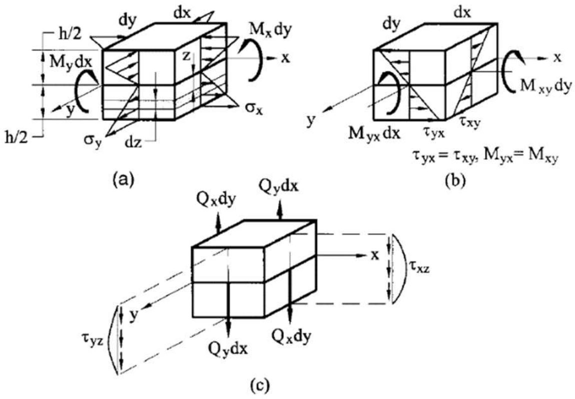

Figure A.11 Stresses over the plate thickness.

The components of stress (and, thus, the stress resultants and stress couples) generally vary from point to point in a loaded plate. These variations are governed by the static conditions of equilibrium. Consider equilibrium of an element dx x dy of the plate subject to a vertical distributed load of intensity $p(x,y)$ applied to an upper surface of the plate, as shown in Figure A.11. Since the stress resultants and stress couples are assumed to be applied to the middle plane of this element, a distributed load $p(x,y)$ is transferred to the midplane. Note that as the element is very small, the force and moment components may be considered to be distributed uniformly over the midplane of the plate element. In passing from the section x to the section x + dx an intensity of stress resultants changes by a value of partial differential, for examples, by $\partial M_x = \partial M_x / \partial x \, dx$. The same is true for the sections y and y + dy. For the system of forces and moments shown in Figure A.11, the following three independent conditions of equilibrium may be set up:

1. The force summation in the z axis gives

$$\frac{\partial Q_x}{\partial x} dxdy + \frac{\partial Q_y}{\partial y} dxdy + pdxdy = 0 \tag{78}$$

from which

$$\frac{\partial Q_x}{\partial x} + \frac{\partial Q_y}{\partial y} + p = 0 \tag{79}$$

2. The moment summation about the x axis leads to

$$\frac{\partial M_{xy}}{\partial x} dxdy + \frac{\partial M_y}{\partial y} dxdy - Q_y dxdy = 0 \tag{80}$$

$$\frac{\partial M_{xy}}{\partial x}+\frac{\partial M_{y}}{\partial y}-Q_{y}=0 \tag{81}$$

Note that products of infinitesimal terms, such as the moment of the load *p* and the moment due to the change in Q_y have been omitted in Eq. (80) as terms with higher order of smallness.

3. The moment summation about the *y* axis results in

$$\frac{\partial M_{xy}}{\partial y}+\frac{\partial M_{x}}{\partial x}-Q_{x}=0 \tag{82}$$

It follows from the expressions (81) and (82) that the shear forces Q_x and Q_y can be expressed in terms of the moments, as follows

$$Q_{x}=\frac{\partial M_{x}}{\partial x}+\frac{\partial M_{xy}}{\partial y} \tag{83}$$

$$Q_{y}=\frac{\partial M_{xy}}{\partial x}+\frac{\partial M_{y}}{\partial y} \tag{84}$$

Here it has been taken into account that $M_{xy} = M_{yx}$. Substituting Eq. (83) and (84) into Eq.(79), one finds the following

$$\frac{\partial^{2} M_{x}}{\partial x^{2}}+2\frac{\partial^{2} M_{xy}}{\partial x \partial y}+\frac{\partial^{2} M_{y}}{\partial y^{2}}=-p(x, y) \tag{85}$$

Finally, introduction of the expression for M_x, M_y and M_{xy} from Eq. (71) into Eq. (85) yields

$$\frac{\partial^{4} w}{\partial x^{4}}+2\frac{\partial^{4} w}{\partial x^{2} \partial y^{2}}+\frac{\partial^{4} w}{\partial y^{4}}=\frac{p}{D} \tag{86}$$

This is the *governing differential equation for the deflections* for thin plate bending analysis based on Kirchhoff’s assumptions. This equation was obtained by Lagrange. Mathematically, the differential equation (86) can be classified as a linear partial differential equation of the fourth order having constant coefficients. Eq. (86) may be rewritten as follows

$$\nabla^{2}\left(\nabla^{2} w\right)=\nabla^{4} w=\frac{p}{D} \tag{87}$$

Once a deflection function $w(x, y)$ has been determined from Eq. (86), the stress resultants and the stresses can be evaluated by using Eq. (71) and (73). In order to determine the deflection function, it is required to integrate Eq. (86) with the constants of integration dependent upon the appropriate boundary conditions. Expressions for the vertical forces Q_x and Q_y may now be written in terms of the deflection w from Eq. (83) and (84) together with Eq. (71) as follows

$$Q_x = -D\frac{\partial}{\partial x}\left(\frac{\partial^2 w}{\partial x^2} + \frac{\partial^2 w}{\partial y^2}\right) = -D\frac{\partial}{\partial x}\left(\nabla^2 w\right) \tag{88}$$

$$Q_y = -D\frac{\partial}{\partial y}\left(\frac{\partial^2 w}{\partial x^2} + \frac{\partial^2 w}{\partial y^2}\right) = -D\frac{\partial}{\partial y}\left(\nabla^2 w\right) \tag{89}$$

Using Eq. (88) and (89) and Eq. (87) we can rewrite the expressions for the stress components τ_{xz}, τ_{yz} and σ_z (Eq. (74) and (75) and Eq. (77)) as follows

$$\begin{aligned} \tau_{xz} &= \frac{3Q_x}{2h}\left[1-\left(\frac{2z}{h}\right)^2\right] \\ \tau_{yz} &= \frac{3Q_y}{2h}\left[1-\left(\frac{2z}{h}\right)^2\right] \\ \sigma_z &= -\frac{3p}{4}\left[\frac{2}{3}-\frac{2z}{h}+\frac{1}{3}\left(\frac{2z}{h}\right)^3\right] \end{aligned} \tag{90}$$

Summarizing the arguments set forth in this section, we come to the conclusion that the deformation of a plate under the action of the transverse load $p(x, y)$ applied to its upper plane is determined by the differential equation (86). This deformation results from:

1. bending produced by bending moments M_x and M_y as well as by the shear forces Q_x and Q_y;
2. torsion produced by the twisting moments $M_{xy} = M_{yz}$.

Both of these phenomena are generally inseparable in a plate.

A.2. Thin orthotropic plates

A.2.1. General

Up to this point, all our previous discussions of plates have assumed the plate material to be isotropic according to assumption (1). We recall that the assumption of isotropy implies that material properties at a point are the same in all directions. This means that if an isotropic material is subjected to an axial stress in a principal direction, the major deformation occurs in the direction of the applied load. Lateral deformations of smaller magnitude occur in the other principal directions. Also, shear stress causes only shear deformation. So, normal strains and stresses are not coupled to shear strains and stresses. The deformations are dependent on the two independent elastic constants, for instance E and ν. However, certain materials display direction-dependent properties; consequently, these materials are referred to as anisotropic. In anisotropic materials stressed in one of the principal directions, the lateral deformations in the other principal directions could be smaller or larger than the deformation in the direction of the applied stress depending on the material properties. For a general anisotropic material, the matrix of material constants, because of symmetry, contains twenty-one independent material constants. This means that all the strains are coupled to all the stresses. Some materials such as wood, fiber-reinforced plastic, etc., fall into this category. These materials possess *natural anisotropy*. Besides plates made of anisotropic materials, a number of manufactured plates made of isotropic materials also may fall into the category of anisotropic plates: examples include corrugated and stiffened plates, etc. Such a type of anisotropy is referred to as *structural anisotropy* and that of an anisotropic plate can approximately replace their structural behaviour. Such an approximation is possible if, for examples, stiffeners are arranged sufficiently close to each other so that the given stiffened plate can be replaced by an orthotropic homogeneous plate with “distributed” stiffened rigidities along the plate. Experimental data indicate a good agreement with this idealization provided that the flexural rigidities are uniformly distributed in the x and y directions. If an anisotropic material has three mutually perpendicular planes of symmetry with respect to its elastic properties, it is called *orthotropic* (i.e. orthogonally anisotropic).

A.2.2. Basic relationships

Let us consider bending of plates of constant thickness and made of orthotropic material. Assume that the principal directions of orthotropy coincide with the x and y coordinate axes which, in turn, lie in the middle plane of the plate. The stress-strain relations (Eq. (67)) used for isotropic plates are not valid for orthotropic plates. Thus, we must obtain a new set of stress-strain relations that reflects the orthotropic properties of a material of the plate. Such a set of relations is shown below (Lekhnitskii, 1968)

$$\varepsilon_x = \frac{\sigma_x}{E_x} - \nu_y \frac{\sigma_y}{E_y}, \qquad \varepsilon_y = \frac{\sigma_y}{E_y} - \nu_x \frac{\sigma_x}{E_x}, \qquad \gamma_{xy} = \frac{\tau_{xy}}{G} \tag{91}$$

where E_x, E_y, ν_x, ν_y and G are assumed to be elastic constants of an orthotropic material, i.e., E_x, E_y and ν_x, ν_y are the moduli of elasticity and Poisson’s ratios in the x and y directions, respectively. They are independent of one another. G is the shear modulus, which is the same for both isotropic and orthotropic materials. It can be expressed in terms of E_x and E_y as follows

$$G \approx \frac{\sqrt{E_x E_y}}{2\left(1+\sqrt{\nu_x \nu_y}\right)} \tag{92}$$

The following relationship exists between independent elastic constants introduced above

$$\frac{\nu_x}{E_x} = \frac{\nu_y}{E_y} \tag{93}$$

This equality directly results from Betti's reciprocal theorem. Solving Eq. (91) for the stress components and taking into account Eq. (93), we obtain

$$\sigma_x = \frac{E_x}{1-\nu_x\nu_y}\left(\varepsilon_x + \nu_y \varepsilon_y\right), \qquad \sigma_y = \frac{E_y}{1-\nu_x\nu_y}\left(\varepsilon_y + \nu_x \varepsilon_x\right), \qquad \tau_{xy} = G\gamma_{xy} \tag{94}$$

Substituting the relations of the Eq. (63) into Eq. (94) gives the following

$$\begin{aligned}
\sigma_x &= -\frac{E_x}{1-\nu_x\nu_y}\left(\frac{\partial^2 w}{\partial x^2} + \nu_y \frac{\partial^2 w}{\partial y^2}\right) z \\
\sigma_y &= -\frac{E_y}{1-\nu_x\nu_y}\left(\frac{\partial^2 w}{\partial y^2} + \nu_x \frac{\partial^2 w}{\partial x^2}\right) z \\
\tau_{xy} &= -2Gz \frac{\partial^2 w}{\partial x \partial y}
\end{aligned} \tag{95}$$

Substituting the above into Eq. (69) and integrating over the plate thickness, yields the following bending and twisting moments deflection relations for orthotropic plates

$$\begin{aligned}
M_x &= -\left[D_x \frac{\partial^2 w}{\partial x^2} + D_{xy} \frac{\partial^2 w}{\partial y^2}\right] \\
M_y &= -\left[D_y \frac{\partial^2 w}{\partial y^2} + D_{yx} \frac{\partial^2 w}{\partial x^2}\right] \\
M_{xy} &= -2D_s \frac{\partial^2 w}{\partial x \partial y}
\end{aligned} \tag{96}$$

where D_x, D_y, D_{xy}, D_{yx} and D_s are the flexural and torsional rigidities of an orthotropic plate, respectively, and are given as

$$D_x = \frac{E_x}{1-\nu_x\nu_y}\frac{h^3}{12}, \qquad D_y = \frac{E_y}{1-\nu_x\nu_y}\frac{h^3}{12}, \qquad D_{xy} = \frac{E_x\nu_y}{1-\nu_x\nu_y}\frac{h^3}{12}$$

$$D_{yx} = \frac{E_y\nu_x}{1-\nu_x\nu_y}\frac{h^3}{12}, \qquad D_s = \frac{Gh^3}{12} \tag{97}$$

In view of the expressions (93), one can conclude that $D_{xy} = D_{yx}$. The shear force expressions in Eq. (83) and (84) become

$$Q_x = -\frac{\partial}{\partial x}\left(D_x \frac{\partial^2 w}{\partial x^2} + H \frac{\partial^2 w}{\partial y^2} \right) \tag{98}$$

$$Q_y = -\frac{\partial}{\partial y}\left(H \frac{\partial^2 w}{\partial x^2} + D_y \frac{\partial^2 w}{\partial y^2} \right) \tag{99}$$

where

$$H = D_{xy} + 2D_s \tag{100}$$

The governing differential equation (86) for orthotropic plates becomes

$$D_x \frac{\partial^4 w}{\partial x^4} + 2H \frac{\partial^4 w}{\partial x^2 \partial y^2} + D_y \frac{\partial^4 w}{\partial y^4} = p(x, y) \tag{101}$$

The latter equation (sometimes called *Huber equation*) is valid for both naturally and structurally orthotropic plates provided structural elements causing orthotropy are arranged sufficiently close together, so as to ignore a jump change of elastic properties in a plate.

A.3. The effect of transverse shear deformation on the bending of elastic plates

A.3.1. Introduction

Kirchhoff's hypotheses permitted the creation of the classical (Kirchhoff's) bending theory of thin plates which for more than a century has been the basis for the calculation and design of structures in various areas of engineering and has yielded important theoretical and numerical results. However, just as for any other approximation theory, Kirchhoff's theory has some obvious drawbacks and deficiencies, two of which are:

1. a well-known disagreement exists between the order of Eq. (51) and the number of the boundary conditioners on the plate free edge. As a result, the boundary conditions of the classical theory take into account only two characteristics on the free edge of the plate rather than three characteristics corresponding to the reality.
2. Certain formal contradictions take place between the Kirchhoff plate theory and the three-dimensional equation of elasticity. The most important of the above contradictions is associated with Hooke's law for the transverse shear stresses τ_{xz} and τ_{yz}. In fact, the deformations γ_{xz} and γ_{yz} are absent according to the hypotheses of the classical theory. However, the stresses τ_{xz} and τ_{yz} cannot be equal to zero because the shear forces Q_x and Q_y, which are resultants of the abovementioned stresses, are necessary for an equilibrium of the plate differential element.

Notice that as a result of an inaccuracy of Kirchhoff's theory, we cannot guarantee that the stress distribution predicted by this theory will agree well with the actual stresses in the immediate vicinity of the plate edge. The latter statement acquires a practical importance of a refinement of the classical plate theory for plate fields neighbouring to a boundary or to openings whose diameter (or another typical dimension) is not too large compared with the plate thickness. Numerous researches have attempted to refine Kirchhoff's theory. E. Reissner made the most important advance in this direction (Reissner, 1944). Reissner's theory takes into account the influence of the transverse shear deformation on the deflection of the plate and leads to a sixth-order system of governing differential equations and, accordingly, to three boundary conditions on the plate edge. Here it is unnecessary to introduce the effective transverse shear force. Reissner's theory is free from the drawbacks of Kirchhoff's theory discussed above.

The correct interpretation of Reissner's theory is complicated substantially by the fact that this theory involves the variational procedure to derive the governing equations, which was essentially based on the use of Kirchhoff's theory to approximate the stress distribution over the thickness of the plate. Therefore, another approach is presented below for obtaining the governing differential equations of the refined plate bending theory, which takes into account the transverse shear deformations. According to this approach, the above equations are derived from the equations of the theory of elasticity and certain physical hypotheses. This approach was developed by Vasil'ev (Vasil'ev, 1998).

A.3.2. The governing equations

Let us introduce again three familiar hypotheses:

1. the straight line normal to the middle plane of the plate does not change its length and remains rectilinear when the plate is subjected to bending;
2. the transverse normal stress σ_z is small compared with the stresses σ_x and σ_y;
3. the middle plane remains unstrained subsequent to bending.

The only difference between these hypotheses and Kirchhoff's hypotheses is that the former hypotheses do not require the straight line of the plate to be orthogonal to the bent mid-surface of the plate. In this case, the straight line normal to the middle plane, called also the normal element, acquires three independent degrees of freedom corresponding to the deflection $w(x, y)$ and the angles of rotations ϑ_x and ϑ_y which are not related to the deflection w as it has taken place in Kirchhoff's theory. It has been shown that the displacement components over the plate thickness, according to the abovementioned hypotheses, obey the following law

$$u = -z\vartheta_x(x, y), \qquad v = -z\vartheta_y(x, y), \qquad w = w(x, y) \tag{102}$$

By repeating the derivation of relations (71) we obtain

$$M_x = -D\left(\frac{\partial \vartheta_x}{\partial x} + \nu\frac{\partial \vartheta_y}{\partial y}\right)$$

$$M_y = -D\left(\frac{\partial \vartheta_y}{\partial y} + \nu\frac{\partial \vartheta_x}{\partial x}\right) \tag{103}$$

$$M_{xy} = -\frac{1}{2}D(1-\nu)\left(\frac{\partial \vartheta_x}{\partial y} + \frac{\partial \vartheta_y}{\partial x}\right)$$

Note that if the angles of rotation are related to the deflections by relations of the type of (62), the bending and twisting moment equations (103) will coincide with the relations (71) derived for the classical (Kirchhoff's) theory. The stresses σ_x, σ_y and τ_{xy} are related to the stress resultants M_x, M_y and M_{xy} by relations (69) and the transverse shear forces Q_x and Q_y are resultants of the transverse shear stresses τ_{xz} and τ_{yz}. As mentioned previously, the transverse shear forces cannot be obtained directly by integrating the Eq. (70) in Kirchhoff's theory. However, the refined theory makes it possible to obtain Q_x and Q_y in terms of the deflection w and the angles of rotation ϑ_x and ϑ_y by integrating Eq. (70). Substituting for τ_{xz} and τ_{yz} from Eq. (47) into Eq.(70) and using the second and third relations (43) and (102), we obtained the following

$$Q_x = G\int_{-h/2}^{h/2}\left(\frac{\partial u}{\partial z} + \frac{\partial w}{\partial x}\right)dz = Gh\left(-\vartheta_x + \frac{\partial w}{\partial x}\right) \tag{104}$$

Thus, within the framework of the theory, one can obtain the transverse shear forces as the stress resultants of the shear stress τ_{xz} and τ_{yz}. We have the following

$$Q_x = C\eta_x, \qquad Q_y = C\eta_y \tag{105}$$

where

$$C = Gh, \qquad \eta_x = -\vartheta_x + \frac{\partial w}{\partial x}, \qquad \eta_y = -\vartheta_y + \frac{\partial w}{\partial y} \tag{106}$$

and C describes the shear stiffness of the plate in the planes xz and yz. Considering the equilibrium of the plate element, we obtain Eq. (79) and Eq. (83) and (84). Substituting for the stress resultants from the relations (103) and (105) into Eq. (79) and Eq. (83) and (84), we arrive at the system of equations for ϑ_x, ϑ_y and w. It is possible to simplify this system. To this end, we use Eq. (85). By substituting the moments according Eq. (103) into the above equation, we obtain

$$D\nabla^2\left(\frac{\partial \vartheta_x}{\partial x} + \frac{\partial \vartheta_y}{\partial y}\right) - p = 0 \tag{107}$$

Let us introduce the so-called *potential function* $\Phi(x, y)$ of the displacement field in a plane z = const. which satisfies the following relations

$$\vartheta_x = \frac{\partial \phi}{\partial x}, \qquad \vartheta_y = \frac{\partial \phi}{\partial y} \tag{108}$$

Using this function, we can reduce Eq. (107) to the form

$$D\nabla^2\nabla^2\phi = p \tag{109}$$

Using Eq. (83) and (84) and substituting there the expressions (103) and (105) for moments and forces together with relations (109) we obtain

$$\frac{\partial F_\phi}{\partial x} = 0, \qquad \frac{\partial F_\phi}{\partial y} = 0, \qquad F_\phi = \frac{D}{C}\nabla^2\phi - \phi + w \tag{110}$$

From the first two equations of (110) it follows that F_Φ = const. The value of this constant is unessential for the potential function and, hence, can be assumed to be equal to zero without loss of generality. Then, $F_\Phi = 0$ and we obtain the following from Eq. (110)

$$w = \phi - \frac{D}{C}\nabla^2\phi \tag{111}$$

where the function Φ is given by Eq. (108) . This potential is sometimes referred to as the penetrating potential, because it describes solutions that penetrate into the plate domain. However, this potential cannot describe completely the bending behavior of the plate. It does not take into account the rotation of the plate element in its own plane, which can be described by the so-called *stream function* Ψ. This function may be introduced as follows

$$\vartheta_x = -\frac{\partial \psi}{\partial y}, \qquad \vartheta_y = \frac{\partial \psi}{\partial x}, \qquad w = 0 \tag{112}$$

It can be easily verified that the relations (112) represent the solution of the homogeneous equation (107) (i.e., for $p = 0$). Substituting the expressions (103) for the moments and expressions (105) for the shear forces into Eq. (83) and (84) and using Eq. (112), we obtain

$$\frac{\partial F_\psi}{\partial x} = 0, \qquad \frac{\partial F_\psi}{\partial y} = 0, \qquad F_\psi = \Delta\psi - k^2\psi \tag{113}$$

where

$$k^2 = \frac{2C}{D(1-\nu)} \tag{114}$$

By repeating the reasoning that led to Eq. (111), we arrive at the *Helmholtz equation*

$$\nabla^2\psi - k^2\psi = 0 \tag{115}$$

Since the plate bending problem is assumed to be linear, we can use the method of superposition and represent the angles of rotation of the normal element of the plate as follows

$$\vartheta_x = \frac{\partial \phi}{\partial x} - \frac{\partial \psi}{\partial y}, \qquad \vartheta_y = \frac{\partial \phi}{\partial y} - \frac{\partial \psi}{\partial x} \tag{116}$$

where the functions Φ and Ψ are defined by Eq.(108) and (112), respectively. Equations (109) and (115) represent the *sixth-order system of governing differential equations of the plate bending theory by taking into account the transverse shear deformation*. This theory is sometimes referred to as the *shear or refined plate theory*.

The deflection w is given by Eq. (111). Taking into account the relations (103) and (116), we can express the bending and twisting moments, as well as shear forces, in terms of the following functions Φ and Ψ

$$M_x = -D\left[\frac{\partial^2\phi}{\partial x^2} + \nu\frac{\partial^2\phi}{\partial y^2} - (1-\nu)\frac{\partial^2\psi}{\partial x \partial y}\right] \tag{117}$$

$$M_y = -D\left[\frac{\partial^2\phi}{\partial y^2} + \nu\frac{\partial^2\phi}{\partial x^2} - (1-\nu)\frac{\partial^2\psi}{\partial x\partial y}\right]$$

$$M_{xy} = -D(1-\nu)\left[\frac{\partial^2\phi}{\partial x\partial y} + \frac{1}{2}\left(\frac{\partial^2\psi}{\partial x^2} - \frac{\partial^2\psi}{\partial y^2}\right)\right]$$

$$Q_x = -D\frac{\partial}{\partial x}\nabla^2\phi + C\frac{\partial\psi}{\partial y}, \qquad Q_y = -D\frac{\partial}{\partial y}\nabla^2\phi + C\frac{\partial\psi}{\partial x} \tag{118}$$

As $C \to \infty$ (i.e., the transverse shear deformation is ignored) it follows from the Eq. (111) and (115) that $\Psi = 0$ and $w = \Phi$ and the resulting system of Eq. (109) and (115) degenerates into the governing differential equation (86) of the Kirchhoff's theory. From the above it follows that the effect of the transverse shear strains is twofold. Consider the second term of the right-hand side of Eq. (111). It determines the effect of the shear strain on the deflection. The asymptotic analysis, conducted by Vasil'ev, showed that the coefficient $\nabla^2\Phi$ in Eq. (111) contains the factor of h^2/a^2, where a is the characteristic length of the plate. Since h^2/a^2 is a very small value for thin plates, we can set $w = \Phi$ with a high degree of accuracy. The second effect of the shear strains is associated with the existence of the Helmholtz equation (Eq. (115)). The key difference between Kirchhoff's theory and the refined theory presented is directly related to that equation. It was established (Vasil'ev, 1998 and Zihlin, 1992) that the Helmholtz equation determines the state of stress of the plate near the plate edge or other perturbation line along which the continuity of the plate geometry is violated, or in the vicinity of the applied load, etc. It is known that solutions of this equation vary rapidly only when remote from the edge. Therefore, the potential Ψ is a function of the boundary layer type, i.e., it describes solutions that decay with increasing distance from the boundary. It was established that Ψ decays at a distance equal approximately to two thicknesses from the boundary. At interior points of the plate domain that are farther than $2h$ from the boundary, therefore, the solution is described practically exactly by the penetrating potential Φ. This, of course, does not mean that the boundary layer potential Ψ can be ignored, because it may influence significantly the penetrating potential via the boundary conditions.

Let us determine the stress components corresponding to the displacements (102). Repeating the derivation of the stress-moments relations (73), it can be shown that the stresses σ_x, σ_y and τ_{xy} are defined by the same relations (73) as in the case for Kirchhoff's plate bending theory. Now we can proceed to determining the shear stresses τ_{xz} and τ_{yz}. If we substitute for the transverse shear strains γ_{xz} and γ_{yz} from Eq. (43), together with the relations (102), into the constitutive equations (47) for the transverse shear stresses, we obtain

$$\tau_{xz} = G\left(-\vartheta_x + \frac{\partial w}{\partial x}\right), \qquad \tau_{yz} = G\left(-\vartheta_y + \frac{\partial w}{\partial y}\right) \tag{119}$$

These stresses do not satisfy the following static boundary conditions

$$\tau_{xz} = 0\big|_{z=\pm h/2}, \qquad \tau_{yz} = 0\big|_{z=\pm h/2} \tag{120}$$

because the theory under consideration is based on the displacement approximation in the form of Eq. (102). Note that these relations also do not coincide with the relations (74) and (75), which follow from the equilibrium equations. Kirchhoff's theory is free from this contradictions because it does not involve the constitutive relations (47).

Other theories ore known in the literature among which the most accredited can be expressed in the following form

$$D\nabla^2\nabla^2 w = \left[1 - \alpha(\nu)\frac{s^2\nabla}{1-\nu}\right]p \tag{121}$$

where the values of the $\alpha(\nu)$ coefficients are summarized in the Table A.1.

Table A.1 Coefficients $\alpha(\nu)$.

Theory	Coefficient $\alpha(\nu)$
Reissner	$2/\pi^2$
Mindlin	$(2-\nu)/10$
Hencky	$1/6$
Kromm e Panc	$1/5$
Wang e Shi	$(8-3\nu)/40$